UNIVERSITY OF TWENTE.

Faculty of Thermal and Fluid Engineering

Lagrangian Trajectory Method with Bubble Dynamics for Cavitation Inception Predictions

S. J. Beelen

M.Sc. Thesis
March 2018

Supervisors:
ir. M. X. van Rijsbergen
Prof. dr. ir. H. W. M. Hoeijmakers

Mechanical Engineering Group
Faculty of Thermal and
Fluid Engineering
University of Twente
P.O. Box 217
7500 AE Enschede
The Netherlands

M.Sc. Thesis

Lagrangian Trajectory Method with Bubble Dynamics for Cavitation Inception Predictions

February 8, 2018

Supervisors:

ir. M. X. van Rijsbergen

Prof. dr. ir. H.W.M. Hoeijmakers

Author: S.J. Beelen, s1385232

Marin
M.Sc. Thesis Mechanical Engineering

Number of pages of content: 75

MARIN/UT/ME-February 8, 2018

Summary

Cavitation can occur in the form of sheet cavitation, which is in many cases induced by free-stream nuclei. To track the free-stream nuclei a Lagrangian approach is coupled with bubble dynamics.

By means of an elementary model, with a symmetric profile at zero incidence, the so called screening effect is observed. Screening makes large gas nuclei pass over the low pressure region, by which cavitation inception is prevented. The screening effect depends on the free stream velocity and on the size of the body, but can not be described by the flow Reynolds number. The equivalent Stokes number can be related to the scale effects on screening.

To evaluate the scale effects on cavitation in more detail the elementary model is replaced by a more involved model. This model uses conformal mapping to construct an, in general, non-symmetric profile at incidence. A bubble dynamics equation will be used for the stability of the nucleus, and the equation of motion is reevaluated.
The Kelvin impulse is introduced into the equation of motion. Furthermore, contamination of surfactants in the liquid yields the need for the history force in the equation of motion. When the nucleus is in contact with the surface of the body, an impact model, based on the local flow velocity and the nucleus growth, describes the trajectory of the nucleus.
The Kármán-Trefftz conformal transformation is used to approximate the potential flow field around a propeller blade section. The propeller blade section is non-symmetric and at incidence. Screening effects do not influence the available nuclei spectrum under these non-symmetric conditions. The available nuclei spectrum for cavitation is mainly determined by the stability of the nucleus. The cavitation event rate is derived from the bandwidth in which nuclei should start to cause cavitation. The cavitation event rate shows that to interpreted experimental results focusing on the available nuclei spectrum is insufficient.

Finally, first order interpolation in a viscous flow field is examined. The viscous flow field is around a NACA0015 profile with a flow Reynolds number of $\mathrm{Re}_f = 3.6 \cdot 10^5$ and a chord length of $c = 60\,mm$. Using viscous flow the Saffman lift force could be important, but turns out not to be important for the nucleus trajectory. The impact model is the mayor reason behind this insignificant importance. The used profile is symmetric, but has an angle of attack. This means that the conditions are non-symmetric, non-symmetric screening behavior is thus observed. When comparing a flow field without a roughness element to a flow field with a roughness element, more growth of gas nuclei is observed. However, the observed effect of the roughness element in experiments is not solely described by this increase in growth. The equation of motion is suitable with solid nuclei. Analysis with solid nucleus, more dense than the liquid, shows that solid nuclei deviate in the opposite direction as gas nuclei from the streamline.

Preface

This master thesis is written as a part of the masters program mechanical engineering over the past nine months.
During these nine months I had the opportunity to get a feeling for what doing fundamental research can provide for practical applications. I experienced dealing with the limits of modeling as both interesting and challenging. To a large extend the model has provided insight by challenging its own limits. Challenging the limits of a model, based on fundamental physics, whilst keeping practical applications as a reference frame might be the strong point of the thesis.

In this very short period of conducting research, I found at least as many questions as answers. This is inherent to doing fundamental research in my view, till this point I am indecisive if I like this. Encountering new questions is on the one hand challenging, but not all questions have answers.

I am content on and proud of the presented thesis. So enjoy reading!

Acknowledgments

Starting with an internship at MARIN which was later continued with this master thesis, I enjoyed working at MARIN. I would like to thank Martijn van Rijsbergen in particular. As the supervisor at MARIN, Martijn provided constructive conversations on a (more than) weekly basis. The discussions with Martijn helped to clear my thinking, and to either formulate the problem or the solution. The patience involved in helping me put in to words the technical results was and is admirable. Furthermore, I highly value the advice on some professional improvements. Those other employees at MARIN who provided help are appreciated for it.

As the supervisor from the University of Twente, Prof. dr. ir. Hoeijmakers provided monthly support. The support has always been very clear, useful and adequate. I am thankful for this support, and still grateful for him to give me the opportunity to do my internship out of which the master thesis followed at MARIN.

The contact with Dirk van Eijkeren helped, among others, to clarify and speed up the implementation of the History force. Lars Bruinekreeft helped by checking the report.

Simon Beelen
February 8, 2018

Contents

List of symbols

Roman symbols

a	Intersection with ξ-axis	$[m]$
a	Kernel dependent factor	$[-]$
b	Kernel dependent factor	$[-]$
c	Speed of sound of the liquid	$[ms^{-1}]$
c	Kernel dependent factor	$[-]$
c	Chord length	$[m]$
c_1	General factor	$[-]$
c_2	General factor	$[-]$
C	Nuclei concentration	$[m^{-3}]$
C_{am}	Coefficient of added mass	$[-]$
C_D	Drag coefficient	$[-]$
$C_{L,S}$	Saffman lift force coefficient	$[-]$
C_p	Pressure coefficient	$[-]$
D_n	Normal distance	$[m]$
$\dot{E}$	Cavitation event rate	$[s^{-1}]$
$\dot{E}'$	Cavitation event rate per meter	$[s^{-1}m^{-1}]$
Eo	Eötvös number	$[-]$
Eo$'$	Modified Eötvös number	$[-]$
f_D	Drag factor	$[-]$
$\mathbf{F}$	Force vector	$[kgms^{-2}]$
g	Kernel dependent factor	$[-]$
g	Gravitational acceleration	$[ms^{-2}]$
$\mathbf{g}$	Gravitational acceleration vector	$[ms^{-2}]$
h	Half ultimate body width	$[m]$
h	Spatial step size	$[m]$
h	Kernel dependent factor	$[-]$
$\mathbf{I}$	Kelvin impulse	$[kgms^{-1}]$
J	advance ratio	$[-]$
K	History kernel	$[-]$
m_p	Mass of the nucleus	$[kg]$
n	Transformation parameter	$[-]$
n_{prop}	Rotational rate propeller	$[s^{-1}]$
$\mathbf{n}$	Inward unit normal	$[-]$
$\hat{\mathbf{n}}$	Outward unit normal	$[-]$
p	Local pressure	$[kgm^{-1}s^{-2}]$
p_v	Vapor pressure	$[kgm^{-1}s^{-2}]$
p_g	Gas pressure	$[kgm^{-1}s^{-2}]$
p_0	Initial pressure	$[kgm^{-1}s^{-2}]$
q	General flow property	$[-]$
$\mathbf{Q}$	General vector	$[-]$
r	Radial polar coordinate	$[m]$
r_{prop}	Local propeller radius	$[m]$
R	Nucleus radius	$[m]$

$\hat{R}$	Dimensionless radius	$[-]$
R_{cyl}	Transformed cylinder radius	$[m]$
R_{crit}	Critical radius	$[m]$
R_{prop}	Total propeller radius	$[m]$
R_0	Initial radius	$[m]$
$\hat{R}_0$	Initial dimensionless radius	$[-]$
Re_p	Nucleus Reynolds number	$[-]$
Re_f	Flow Reynolds number	$[-]$
Stk_{eq}	Equivalent Stokes number	$[-]$
t	Time	$[s]$
$\hat{t}$	Dimensionless time	$[-]$
T_H	History time	$[s]$
u	Horizontal flow velocity	$[ms^{-1}]$
$\hat{u}$	Dimensionless horizontal flow velocity	$[-]$
u_p	Horizontal nucleus velocity	$[ms^{-1}]$
U_0	Free stream velocity	$[ms^{-1}]$
v	Vertical flow velocity	$[ms^{-1}]$
$\hat{v}$	Dimensionless vertical flow velocity	$[-]$
v_p	Vertical nucleus velocity	$[ms^{-1}]$
V_{lin}	Linear velocity propeller	$[ms^{-1}]$
$\mathbf{w}$	Flow velocity vector	$[ms^{-1}]$
$\bar{\mathbf{w}}$	Relative velocity vector	$[ms^{-1}]$
$\hat{\mathbf{w}}$	Dimensionless flow velocity vector	$[-]$
$\mathbf{w}_p$	Nucleus velocity vector	$[ms^{-1}]$
$\hat{\mathbf{w}}_p$	Dimensionless nucleus velocity vector	$[-]$
W	Complex velocity	$[ms^{-1}]$
$\tilde{W}$	Complex velocity of computational frame	$[ms^{-1}]$
We	Weber number	$[-]$
x	Dimensionless horizontal position	$[-]$
x	Horizontal position	$[m]$
x_g	Horizontal grid point position	$[m]$
x_p	Nucleus dimensionless horizontal position	$[-]$
$\mathbf{x}_g$	Grid point position	$[m]$
$\mathbf{x}_p$	Nucleus position vector	$[m]$
y	Dimensionless vertical position	$[-]$
y	Vertical position	$[m]$
y_g	Vertical grid point position	$[m]$
y_p	Nucleus dimensionless vertical position	$[-]$
z	Complex solution location	$[m]$
$\mathbf{z}$	General vector	$[-]$

Greek symbols

α	Angle of attack	$[-]$
α_{te}	Trailing edge angle	$[-]$
γ	Surface tension	$[kgs^{-2}]$
Γ	Circulation	$[m^2s^{-1}]$
ε	Roughness height	$[m]$
ζ	Complex computational location	$[m]$
η	Imaginary part of ζ	$[m]$
θ	Angular polar coordinate	$[-]$
λ	General factor	$[-]$
μ_f	Liquid dynamic viscosity	$[kgm^{-1}s^{-1}]$
ν_f	Liquid kinematic viscosity	$[m^2s^{-1}]$
ξ	Real part of ζ	$[m]$
ρ_f	Liquid density	$[kgm^{-3}]$
ρ_p	Nucleus density	$[kgm^{-3}]$
σ_v	Cavitation number	$[-]$
τ	Integration variable	$[s]$
τ_d	Diffusive timescale of the nucleus	$[s]$
ϕ	Potential	$[m^2s^{-1}]$
ω_f	2D flow vorticity	$[s^{-1}]$

1 Introduction

Cavitation is the formation of cavities in the liquid. A cavity in the liquid is a liquid free zone, the cavity can be filled with gas. Cavities arise in low pressure regions. The cavities can implode when the pressure increases. The implosions cause damage to propellers and rudders, lowers the efficiency of propellers, and produces noise. For the maritime and pump industry, the costs of cavitation are significant. The produced noise impacts sea life, the usability of pumps and the comfort on cruise ships.
Cavitation can occur in the form of sheet cavitation, which is in many cases induced by free-stream nuclei, see [1]. High-speed observations showed that both gaseous and solid nuclei which induced sheet cavitation could deviate significantly from calculated streamlines.

Understanding the underlying processes of sheet cavitation inception is crucial for cavitation models. These models should capture scale effects as experimental comparison is not possible in many cases. A model describing the nucleus trajectory and the dynamics of the nucleus could give insight on sheet cavitation inception, and the scale effects involved.

A Lagrangian approach yielding an equation of motion coupled with bubble dynamics can be used to obtain insight in the sheet cavitation inception process. The scale effects assumed to play a role will be examined. The so called screening effect pushes large bubbles over the leading edge low pressure region, preventing cavitation. The screening effect might be subject to scale effects which will be reviewed in particular. The application of this model to different flow fields will also be discussed.

The report is subdivided into three main parts.

- The first part introduces the elementary concepts of nuclei stability and screening. The resulting model is used to estimate the cavitation inception related scale effects on a symmetric headform in a potential flow field.
- In the second part, the nuclei stability and nuclei screening is revisited. Bubble dynamics is combined with a more complete equation of motion. The potential flow field is described by a Kármán-Trefftz transformation. The model is applied on a propeller blade section, yielding a non-symmetric foil at an angle of attack.
- The final part describes the applicability and needed adjustments of the model to viscous flows. The effect of a roughness element on a profile is studied, and the compatibility of the model with solid nuclei is examined.

ELEMENTARY NUCLEI STABILITY AND SCREENING

In the first part, the concept of nuclei stability and screening is introduced by means of an elementary model involving relations to describe growth and motion of nuclei.

2 Cavitation inception on a symmetric semi-infinite profile

In [2], a model is presented to estimate the influence of the trajectories of gas nuclei on cavitation inception. The bubble dynamics have been approximated by a quasi-steady bubble growth equation and the trajectory is calculated using a simple force balance method. Replicating the results presented in [2] is therefore a good exercise to get acquainted with a Lagrangian method. The layout of [2] will be adopted which leads to three main parts, namely: Static stability of spherical gas bubbles, Bubble trajectory and Application to a two-dimensional half body in an infinite fluid.

2.1 Static stability of spherical gas bubbles

The static stability of spherical gas bubbles, in the content of cavitation inception referred to as nuclei or gas nuclei, is described by Eq. 2.1.

$$\frac{p - p_v}{p_0 - p_v} = \left(\frac{R_0}{R}\right)^3 \left[1 + \frac{8}{\sigma_v \mathrm{We}} \left(1 - \frac{R^2}{R_0^2}\right)\right] \tag{2.1}$$

p is the local liquid pressure, p_v is the vapor pressure of the liquid, p_0 is the pressure at the initial location, R_0 is the initial radius of the nucleus, R is the current radius of the nucleus, σ_v is the cavitation number, given in Eq. 2.2, and We is the Weber number, given in Eq. 2.3. The derivation of Eq. 2.1 can be found in Appendix A.

$$\sigma_v = \frac{p_0 - p_v}{\frac{1}{2}\rho_f U_0^2} \tag{2.2}$$

$$\mathrm{We} = \frac{2\rho_f U_0^2 R_0}{\gamma} \tag{2.3}$$

ρ_f is the density of the liquid, U_0 is the free stream velocity and γ is the surface tension.
Eq. 2.1 is the pressure balance on the bubble wall in semi-dimensionless form, and can be solved for the radius, R. The solution of Eq. 2.1 is used to predict the nucleus growth, and is given in Appendix A.
The Blake critical radius, R_{crit}, can be found by means of Eq. 2.1, see Eq. 2.4. The derivation of the critical radius can be found in Appendix A.

$$R_{crit} = R_0 \sqrt{3\left(\frac{\mathrm{We}\sigma_v}{8} + 1\right)} \tag{2.4}$$

Once the critical radius is reached the nucleus will grow exponentially, which is used as the definition of cavitation inception in [2].
Along with the critical radius, a critical pressure can be derived, this pressure is called the

Blake threshold pressure. The critical pressure leads to Eq. 2.5, which is derived in Appendix A.

$$C_p^* + \sigma_v = -\frac{2\sigma_v \left(\frac{8}{\sigma_v \mathrm{We}}\right)^{3/2}}{3\sqrt{3}\left(1 + \frac{8}{\sigma_v \mathrm{We}}\right)^{1/2}} \tag{2.5}$$

C_p^* is the critical pressure coefficient. The definition of the pressure coefficient is given in Eq. 2.6.

$$C_p = \frac{p - p_0}{\frac{1}{2}\rho_f U_0^2} \tag{2.6}$$

The bubble growth depends on the Weber number, the cavitation number and the pressure coefficient. A lower cavitation number means that the nucleus will grow more easily. A lower pressure coefficient and a higher Weber number also mean more growth.

2.2 Bubble trajectory

The equation of motion is constructed using a force balance on the bubble. The forces which will be included in the equation of motion are the added mass force, the drag force and the pressure force. The force balance is given in Eq. 2.7.

$$\underbrace{\frac{1}{2}\frac{4}{3}\pi R^3 \rho_f \frac{d\mathbf{w}_p}{dt}}_{\text{Added mass force}} = \underbrace{\frac{1}{2}\rho_f (\mathbf{w} - \mathbf{w}_p)|\mathbf{w} - \mathbf{w}_p| C_D \pi R^2}_{\text{Drag force}} - \underbrace{\frac{3}{2}\frac{4}{3}\pi R^3 \nabla p}_{\text{Pressure force}} \tag{2.7}$$

$\mathbf{w}_p$ is the velocity of the nucleus with components: $\mathbf{w}_p = \begin{bmatrix} u_p & v_p \end{bmatrix}^T$. $\mathbf{w} = \begin{bmatrix} u & v \end{bmatrix}^T$ is the flow velocity. ρ_f is the density of the fluid. C_D is the drag coefficient defined in Eq. 2.8. ∇p is the pressure gradient.

$$\frac{C_D \mathrm{Re}_p}{24} = 1 + 0.197 \mathrm{Re}_p^{0.63} + 2.6 \cdot 10^{-4} \mathrm{Re}_p^{1.38} \tag{2.8}$$

Re_p is the nucleus Reynolds number, defined as $\mathrm{Re}_p \equiv \frac{2R|\mathbf{w} - \mathbf{w}_p|}{\nu_f}$, ν_f is the kinematic viscosity of the fluid.
The added mass force is due to the surrounding liquid which needs to be accelerated along with the bubble. The drag force is due to the relative velocity of the bubble to the flow. The pressure force is due to the pressure gradient in the flow in combination with the density difference between the bubble and the liquid.
The force balance leading to the equation of motion is discussed in more detail in Chapter 6. The elemental components of the total force balance have been used for this force balance.

The dimensionless form of the equation of motion can be found in Eq. 2.9.

$$\frac{d\hat{\mathbf{w}}_p}{d\hat{t}} = \frac{18}{\hat{R}^2 \mathrm{Re}_f} \frac{\mathrm{Re}_p C_D}{24} (\hat{\mathbf{w}} - \hat{\mathbf{w}}_p) - \frac{3}{2} \nabla C_p \tag{2.9}$$

Dimensionless variants of their dimensionfull counterparts are denoted by a hat. The inflow velocity, U_0, and the half ultimate body width, h, are used to non-dimensionalize. The dimensionless locations are denoted by the coordinate (x, y) for writing convenience. Re_f is the flow Reynolds number defined as: $\mathrm{Re}_f \equiv \frac{U_0 h}{\nu_f}$, and C_p is the pressure coefficient.

2.3 Application to a two-dimensional half body in an infinite fluid

The flow field which will be used is a potential flow field. The benefit of a potential flow field is that with the superposition of very basic elements an analytically defined flow field can be found. The elements used in this case are uniform flow and a source at the origin. The source strength is chosen such that the stagnation point is in $(x, y) = (-\frac{1}{\pi}, 0)$. The resulting body shape is given in Eq. 2.10.

$$x = -y \cot \pi y \tag{2.10}$$

The flow velocities are given in Eq. 2.11.

$$\begin{aligned} \hat{u} &= 1 + \frac{1}{\pi} \frac{x}{x^2 + y^2} \\ \hat{v} &= \frac{1}{\pi} \frac{y}{x^2 + y^2} \end{aligned} \tag{2.11}$$

Finally the pressure gradient is given in Eq. 2.12.

$$\begin{aligned} -\frac{\partial C_p}{\partial x} &= -\frac{2}{\pi} \frac{x^2 - y^2 + \frac{x}{\pi}}{(x^2 + y^2)^2} \\ -\frac{\partial C_p}{\partial y} &= -\frac{2}{\pi} \frac{y\left(2x + \frac{1}{\pi}\right)}{(x^2 + y^2)^2} \end{aligned} \tag{2.12}$$

The full derivation of the flow field can be found in Appendix B. Using the velocity and the pressure gradient Eq. 2.9 can be completed.
The flow field is visualized in Figure 2.1, the maximum pressure coefficient is $C_{p,max} = 1$ and the minimum pressure coefficient is $C_{p,min} = -0.58$.

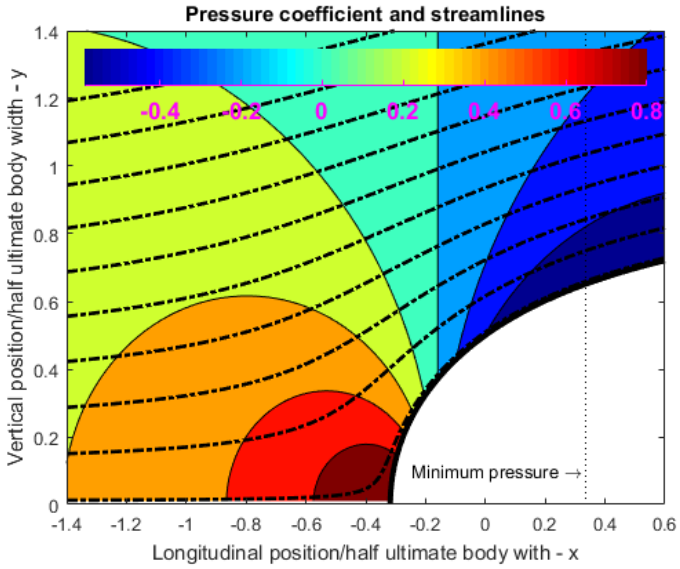

Figure 2.1: Flow visualization via the pressure coefficient and the streamlines.

2.4 Solving the system of ODE's

The resulting equations of motion are second-order coupled non-linear ODE's, which can be solved via numerical integration. Most of these numerical integration schemes are designed to solve systems of first-order ODE's efficiently, therefore the set of second-order ODE's will be reduced to a system of first-order ODE's. The resulting order reduction can be seen in Eq. 2.13. For the derivation see Appendix C.

$$\frac{d\mathbf{z}}{d\hat{t}} = \begin{bmatrix} \frac{18}{\hat{R}^2 \mathrm{Re}_f} \frac{\mathrm{Re}_p C_D}{24} \left[\left(1 + \frac{1}{\pi} \frac{x_p}{x_p^2 + y_p^2} \right) - \dot{x}_p \right] - \frac{3}{\pi} \left[\frac{x_p^2 - y_p^2 + \frac{x_p}{\pi}}{(x_p^2 + y_p^2)^2} \right] \\ \dot{x}_p \\ \frac{18}{\hat{R}^2 \mathrm{Re}_f} \frac{\mathrm{Re}_p C_D}{24} \left[\left(\frac{1}{\pi} \frac{y_p}{x_p^2 + y_p^2} \right) - \dot{y}_p \right] - \frac{3}{\pi} \left[\frac{y_p \left(2x_p + \frac{1}{\pi} \right)}{(x_p^2 + y_p^2)^2} \right] \\ \dot{y}_p \end{bmatrix}, \mathbf{z} = \begin{bmatrix} \dot{x}_p \\ x_p \\ \dot{y}_p \\ y_p \end{bmatrix} \tag{2.13}$$

The numerical integration scheme which will be used is the Runge-Kutta scheme. This scheme will be incorporated via the ode functions in MATLAB, since these have adjusted time stepping, which speeds up the process significantly. At every time step the velocity and position will be updated, just like the bubble radius and nucleus Reynolds-number.

Although no initial conditions on the velocities are mentioned by [2], zero initial conditions seemed to be used. Changing the initial horizontal location (second Figure in [2]) is only influential if these initial conditions are used, see Eq. 2.14.

$$\mathbf{z}_0 = \begin{bmatrix} u_{p,0} = 0 \\ x_{p,0} = x_{p,0} \\ v_{p,0} = 0 \\ y_{p,0} = y_{p,0} \end{bmatrix} \tag{2.14}$$

2.5 Results

In this part, the results will be discussed and compared with the results of [2].

2.5.1 Variation of the initial vertical position

The effect of the vertical initial location on the nucleus path is examined first. The trajectory of a bubbles with $y_{p,0}$ = [0.01 0.02 0.05 0.1 0.2] is shown in Figure 2.2.

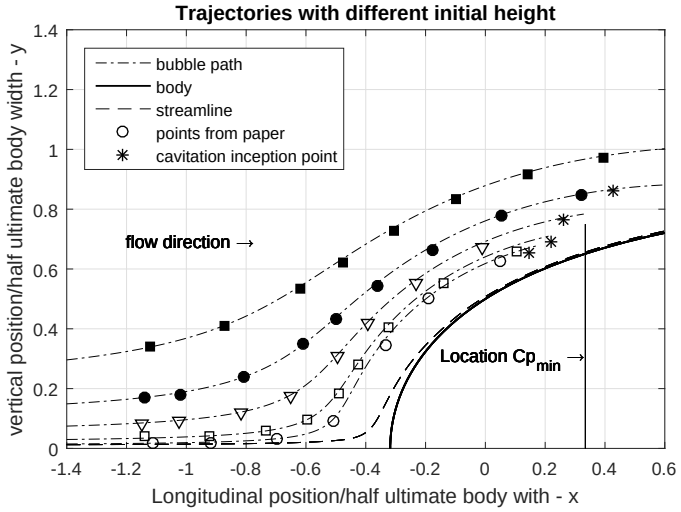

Figure 2.2: Trajectories with different initial height $y_{p,0}$ = [0.01 0.02 0.05 0.1 0.2], U_0 = 15.24 ms^{-1}, h = 15.24 mm and R_0 = 305 μm. The reference points are from [2].

The resulting trajectories compare quite good with the data from [2], however the trajectories are overall slightly higher.

2.5.2 Variation of initial radius

The trajectories of a range of initial radii are being compared to the trajectories with the same initial radii as in [2], see Figure 2.3.

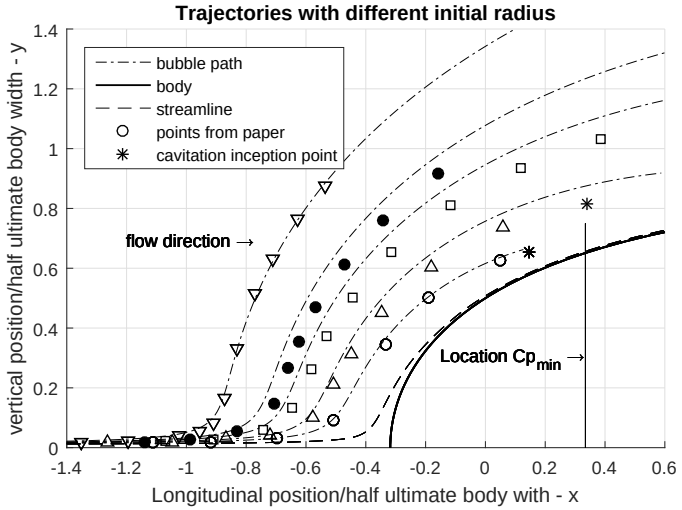

Figure 2.3: Nuclei trajectories with $\hat{R}_0$ = [0.24 0.12 0.08 0.04 0.02], $U_0 = 15.24\,ms^{-1}$, $h = 15.24\,mm$. The reference points are from [2].

It can be seen that the calculated trajectories deviates significantly from the reference points in [2] in some cases ($\hat{R}_0$ = [0.12 0.08 0.04]). The trajectories with $\hat{R}_0$ = [0.24 0.02] (furthest away from the body and closest to the body) are reasonably comparable. In Figure 2.3 the screening effect can be seen, large bubbles do not grow exponentially due to the higher encountered pressures.

The dimensional radii used in [2] range from $R_0 = [300 - 3658]\,\mu m$. Compared to the range found in [1] ($R_0 = [5 - 500]\,\mu m$) the nuclei are rather large. However, it shows the screening effect clearly.

2.5.3 Varying the cavitation number

In [2] the cavitation number is changed from $\sigma_v = 0.4$ to $\sigma_v = 0.2$ and $\sigma_v = 0.58$. Changing the cavitation number influences the growth of the nucleus. Assymptotic growth of a bubble, which occurs past the critical radius, is called cavitation inception. The sixth Figure in [2] shows the growth of a nucleus with different cavitation numbers. The growth of a nucleus with different cavitation numbers can be seen in Figure 4(a).

The bubble growth of $\sigma_v = 0.58$ is slightly smaller than the nucleus growth calculated in [2] with the same cavitation number ($\frac{R_{max}}{R_0} \approx 2.6$), see Figure 4(b). This is due to the slightly higher trajectory which leads to encountering higher pressures. The corresponding trajectories can be seen in Figure 2.5.

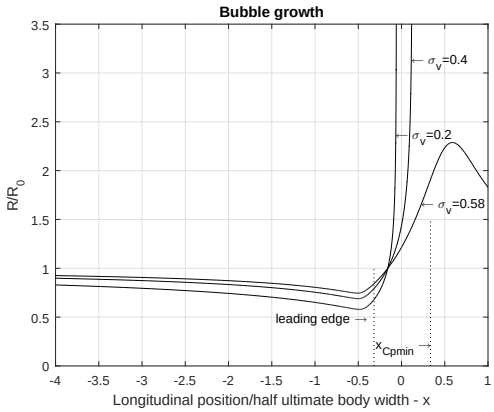

(a) Variation of the size of a gas nucleus along its trajectory with $y_{p,0} = 0.01$, $U_0 = 15.24\,ms^{-1}$, $h = 15.24\,mm$ and $R_0 = 305\,\mu m$.

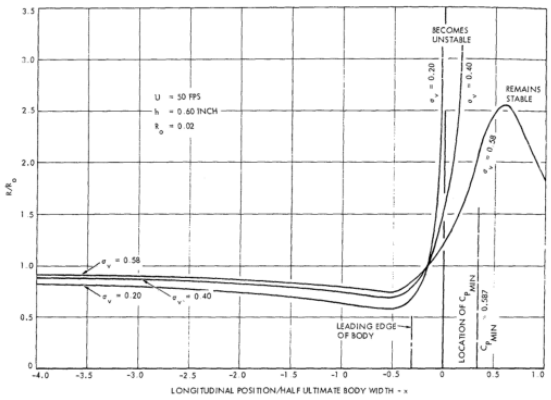

(b) Reference figure found in [2]

Figure 2.4: Comparison of the found variation of the size of a bubble with [2].

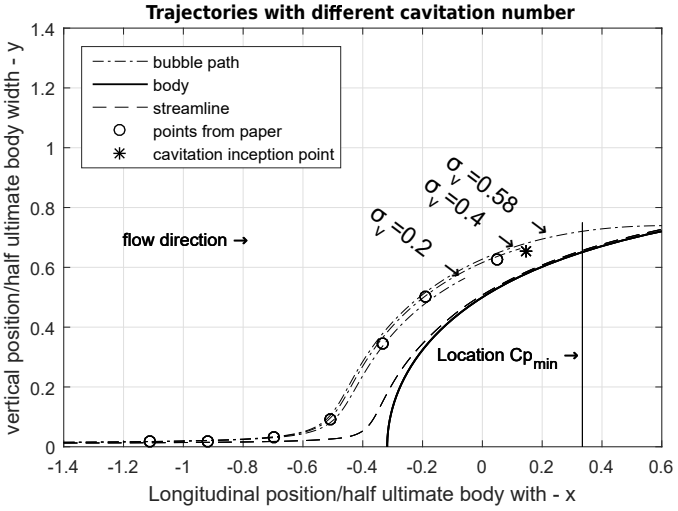

Figure 2.5: Nucleus trajectories with different cavitation numbers, $y_{p,0} = 0.01$, $U_0 = 15.24\,ms^{-1}$, $h = 15.24\,mm$ and $R_0 = 305\,\mu m$. The reference points are from [2] with $\sigma_v = 0.4$.

The cavitation number can be controlled in experiments by changing the ambient pressure. Changing the surrounding pressure however, influences the nuclei distribution. A lower ambient pressure leads to larger bubbles and can, due to gravity, lead to a layered nuclei spectrum in a horizontal test section. Near the headform, nuclei could be smaller than the initially measured spectrum.

2.6 Influence of the discretization

The results found in the previous section are not the same as in [2]. A suggestion on the cause of this discrepancy might be the temporal step involved in solving the coupled differential equation. The time step is namely variable in this report. Another possible cause could be the discretization scheme. The time step and solving procedure used in [2] are unknown.

The Runge-Kutta method is named, but past the point where the trajectories are calculated. To visualize the influence of the discretization scheme and the time step a forward Euler discritization is used, see Figure 2.6.

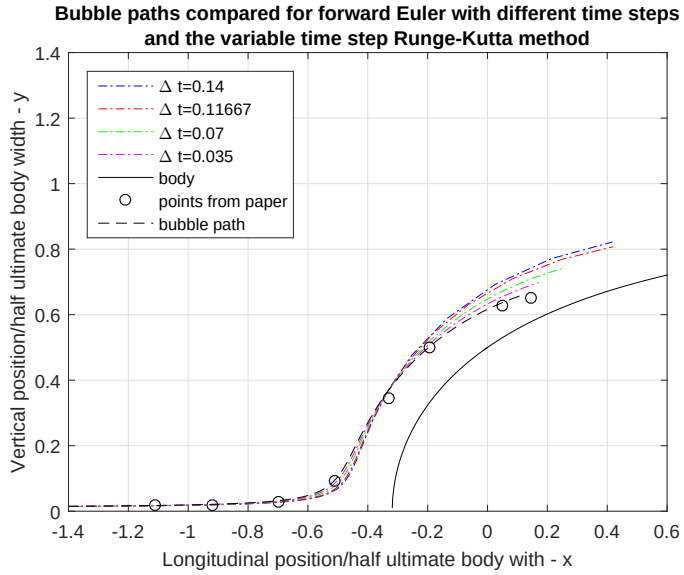

Figure 2.6: Nucleus path with a different discretization and a fixed time step, $y_{p,0} = 0.01$, $U_0 = 15.24\,ms^{-1}$, $h = 15.24\,mm$ and $R_0 = 305\,\mu m$. The reference points are from [2].

The variations of the discretization and the time step rejects the hypothesis of a discrepancy due to the discretization or time step. The trajectories will not get closer to the trajectory found in [2]. The cause of the different results will thus remain unknown.

3 Scale effects in the cavitation inception model

Scale effects are examined within the limitations of the current model. The influence of characteristic variables, h, U_0 and $\hat{R}_0$ will be discussed.

3.1 Main dimensionless numbers

The trajectory and the nucleus growth are calculated simultaneously, therefore the scale effects can be subdivided into two categories, namely the scale effects on the trajectory and the scale effects on the nucleus growth. To distinguish between these scale effects, the equivalent Stokes number and the Weber number can be used. The equivalent Stokes number is given in Eq. 3.1.

$$\mathrm{Stk}_{eq} = \frac{\hat{R}^2 \mathrm{Re}_f}{18} \tag{3.1}$$

The equivalent Stokes number measures the characteristic time scale of the particle relative to the characteristic time scale of the flow, the derivation can be found in Appendix D. Since the equivalent Stokes number has the radius of the nucleus in the definition, the nucleus growth is affecting this number. Therefore, the equivalent Stokes number at the initial condition will be used and is given in Eq. 3.1.

$$\mathrm{Stk}_{eq0} = \frac{\hat{R}_0^2 \mathrm{Re}_f}{18} \tag{3.2}$$

The equivalent initial Stokes number will be used for the scale effects on the trajectory.
The Weber number is used for the scale effects on the growth of the nucleus. The most adequate definition of the Weber number for this model has been given in [3] as:

"The dimensionless Weber number represents the ratio of disruptive hydrodynamic forces to the stabilizing surface tension force. Hence, the Weber number indicates whether the kinetic or the surface tension energy is dominant."

According to [3], a higher Weber number means that the bubble is less stabilized by the surface tension. A less stable bubble will deform easier, deformation can occur in the form of changing shape and in the form of changing size. The changing shape can not be included in the model. The Weber number will thus only be used to estimate radial changes, which is a limit in the model. The Weber number in terms of the dimensionless initial radius is given in Eq. 3.3.

$$\mathrm{We} = \frac{2\rho_f U_0^2 \hat{R}_0 h}{\gamma} \tag{3.3}$$

The equation of motion, given by Eq. 2.9, can be rewritten, using Eq. to Eq. 3.4.

$$\frac{d\hat{\mathbf{w}}_p}{d\hat{t}} = \underbrace{\frac{R_0^2}{R^2}\frac{1}{\mathrm{Stk}_{eq0}}\frac{C_D\mathrm{Re}_p}{24}}_{\text{determines normal distance}} (\hat{\mathbf{w}} - \hat{\mathbf{w}}_p) - \frac{3}{2}\hat{\nabla}C_p \tag{3.4}$$

Where $\frac{R_0^2}{R^2}$ is a function of the Weber number and $\frac{C_D\mathrm{Re}_p}{24}$ is a function of both the equivalent Stokes number at the initial condition and the Weber number. For Stokes flow the term $\frac{C_D\mathrm{Re}_p}{24}$ will reduce to 1.
The trajectory of the nucleus follows from Eq. 3.4, and can only be altered if the term in front of the relative velocity is altered. Which in turn can only be altered if either the Weber number changes or the equivalent initial Stokes number. Shortly, if the term in front of the relative dimensionless velocity decreases, larger relative velocities are allowed leading to larger deviations from the streamline.
Deviations from the streamline or similarly normal distances from the body are of interest as the nucleus encounters higher pressures if it is further away from the body. *Screening* occurs when the bubble is pushed over the region where the pressure is low enough for the bubble to induce cavitation inception.

3.2 Small nuclei in the Stokes limit

For small nuclei in the Stokes limit, the normal distance from the streamline is proportional to the equivalent Stokes number. This can be seen in Eq. 3.4 as in the Stokes limit the drag factor, $\frac{C_D\mathrm{Re}_p}{24}$, is 1. The derivation of this analytical relation, based on [4] can be found in Appendix E.
Small nuclei have an initial dimensionless radius that fulfills $\hat{R}_0 < 0.002$ for $h = 15.24\,mm$ and $U = 15.24\,ms^{-1}$, see Appendix D. Eq. 3.4 has been checked using the normal with an angle of $\alpha = 45^\circ$ (see Figure 3.3). The streamline is approximately parallel to the body using this normal and the largest pressure gradients have been encountered. In Figure 3.1, the found normal distances as a function of the initial dimensionless nucleus radius along with a fitted curve have been given. The fitted second order polynomial shows that indeed second order behavior is found.

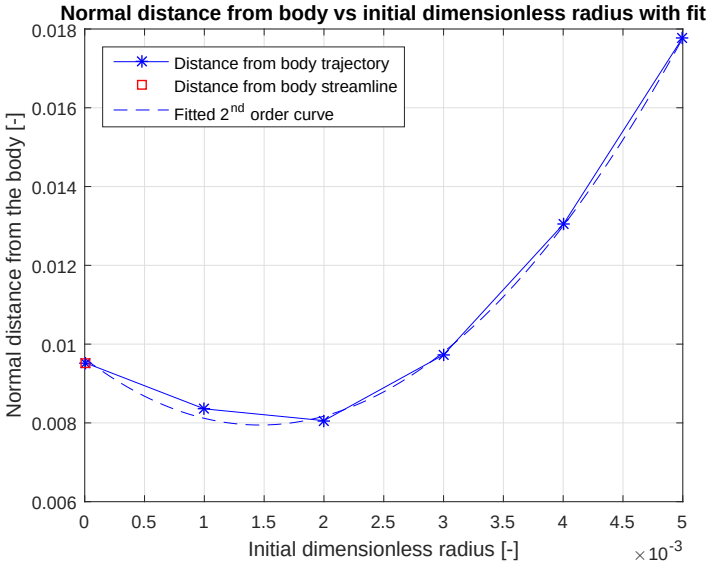

Figure 3.1: Normal dimensionless distance from the body for $h = 15.24\,mm$ and $U = 15.24\,ms^{-1}$.

In Figure 3.2 the first order behavior regarding the flow Reynolds number has been checked. The initial dimensionless nucleus radius is $\hat{R}_0 = 0.002$. As the flow Reynolds number increases, the distance from the body tends to get first order $0.3 \cdot 10^6 < \mathrm{Re}_f < 10^6$. For very low Reynolds numbers however, the nucleus would follow the streamline closer, the range of flow Reynolds number of $0 < \mathrm{Re}_f < 0.3 \cdot 10^6$ will hardly be affected by screening, and will thus not scale likewise.

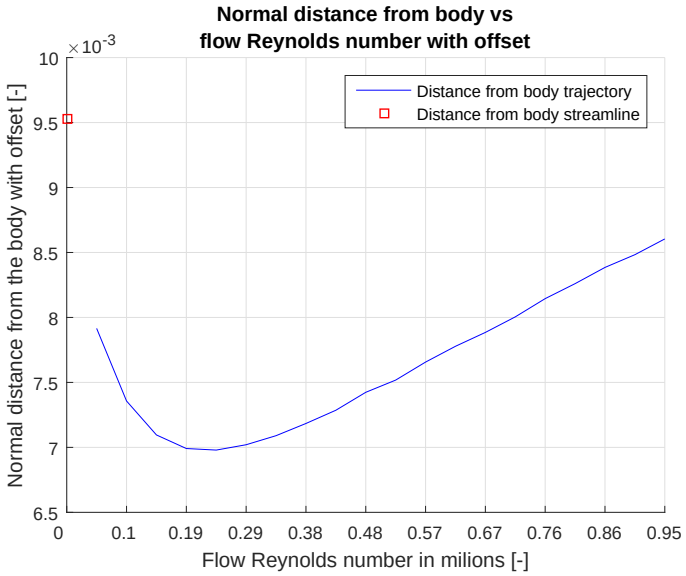

Figure 3.2: Normal dimensionless distance from the body for $\hat{R}_0 = 0.002$.

3.3 Dimensionless distance from body

For large initial bubble radii the scaling laws will be re-examined. The influence of the drag factor ,$\frac{C_D \mathrm{Re}_p}{24}$, will be significant, as it deviates from 1.

Both the equivalent initial Stokes number and the Weber number are altered by the half ultimate body width, the free stream velocity and the initial dimensionless radius. First the scale effects regarding the dimensionless distance from the body are examined. Four lines normal to the body have been taken as a reference. The normal lines are determined by their angle with respect to the $-x$-axis. An angle of 0° means the normal is taken at the stagnation point. An angle of 90° is approached when $x \to \infty$, see Figure 3.3.

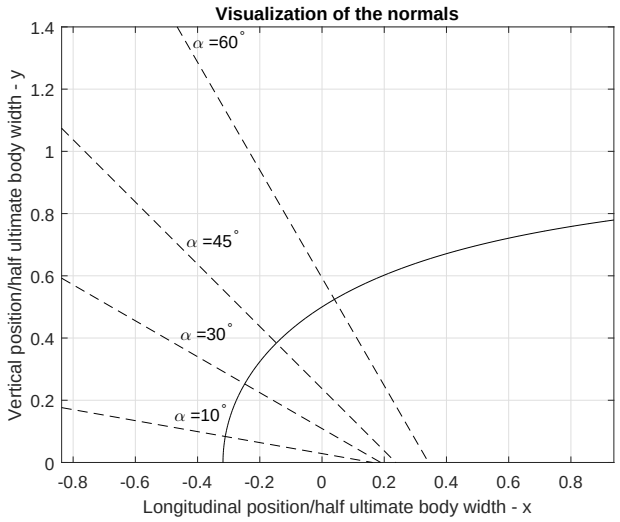

Figure 3.3: Outward normals used for the normal distances.

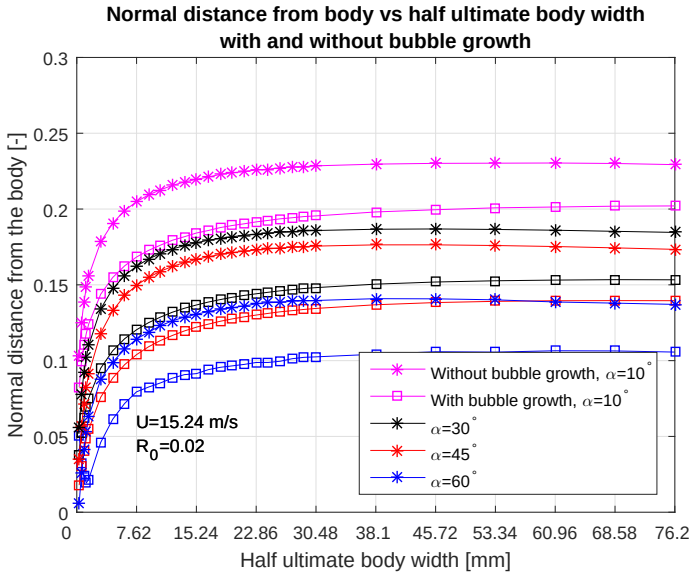

Figure 3.4: Normal distance from the body plotted against the half ultimate body width for different normals, with (square) and without (asterisk) nucleus growth. $y_{p,0} = 0.01$, $U_0 = 15.24\, ms^{-1}$ and $R_0 = 305\, \mu m$.

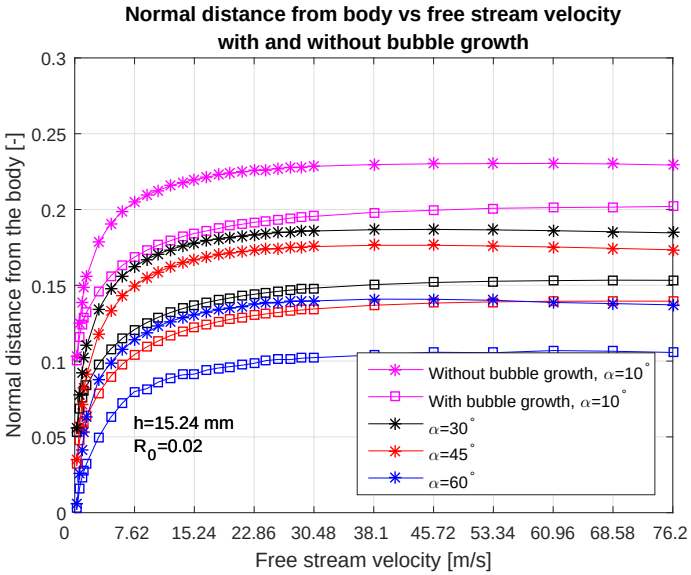

Figure 3.5: Normal distance from the body plotted against the free stream velocity for different normals, with (square) and without (asterisk) nucleus growth. $y_{p,0} = 0.01$, $h = 15.24\,mm$ and $R_0 = 305\,\mu m$.

In Figures 3.4-3.5 it can be seen that changing the half ultimate body width and changing the free stream velocity yield the same result in the absence of nucleus growth. The only influential factor is the initial equivalent Stokes number, in which via the flow Reynolds number (see Eq. 3.1) the half ultimate body width and free stream velocity are causing equal scale effects.
In the same Figures it can be seen that the growth of the nucleus reduces the normal distance from the body. This is caused by the nucleus shrinking towards the body, making it follow the streamline more closely when the repulsive pressure gradients are encountered.
The way the nucleus growth influences the normal distance from the body seems to be independent of the variable parameter. This yields that the magnitude of the Weber number does not influence the nucleus growth in a significant way within the investigated range. The Weber number does not react likewise to both parameters (linear increase when h is increased and quadratic increase when U_0 is increased), the normal distance however does. The Weber number variation is irrelevant as the Weber number is large in both cases. A large Weber number would mean significant change of shape, this effect can not be captured in the model. In this range of large Weber numbers the deformation will mostly be shape wise.

Changing the initial dimensionless nucleus radius has been done in [2], see Figure 2.3. The same steps in the initial dimensionless radius have been taken for both with and without nucleus growth, see Figure 3.6. As discussed, the current model overestimates the results of [2]. The nucleus growth reduces the distance to the body, this is due to the shrinking of the nucleus towards the stagnation point.

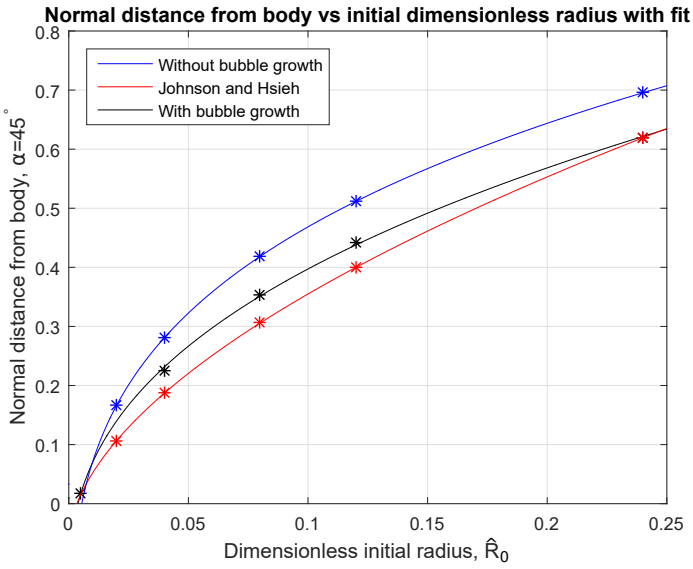

Figure 3.6: Comparison between [2] and the outcome of the model with and without nucleus growth.

For the three main parameters, the half ultimate body width, the free stream velocity and the initial dimensionless radius, holds that increasing them individually leads to a larger distance from the body. Screening occurs on the larger (dimensionless) nuclei, see Figure 3.6, and is then influenced by the flow Reynolds number, see Figures 3.4-3.5. Screening is thus an effect which could prevent larger nuclei from cavitating.

3.4 Characterization of cavitation inception

Cavitation inception occurs in many forms. For this model, distinction between off-body cavitation inception and on-body cavitation inception is made. Off-body cavitation inception occurs when the nucleus becomes unstable before the center of the bubble hits the body. On-body cavitation inception occurs when the middle point of the nucleus hits the body before the minimum pressure point and will get unstable when it travels along the body towards the minimum pressure point.
The cavitation inception type (on- or off-body) is influenced by the cavitation number and is different for different initial nuclei radii while the body size and the free stream velocity are kept constant. This can be seen in Figure 3.7, the figure is similar to figure 7 in [2].

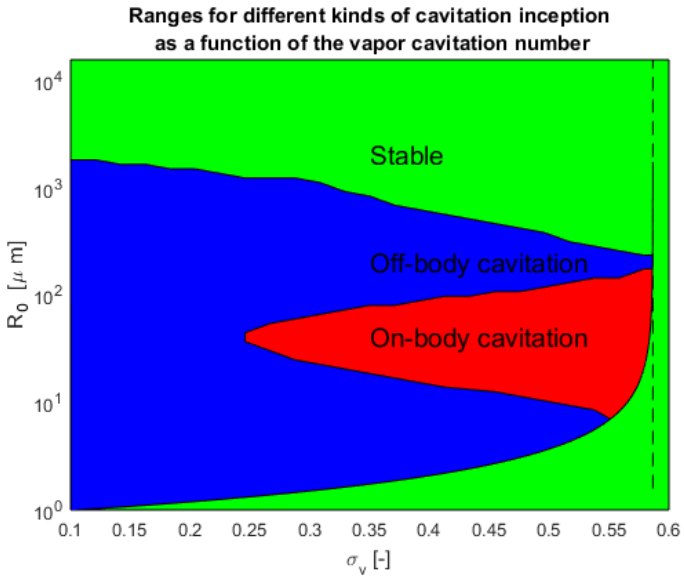

Figure 3.7: Different kinds of cavitation inception as a function of the vapor cavitation number, with $y_{p,0} = 0.01$, $U_0 = 15.24\,ms^{-1}$ and $h = 15.24\,mm$.

Figure 3.7 will be explained by means of moving upward in the figure, for example at $\sigma_v = 0.4$.
The lower limit depends on the minimum pressure the nucleus could encounter. This means that the lower limit depends on the initial conditions. As a conservative estimate of this lower limit Eq. 2.5 could be solved for the Weber number and thus the nucleus radius with $C_p^* = C_{p_{min}}$. This conservative lower limit is used in [2]. In other words, the nucleus is so small that the surface tension keeps it stable even at the minimum pressure point. This is the green region below the lowest limit.

The lower boundary between off-body cavitation inception and on-body cavitation inception declines for increasing cavitation number until on-body cavitation is the lower limit. In case of on-body cavitation inception, the lower limit is not conservative as it is assumed that the center of the bubble starts moving along the surface of the object towards the minimum pressure point. When the cavitation number increases, bubbles which would cavitate for lower cavitation numbers near the body remain stable and hit the body, after which they eventually cavitate, leading to on-body cavitation. In practice, off- or on-body cavitation events will not be clearly distinguishable since a cavitating nucleus near the surface would hit the surface shortly after becoming unstable. Furthermore, the distinction between both events is currently made based on the center of the bubble, meaning that the bubble interface may already have hit the body.

The upper boundary between on-body cavitation inception and off-body cavitation inception inclines for increasing cavitation number. Larger nuclei will remain stable in lower pressures and thus will have more chance of hitting the body before the minimum pressure point. Again, in reality the distinction between both regions will be less clear.

The boundary between off-body cavitation inception and stable is declining since a nucleus along the same trajectory will remain stable when the cavitation number is higher.

The resolution of Figure 3.7 makes that the upper triple point in this figure is not visible. The upper on-body cavitation inception line, the upper off-body cavitation inception line and the

stable line should intersect in one point. In this point a nucleus with a given initial height will be screened just that much that the nucleus will hit the body exactly in the minimum pressure point. Such a nucleus can be categorized as off-body cavitation inception and as on-body cavitation inception, the slightest deviation in initial size could make the nucleus stable, just as the slightest pressure disturbance.

3.5 Parameter study

The transition between different cavitation inception regions discussed previously depend on the initial dimensionless height, the free stream velocity and the half ultimate body width. To investigate the way in which Figure 3.7 is altered when any of these parameters is altered, slices of Figure 3.7 will be made at two cavitation numbers, namely $\sigma_v = 0.4$ and $\sigma_v = 0.55$.

3.5.1 Initial dimensionless height

As the initial dimensionless height, y_0, increases, less low pressures will be encountered by the nucleus. Therefore, the range of nuclei available for cavitation inception will shrink. In Figure 3.8 the effect of a higher initial position can be seen. A lower cavitation number leads to a larger range of initial conditions in which the nuclei will cavitate. The range for on-body cavitation inception however, shrinks for a lower cavitation number. This is in accordance with Figure 3.7, at a lower cavitation number nuclei near the body will cavitate instead of/before hitting the body.

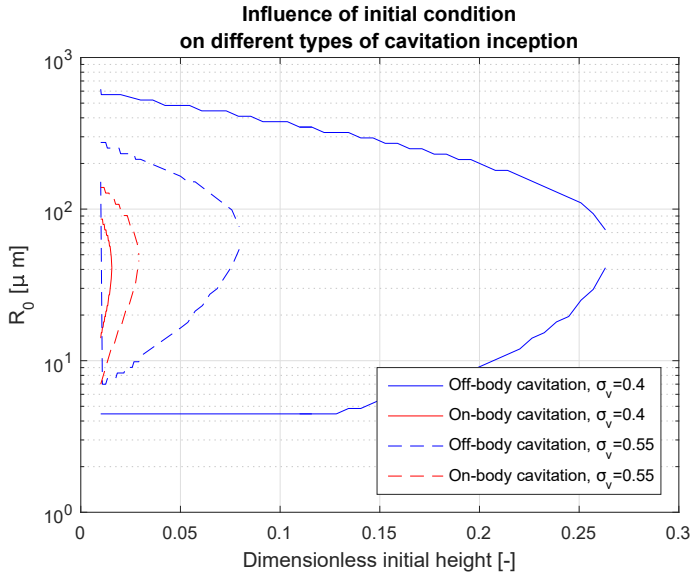

Figure 3.8: Influence of the initial dimensionless height on different types of cavitation inception.

3.5.2 Free stream velocity

Increasing the free stream velocity increases the Weber number, nuclei are thus less stable, and especially smaller nuclei will get available for cavitation inception. Furthermore, a higher velocity increases the equivalent Stokes number, leading to more screening in most

cases, see Figure 3.5. Which leads to larger nuclei no longer being available for cavitation inception. In Figure 3.9 the combined effects can be seen. A smaller cavitation number leads to a wider range of available nuclei for cavitation inception. The vertical part of the lines is caused by the transition from on- to off-body cavitation inception in the lower limit. This can be seen in Figure 3.7 around $\sigma_v \approx 0.54$.

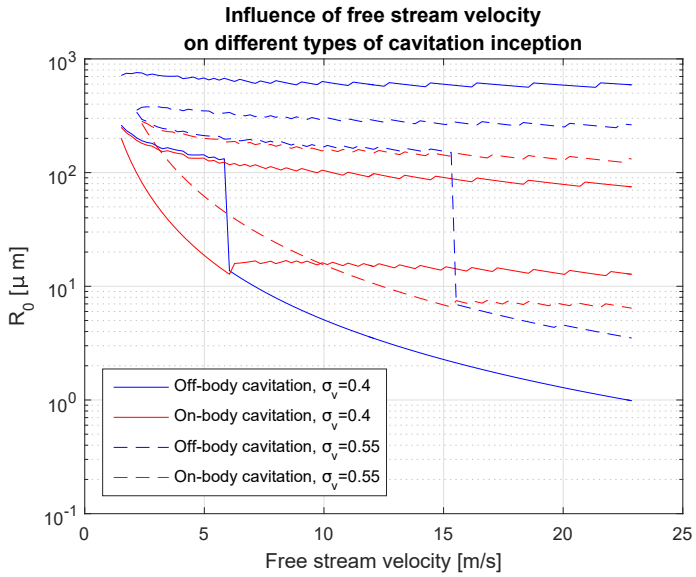

Figure 3.9: Influence of the free stream velocity on different types of cavitation inception.

3.5.3 Half ultimate body width

A larger half ultimate body width leads to a larger Weber number meaning less stable nuclei with a constant dimensionless initial radius. However, the radii are shown in their dimensionfull form. This means that the lower conservative limit will not be affected by the half ultimate body width. This effect can be seen in Figure 3.10. Again, when $\sigma_v = 0.4$ the total range for off-body cavitation inception is larger than for $\sigma_v = 0.55$. The range for on-body cavitation inception for $\sigma_v = 0.4$ is smaller than this range for $\sigma_v = 0.55$. Both observations are in accordance with Figure 3.7.

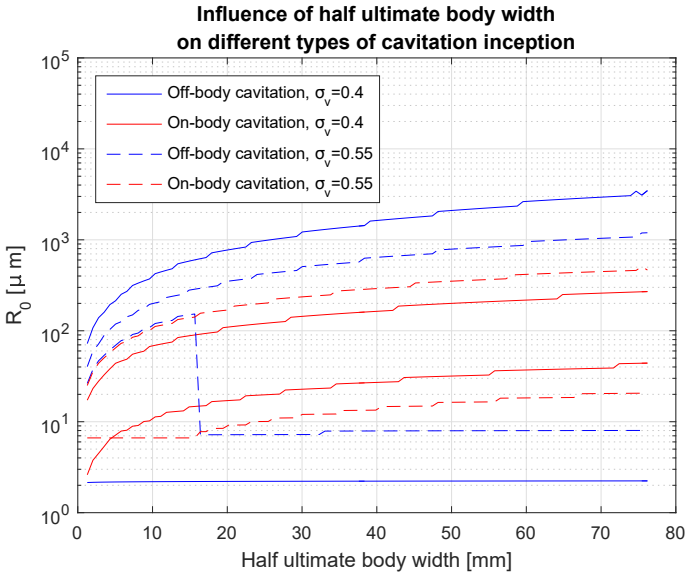

Figure 3.10: Influence of the half ultimate body width on different types of cavitation inception.

3.5.4 Flow Reynolds number

In Figure 3.9 and Figure 3.10 the effect of the flow Reynolds number on the nucleus size available for cavitation inception is inconclusive. The free stream velocity and the half ultimate body width are namely both linear to the Reynolds number, but do not show the same result. So, the resulting effect on the dimensionfull nucleus size of changing the flow Reynolds number depends on how the flow Reynolds number is changed.
The effect of the flow Reynolds number on the dimensionless nucleus size is shown in Figure 3.11. The upper limit for off-body cavitation inception and the limits for on-body cavitation inception are comparable for the free stream velocity and the half ultimate body width. The lower off-body cavitation inception limit however, differs significantly. The lower limit is fully determined by the stability via the Weber number, in which the free stream velocity (quadratic) and the half ultimate body width (linear) are not equivalently taken into account. The three limits determined largely by screening effects are thus insensitive to the way in which the flow Reynolds number is changed as far as the dimensionless nucleus size is concerned, whereas the limit determined by the nucleus stability shows different results for different ways of altering the flow Reynolds number.

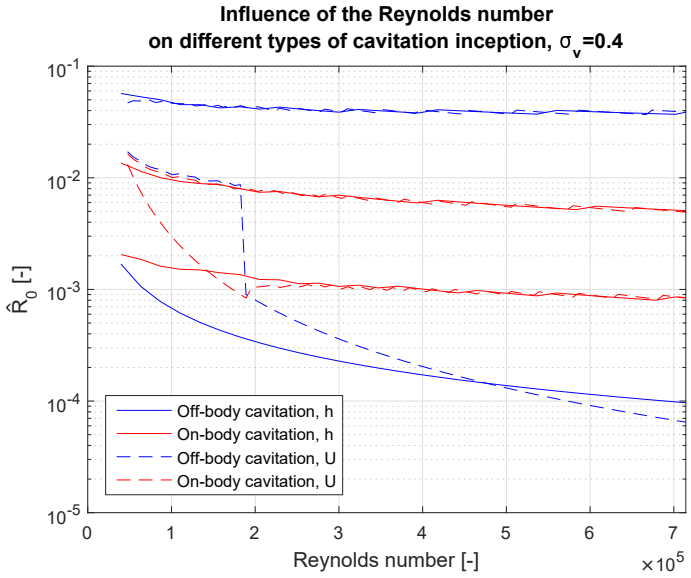

Figure 3.11: Influence of the flow Reynolds number on different types of cavitation inception for $\sigma_v = 0.4$.

3.6 Comparison with literature

Scale effects on cavitation and cavitation inception have been the subjects of many studies ([4],[5],[6],[7]). The mentioned studies focus on the cavitation event rate. The cavitation event rate is the count of measured cavitation occurrences [s^{-1}]. The occurrence of cavitation in experiments is highly dependent on the nuclei spectra available in the oncoming flow, something which has been left out of the consideration thus far. Measuring the cavitation event rate can be done in a variety of ways, via sound, images or as done by [5] and [6] via electrodes in the headforms surface.

The cavitation event rate is dependent on the pressure distribution and thus on the shape of the object, as discussed in [7] (figure 4). The object used by [4],[5],[6] is a Schiebe headform, which is a frequently used headform in cavitation studies. The Schiebe headform is blunt compared to the body used thus far.

The number of cavitation occurrences measured should be directly relatable to the number of cavitation inception occurrences. Lowering the cavitation number leads to more cavitation events [5] (Figure 4). This would be expected when looking at Figure 3.7. The cavitation occurrence is measured at the surface. The occurrence of cavitation inception on the surface and the occurrence of cavitation on the surface are not directly relatable as cavitation inception in the flow can cause cavitation on the surface.

CONFORMAL TRANSFORMATIONS, BUBBLE DYNAMICS AND THE EQUATION OF MOTION

In the second part the nuclei stability will be implemented using a bubble dynamics equation and the screening effect is evaluated in more detail. Non-symmetric conditions are constructed using conformal mapping.

4 Flow field

The flow field is crucial to the motion of the nucleus. Thus far the flow field has been potential flow around a semi-infinite half body. To be able to alter the flow field and be computationally efficient conformal mapping is convenient. The Kármán-Trefftz transform is a conformal transformation which can yield airfoil like shapes with finite trailing edge angles. The Kármán-Trefftz transform (given in Appendix D from the Fluid Dynamics Lecture Notes by H.W.M. Hoeijmakers) is defined in Eq. 4.1.

$$z = 2a\frac{1+f(\zeta)}{1-f(\zeta)} \quad \text{Where} \quad f(\zeta) = \left(\frac{\zeta - a}{\zeta + a}\right)^n \tag{4.1}$$

In the z-plane the transformed flow field is the solution. In the ζ-plane, the potential flow solution around a cylinder in 2D is used. Both planes are complex. a is the location at which the cylinder crosses the ξ-axis in the ζ-plane, and thus given by $a = \sqrt{R_{cyl}^2 - \eta_0^2} - |\xi_0|$. R_{cyl} is the radius of the cylinder, and $\zeta_0 = \xi_0 + i\eta_0$ is the middle point of the cylinder. The location of the middle point of the cylinder is usually in the top left quarter plane and determines the thickness (ξ_0) and the camber (η_0) of the foil. Finally, n determines the trailing edge angle (α_{te}) as: $n = 2 - \frac{\alpha_{te}}{\pi}$. If $n = 2$ the Joukowski transform is retrieved.

To transform the velocity the derivative of the transform is required, see Eq. 4.2.

$$W = \frac{\tilde{W}}{\frac{dz}{d\zeta}} \quad \text{Where} \quad \frac{dz}{d\zeta} = \frac{8na^2 f(\zeta)}{(\zeta^2 - a^2)(1 - f(\zeta))^2} \tag{4.2}$$

The velocity in the transformed z-plane is $W = u - iv$ and the velocity in the computational ζ-plane is $\tilde{W} = u_\xi - iv_\eta$. The minus signs are the consequence of preserving the complex potential.

The flow in the computational frame is described by the potential in polar coordinates given in Eq. 4.3.

$$\phi = U_0\left(r + \frac{R_{cyl}^2}{r}\right)\cos(\theta - \alpha) - \frac{\Gamma}{2\pi}\theta \tag{4.3}$$

In Eq. 4.3 α is the angle of attack of the flow. Γ is the circulation which is conserved within the transformation, meaning that the cylinder produces as much lift as the foil. The circulation is set such that the stagnation point of the cylinder gets transformed to the trailing edge of the foil, and thus fulfilling the Kutta condition. The circulation therefore depends on the angle of attack and the camber, see Eq. 4.4.

$$\Gamma = -4\pi R_{cyl} U_0 \sin\left(\sin^{-1}\left(\frac{-\eta_0}{R_{cyl}} - \alpha\right)\right) \tag{4.4}$$

The resulting flow field can be seen in Figure 4.1

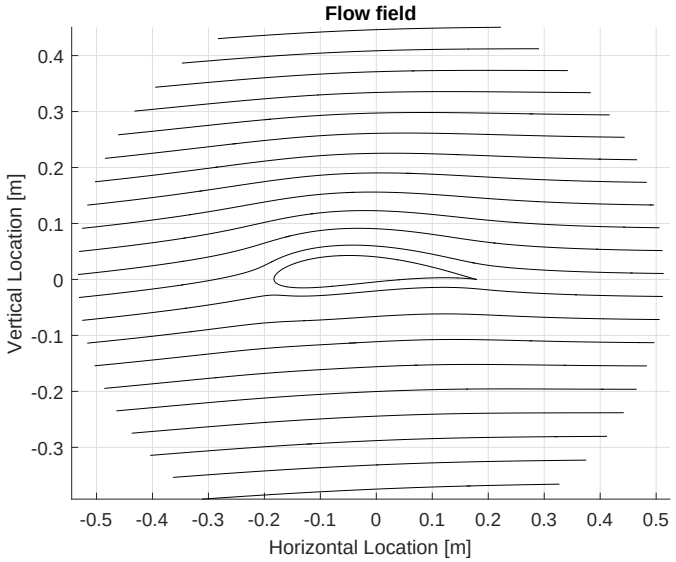

Figure 4.1: The flow field as a result of the Kármán-trefftz transform with $R_{cyl} = 0.1\,m$, $\xi_0 = 0.01\,m$, $\eta_0 = 0.01\,m$, $\alpha_{te} = 10^\circ$ and $\alpha = 2.5^\circ$.

The pressure coefficient in the z-plane can be calculated using Eq. 4.5.

$$C_p = 1 - \frac{u^2 + v^2}{U_0^2} \tag{4.5}$$

The pressure gradient is determined numerically via Eq. 4.6. The scheme is second order accurate except when the body is within range of $\Delta x = \Delta y = h$ the scheme works in one direction, and is therefore first order. h should be small compared to the length scale of the flow.

$$\frac{dC_p}{dx} \approx \frac{C_{p,\mathbf{x}+\Delta x} - C_{p,\mathbf{x}-\Delta x}}{2\Delta x}, \quad \frac{dC_p}{dy} \approx \frac{C_{p,\mathbf{x}+\Delta y} - C_{p,\mathbf{x}-\Delta y}}{2\Delta y} \tag{4.6}$$

As the flow field is still potential flow viscous effects can not be taken into account.

5 Bubble dynamics

5.1 Rayleigh-Plesset equation

The well known Rayleigh-Plesset equation (Eq. 5.1) can be used to describe the bubble dynamics.

$$\rho_f \left[R\frac{d^2R}{dt^2} + \frac{3}{2}\left(\frac{dR}{dt}\right)^2 \right] = p_v - p + p_g(t) - 2\frac{\gamma}{R} - \frac{4\mu_f}{R}\frac{dR}{dt} \tag{5.1}$$

The derivation of Eq. 5.1 is based on the mass conservation equation and the Navier-Stokes equations. In the derivation a spherical nucleus is assumed. The derivation can be seen in Appendix F.

5.2 The general Keller-Herring equation

The Rayleigh-Plesset equation does only include viscous damping. To derive the Rayleigh-Plesset equation an undisturbed flow field near the nucleus is assumed, meaning that particularly during the collapse of a nucleus the radiation of a sound wave is omitted. In the general Keller-Herring equation the energy loss due to the emitted sound wave is taken into account. The general Keller-Herring equation is derived in Appendix F. The outcome can be seen in Eq. 5.2.

$$\begin{aligned} &\left(1 - (\lambda+1)\frac{\frac{dR}{dt}}{c}\right)\rho_f R\frac{d^2R}{dt^2} + \frac{3}{2}\left(\frac{dR}{dt}\right)^2\rho_f\left(1 - (\lambda+\frac{1}{3})\frac{\frac{dR}{dt}}{c}\right) = \\ &\left(1 + (1-\lambda)\frac{\frac{dR}{dt}}{c}\right)\left[p_v - p + p_g(t)\right] + \frac{R}{c}\frac{dp_g(t)}{dt} - 4\mu_f\frac{\frac{dR}{dt}}{R} - \frac{2\gamma}{R} \end{aligned} \tag{5.2}$$

The speed of sound in water is taken into account in Eq. 5.2 as $c = 1481\, ms^{-1}$.
If the factor $\lambda = 0$ the Keller-Miksis equation is found, and if $\lambda = 1$ the equation used by Herring and Trilling is found, λ will be 0 unless mentioned otherwise.
Both the derivation of the Rayleigh-Plesset equation and the derivation of the general Keller-Herring equation is supported by [8] and [9]. The equation of state for a perfect gas will be used for the gas pressure ($p_g(t)$) in the nucleus.

6 Equation of motion

The equation of motion will be discussed in this chapter term wise. The equation of motion is based on the force balance on the nucleus, the terms are thus different forces. Forces due to unsteadiness or due to viscous effects in the flow are not discussed as potential flow is assumed.

6.1 Mass of the nucleus

The mass of the nucleus is particularly influential when the nucleus is a solid particle with a higher density than the surrounding fluid. The mass of a nucleus is defined in Eq. 6.1.

$$m_p = \rho_p \frac{4}{3} \pi R_0^3 \tag{6.1}$$

The mass of a gas nucleus will thus not change when the volume changes as no mass transfer is assumed. In the case of a gas nucleus the mass term will be negligible, but is still taken into account as the equation of motion will be suitable for both solid particles and gas nuclei.

The force as a consequence of the mass of the nucleus and is given in Eq. 6.2.

$$\mathbf{F}_m = m_p \frac{d\mathbf{w_p}}{dt} \tag{6.2}$$

6.2 Kelvin impulse

From impulses forces can be derived. The Kelvin impulse is mentioned specifically as an impulse as it is related to the collapse of gas nuclei. The definition of the Kelvin Impulse ([10],[11]), **I**, can be seen in Eq. 6.3.

$$\mathbf{I} = \rho_f \iint_S \phi \mathbf{n} dS \tag{6.3}$$

Where ϕ is the velocity potential, **n** is the inward unit normal of the nucleus and S is the surface of the nucleus. For a moving spherical nucleus in an infinite fluid the resulting Kelvin impulse can be found in Eq. 6.4.

$$\mathbf{I} = C_{am} \rho_f \frac{4}{3} \pi R^3 (\mathbf{w} - \mathbf{w_p}) \tag{6.4}$$

In which C_{am} is the added mass coefficient. The added mass coefficient depends, among others, on the distance from the wall ([12],[13],[14],[15],[16]). The assumption of an infinite fluid will thus be critical when the nucleus gets near the object in the flow. The dependency of the added mass of a spherical nucleus approaching the wall, [12], can be seen in Figure 6.1.

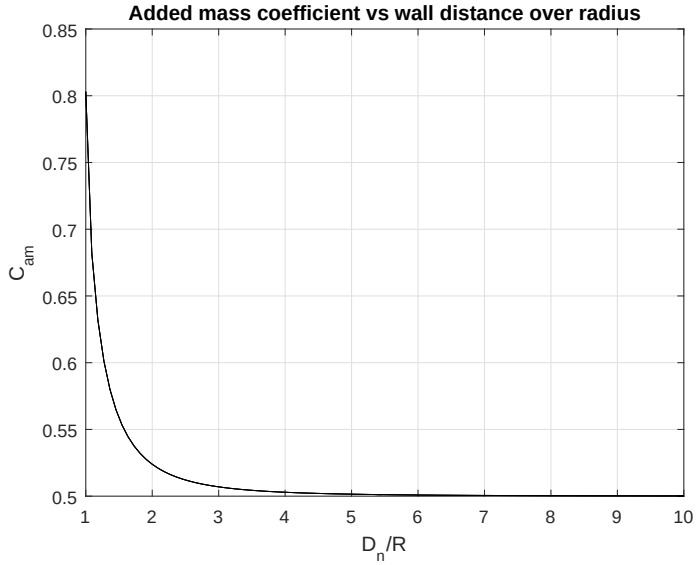

Figure 6.1: Emperical relation for the added mass as a function of the normal distance from the wall, D_n.

It can be seen that the coefficient of added mass starts to deviate significantly from $C_{am} = \frac{1}{2}$, which is the limiting value for a nucleus in an infinite fluid, when the nucleus is approximately two times the radius of the nucleus away from the body. If the nucleus is in contact with the body the coefficient of added mass goes to the limiting value of $C_{am}(D_n = R) = 0.803$ ([12]).
The coefficient of added mass will be taken to be $C_{am} = \frac{1}{2}$, it needs to be taken into account that the Kelvin impulse given in Eq. 6.4 will not hold near the wall. The Kelvin impulse near the wall is the subject of many studies as it is associated with the jet towards the wall from a collapsing nucleus [11]. The forces following from the Kelvin impulse can be found by differentiating the Kelvin impulse with respect to time whilst assuming a constant C_{am}, see Eq. 6.5.

$$\frac{d\mathbf{I}}{dt} = C_{am}\rho_f \frac{4}{3}\pi R^3 \frac{d(\mathbf{w} - \mathbf{w_p})}{dt} + C_{am}\rho_f 4\pi R^2 \frac{dR}{dt}(\mathbf{w} - \mathbf{w_p}) \tag{6.5}$$

The influence of the Kelvin impulse on the motion of nuclei can be illustrated by the conservation of only the Kelvin impulse, see Eq. 6.6.

$$I_1 = I_2 \quad \rightarrow \quad R_1^3 U_{r,1} = R_2^3 U_{r,2} \quad \rightarrow \quad U_{r,2} = \left(\frac{R_1}{R_2}\right)^3 U_{r,1} \tag{6.6}$$

In this case, U_r is the relative one-dimensional velocity, and the subscripts 1 and 2 correspond to time t_1 and time t_2 respectively. If the nucleus shrinks, the magnitude of the relative velocity increases. If the nucleus grows, the magnitude of the relative velocity decreases.

The first term on the right-hand side of Eq. 6.5 can be splitted into two forces, see Eq. 6.7.

$$C_{am}\rho_f \frac{4}{3}\pi R^3 \frac{d(\mathbf{w} - \mathbf{w_p})}{dt} = C_{am}\rho_f \frac{4}{3}\pi R^3 \frac{d\mathbf{w}}{dt} - C_{am}\rho_f \frac{4}{3}\pi R^3 \frac{d\mathbf{w_p}}{dt} \tag{6.7}$$

The first term on the right-hand side will be discussed along with the pressure force. The force due to the Kelvin impulse is given in Eq. 6.8.

$$\mathbf{F}_I = -C_{am}\rho_f \frac{4}{3}\pi R^3 \frac{d\mathbf{w_p}}{dt} + C_{am}\rho_f 4\pi R^2 \frac{dR}{dt}(\mathbf{w} - \mathbf{w_p}) \tag{6.8}$$

Using the Kelvin impulse in the equation of motion implies that the Kelvin impulse is being conserved within the equation of motion. The latter is questionable during violent collapses, as the Kelvin impulse is related to flow features related to collapsing nuclei ([10],[11]). Both during collapse ([11]) and the growth ([17]) of a rising nucleus the acceleration and deceleration of the nucleus were observed respectively. Which is an effect of the conservation of the Kelvin impulse within the equation of motion. The fine line between conservation within the equation of motion and conservation within the flow field will yield a condition at which the equation of motion needs to be altered. However this effect will not be incorporated as it is assumed to be marginal. The time in which the Kelvin impulse will not be conserved within the equation of motion is characterized by the Raleigh collapse time, which is much smaller than the particle response time.

6.3 Drag force

The drag force is given in Eq. 6.9.

$$\mathbf{F}_D = \frac{1}{2}\rho_f C_D \pi R^2 (\mathbf{w} - \mathbf{w_p})|\mathbf{w} - \mathbf{w_p}| \tag{6.9}$$

The drag force dependents on the drag coefficient, C_D. The drag coefficient depends on the shape of the nucleus, the interaction between the interior of the nucleus and the surrounding fluid and on the Reynolds number of the nucleus.

6.3.1 Shape

A solid nucleus will be assumed to be spherical which will in general not be the case. Furthermore, the possible roughness is not taken into account.

The shape of a gas nucleus depends on the surface tension, the pressure gradient in the flow and the relative acceleration of the nucleus.
The surface tension tries to prevent the nucleus from deforming into a shape other than spherical. A relatively high surface tension force will result in (close to) spherical nuclei.
The pressure gradient depends among others on the shape of the object in the flow. The direction and the magnitude of the pressure gradient partially determines the shape of the nucleus. Under a constant pressure gradient and at the terminal velocity, the shape of gas nuclei can be predicted. Many studies have focused on nuclei rising under gravity at terminal velocity ([18],[19],[20]). Gravity is then the constant pressure gradient. The Eötvös number, given in Eq. 6.10, is a measure for the deformation of rising gas nuclei.

$$\mathrm{Eo} = \frac{4g(\rho_f - \rho_p)R^2}{\gamma} \tag{6.10}$$

Based on the Eötvös number corrections on the drag relations for gas nuclei have been proposed ([19],[20]). For more general pressure gradients, the counterpart of the Eötvös number, the modified Eötvös number (Eo′), can be written as in Eq. 6.11 if the density of the nucleus is neglected.

$$\mathrm{Eo}' = \frac{4|\nabla p|R^2}{\gamma} \tag{6.11}$$

The larger the modified Eötvös number the more deformation on the basis of the pressure gradient can be expected. The modified Eötvös number can be related to the nucleus Reynolds number and the Weber number as can be seen in Eq. 6.12.

$$\mathrm{Eo}' = \mathrm{WeRe}_p^2 \frac{|\nabla p|\nu_f^2}{2R_0 U_0^2 \rho_f |\mathbf{w} - \mathbf{w_p}|^2} = \mathrm{WeRe}_p^2 \frac{|\nabla C p|\nu_f^2}{2R_0 |\mathbf{w} - \mathbf{w_p}|^2} \tag{6.12}$$

The pressure gradient is mostly responsible for the change in the square of the relative velocity. Therefore, it is assumed that the modified Eötvös number is proportional to the square of the nucleus Reynolds number, $\mathrm{Eo}' \propto \mathrm{Re}_p^2$.

The (relative) acceleration of a gas nucleus can make a nucleus deform. As a nucleus accelerates it will generally stretch, if a nucleus decelerates it will contract. The effect of acceleration can be seen in [21]. Nuclei will accelerate or decelerate in particular when the pressure gradient is large, therefore it is assumed that the modified Eötvös number is also a quantitative measure for the deformation caused by acceleration. Note that the following only holds when the external pressure is held constant.

Concluding, the shape of a gas nucleus can not be predicted as too many factors influence the deformation of a nucleus. The modified Eötvös number however can give a qualitative prediction of the error made due to the deformation of the nucleus (large modified Eötvös number means large deformations).
As far as the drag relation concerned the nucleus is assumed to be spherical along its complete trajectory, there will be no correction on the sphericity. This is in accordance with the assumptions made to derive the gas nucleus dynamics equation.

6.3.2 Interface interactions

Interface interactions between a solid nucleus and the flow are taken into account in the drag relation (see Eq. 6.15).

Gas nuclei can be categorized as clean or contaminated nuclei.
An example of a clean gas nucleus is an air bubble in ultra pure water. Clean nuclei have a mobile interface, as the liquid is free to slip along the interface as the gas will not resist this slip. The mobility of the interface is crucial in the drag relation as a mobile interface prevents the no-slip boundary condition to be enforced. If the liquid can flow undisturbed along an interface there will be no build up of a boundary layer, which decreases the drag significantly. The remaining drag is due to the pressure difference and is approximately $\frac{2}{3}$ of the drag of a solid sphere. Drag relations for both non-deforming gas nuclei and deforming gas nuclei can be found in Eq. 6.13 and Eq. 6.14 respectively.

A contaminated nucleus will have a less mobile or immobile interface. Surfactants are particularly viable to cause interface immobility, even in very low concentrations. The surfactants will build up in the interface and will be transported initially along the interface to the rear of the nucleus. At the location where the concentration of the surfactant is high, the surface tension is lower. The liquid at the boundary is pulled towards the higher surface tension regions. This flow is counteracted by the movement of the nucleus, and will eventually if the water is sufficiently contaminated reach an equilibrium at which the boundary of the nucleus is immobile. The described effect is a consequence of the Marangoni effect ([18],[20],[22]), see Figure 6.2. The immobility of the interface leads to the build up of a boundary layer just as it would with a solid sphere. The drag force for a contaminated spherical gas nucleus will thus be close to that of a solid sphere.

The presence of surfactants at the interface of a nucleus will influence the (local) surface tension of the nucleus, this effect is however not taken into account.

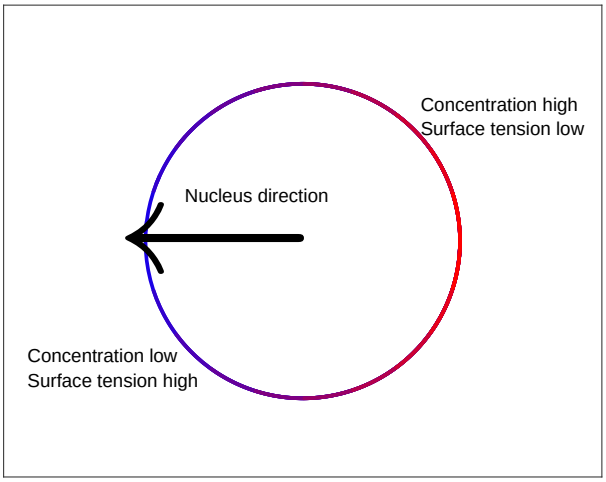

Figure 6.2: Visual interpretation of the Marangoni effect for a moving nucleus.

It will be assumed that the nuclei will be contaminated as the tests will not be conducted in ultra pure liquids, furthermore in real applications like the propeller of a ship the nuclei will surely be contaminated.
If nuclei grow fast the surface concentration of surfactants can be temporarily lower. This effect will also not be taken into account.

6.3.3 Nucleus Reynolds number

The dependency of the drag force on the Reynolds number of the object is well known. The drag coefficient for an uncontaminated non deforming gas nucleus is given in Eq. 6.13.

$$C_D = \frac{16}{\mathrm{Re}_p}\left(1 + \frac{2}{1 + \frac{16}{\mathrm{Re}_p} + \frac{3.315}{\sqrt{\mathrm{Re}_p}}}\right) \tag{6.13}$$

The drag coefficient for an uncontaminated deforming nucleus (due to gravity) can be found in Eq. 6.14 ([19]).

$$C_D = \sqrt{\left\{\frac{16}{\mathrm{Re}_p}\left(1+\frac{2}{1+\frac{16}{\mathrm{Re}_p}+\frac{3.315}{\sqrt{\mathrm{Re}_p}}}\right)\right\}^2+\left\{\frac{3\mathrm{Eo}}{\mathrm{Eo}+9.5}\right\}^2} \tag{6.14}$$

If the Eötvös number is taken as $\mathrm{Eo} = 5\cdot 10^{-6}\mathrm{Re}_p^2$ a good comparison with [23] is found.

The drag coefficient for a solid sphere is given in Eq. 6.15 (by Langmuir and Blodgett).

$$C_D = \frac{24}{\mathrm{Re}_p}\left(1+0.197\mathrm{Re}_p^{0.63}+2.6\cdot 10^{-4}\mathrm{Re}_p^{1.38}\right) \tag{6.15}$$

Improved versions of Eq. 6.15 are widely available, however the same drag relation will be used as in the previous chapter.

The different drag relations are shown in Figure 6.3.

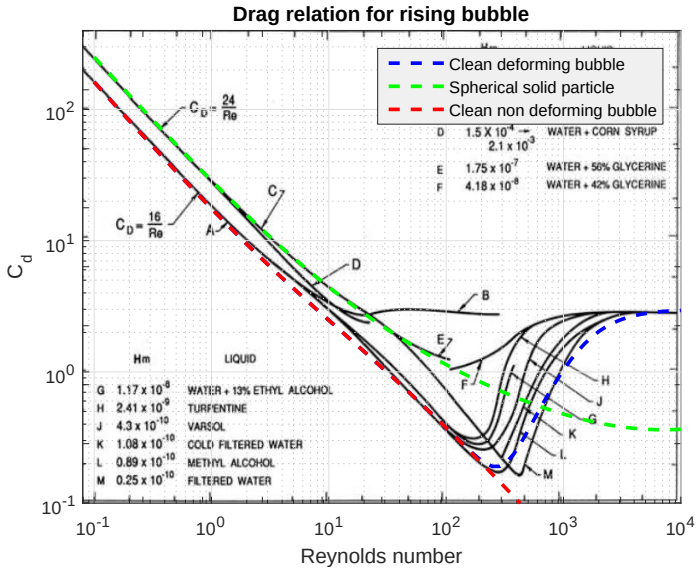

Figure 6.3: red line Eq. 6.13, blue line Eq. 6.14 with $\mathrm{Eo} = 5\cdot 10^{-6}\mathrm{Re}_p^2$, green line Eq. 6.15. Background taken from [23] chapter 5.

As stated before the nuclei are assumed to remain spherical, as the shape of the nuclei is hard to predict and will in general not reach a quasi-steady state. In Eq. 6.14 the nuclei will deform towards spherical caps at their terminal velocities, and is therefore surely not suitable. A spherical nucleus drag relation (Eq. 6.13) neglects the build up of a boundary layer and is therefore not relevant. The more contaminated the liquid the more the nuclei will start to behave like solid particles drag wise. And thus, the spherical solid particle drag relation is used for the calculations. As the modified Eötvös number is large (and thus the nucleus Reynolds number) the drag relation will no longer properly describe the drag force.

A last note on the drag relation is that preferably the drag factor ($\frac{C_D\mathrm{Re}_p}{24}$) should not be singular when it is differentiated with respect to the nucleus Reynolds number and then $\mathrm{Re}_p = 0$ is filled in, as this could lead to singularities in more involved history force terms. For this report this has not led to problems, however this needs to be kept in mind for possible future research.

6.4 Pressure force

The pressure force is the force due to the pressure gradient. The pressure gradient is a body force working on the volume of the nucleus. The pressure force is given in Eq. 6.16.

$$\mathbf{F}_p = -\frac{4}{3}\pi R^3 \nabla p \tag{6.16}$$

The pressure gradient in potential flow and whilst neglecting the gravitational acceleration is given as $\nabla p = -\rho_f \frac{D\mathbf{w}}{Dt}$. There is some discussion [24] on using the material derivative for the pressure gradient and if it should be used in Eq. 6.5. The usual convention is to take the first term on the right-hand side in Eq. 6.7 and add it to the pressure force, meaning that the material derivative will be used. Physically this makes sense as the pressure force works on the nucleus and its added mass. The resulting pressure force corresponds to most force balance based equations of motion, and is given in Eq. 6.17. Note that the pressure gradient force is thus partly due to the Kelvin impulse.

$$\mathbf{F}_p = -\left(1 + C_{am}\right)\frac{4}{3}\pi R^3 \nabla p \tag{6.17}$$

6.5 Gravity

The force due to gravity is given in Eq. 6.18.

$$\mathbf{F}_g = \frac{4}{3}\pi R_0^3 \mathbf{g}(\rho_p - \rho_f) \tag{6.18}$$

The mass of the nucleus is constant, thus the gravitational force is constant. $\mathbf{g}$ is a vector which operates in the vertical direction with components $\mathbf{g} = \begin{bmatrix} 0 \\ -9.81 \end{bmatrix}$ if a standard Cartesian coordinate system is used.

6.6 History force

The history force is a consequence of the lagging build up of both the boundary layer and the wake of the nucleus. The history force can therefore be best understood as the non quasi-steady drag force, thus as the unsteady part of the drag force.
The history force is assumed to be negligible in many gas nucleus motion related studies ([13],[14],[17],[25],[26]), however as the nuclei involved will be contaminated with surfactants, and thus builds up a boundary layer and wake neglecting the history force is not an option. If a boundary layer builds up, the history force might be neglected when the relative acceleration will be sufficiently small, this will in this pressure gradient driven equation of motion not be the case.

The history force for the Stokes limit is given by the Basset force, see Eq. 6.19.

$$\mathbf{F}_{Bas} = -6\pi R(t)\mu_f \int_{-\infty}^{t} K_{Bas}(t,\tau)\frac{d\bar{\mathbf{w}}}{d\tau}d\tau \quad \text{Where:} \quad K_{Bas}(t,\tau) = \frac{1}{\sqrt{4\pi}}\frac{1}{\sqrt{T_H(t,\tau)}} \tag{6.19}$$

The relative velocity, $\bar{\mathbf{w}}$ is defined in Eq. 6.20.

$$\bar{\mathbf{w}}(t) \equiv \mathbf{w}_p(t) - \mathbf{w}(\mathbf{x}_p(t), t) \tag{6.20}$$

The temporal derivative of the relative velocity is given in Eq. 6.21, the gradient in either $\mathbf{x}$ or $\mathbf{x}_p$ might be interchanged as the coordinate system is the same.

$$\frac{d\bar{\mathbf{w}}}{dt} = \frac{d\mathbf{w}_p}{dt} - \left(\mathbf{w}_p \cdot \nabla \mathbf{w} + \frac{\partial \mathbf{w}}{\partial t} \right) \tag{6.21}$$

For steady flow fields the $\frac{\partial \mathbf{w}}{\partial t}$ will cancel. Note that $\mathbf{w}_p \cdot \nabla \mathbf{w} + \frac{\partial \mathbf{w}}{\partial t}$ is *not* the total derivative.

The Basset history force is only valid for low nuclei Reynolds numbers. For Stokes flow the kernel of the history force decays with the square root of the history time. The history time for the Basset kernel is defined as $T_H = \frac{t-\tau}{\tau_d}$, where $\tau_d = \frac{4R^2}{\nu_f}$. τ_d is the diffusive timescale of the nucleus. The general form of the history force can be recognized by the Basset history force, see Eq. 6.22.

$$\mathbf{F}_H = -6\pi R(t)\mu_f \int_{-\infty}^{t} K(t,\tau) \frac{d\bar{\mathbf{w}}}{d\tau} d\tau \tag{6.22}$$

The factor prior to the integral can be recognized as Stokes drag per unit velocity, thus the integral can be interpreted as a correction of the velocity used in the drag relation. In [28] it is shown that the history force can be modeled as a fraction of the drag force (under specific conditions), strengthening the idea of a velocity correction.

For a wider range of nucleus Reynolds numbers, history forces that model the physics more accurate are available ([27],[28]). The forces differ in their respective kernel, $K(t,\tau)$. In general, a history force kernel can be described as in Eq. 6.23.

$$K(t,\tau) = \frac{a(t,\tau)}{\left\{ b(t,\tau) \left[T_H(t,\tau) \right]^{\frac{1}{4}} + c(t,\tau) T_H(t,\tau) \right\}^2} \tag{6.23}$$

In Eq. 6.23 $a(t,\tau)$, $b(t,\tau)$, $c(t,\tau)$ are kernel dependent factors. The history time is $T_H(t,\tau)$, it can be seen that for small history times (assuming $b(t,\tau)$and $c(t,\tau)$ are of the same order) the history kernel decays with the square root of the history time. For larger history times the history kernel decays quadratically with the history time. In other words, the near past has a more significant influence than the far past. The factors $b(t,\tau)$ and $c(t,\tau)$ should be tuned such that the history kernel describes the decay of the relevance of the prior relative acceleration correctly.
For the Basset kernel the kernel dependent factors are: $a(t,\tau) = \frac{1}{\sqrt{4\pi}}$, $b(t,\tau) = 1$ and $c(t,\tau) = 0$. There is thus no distinction between far past and near past in the Basset history force, this can either lead to an overestimation (most cases) or an underestimation (special cases with high relative Reynolds numbers [29], due to $a(t,\tau)$, $b(t,\tau)$ and $c(t,\tau)$) of the actual history force.

Other history forces have been proposed, a fairly complete summary of the proposed history kernels can be found in [27] along with an updated history kernel. In [28] the kernel found in [27] is updated once more and can be found in Eqs. 6.24-6.28. This kernel will be

mentioned as it would be the most complete kernel to implement, it has however not been implemented.

$$K(t,\tau) = \frac{4}{\pi} \frac{f_H(t,\tau)}{\left[[g(t,\tau)T_H(t,\tau)]^{\frac{1}{4}} + \mathrm{Re}_p(t)T_H(t,\tau) \right]^2} \tag{6.24}$$

The history factor f_H is defined as in Eq. 6.25, $f_D(t) = \frac{C_D \mathrm{Re}_p}{24}$ is the drag factor.

$$f_H(t,\tau) = \frac{3}{4}\pi[f_D(t) + \mathrm{Re}_p(t)f'_D(t)]f'_D(\tau) \tag{6.25}$$

The factor $g(t,\tau)$ is determined such that it retains the basset kernel in the Stokes' limit and that it matches the experimental data.

$$g(t,\tau) = 36\pi(f'_D(\tau))^2 \left\{ 1 + \left[\frac{h(\tau)[\mathrm{Re}_p(\tau)]^2}{\mathrm{Re}_p(t)T_H(t,\tau)} \int_\tau^t \frac{d\mathrm{Re}_p f_D}{ds} ds \right]^2 \right\} \tag{6.26}$$

Where $h(\tau)$ is defined as:

$$h(\tau) = \left[1 - \mathrm{e}^{-(0.03\mathrm{Re}(\tau))^2} \right] \left\{ \mathrm{Re}_p(\tau) \left(\frac{11.5 f'_D(\tau)}{f_D(\tau)} \right)^6 + \frac{(f'_D(\tau))^6}{4} \right\} \tag{6.27}$$

The history time $T_H(t,\tau)$ is given in Eq. 6.28 and yields the Basset history time for $\tau \to t$.

$$T_H(t,\tau) = \frac{1}{\tau_d} \int_\tau^t \frac{\mathrm{Re}_p(s)}{\mathrm{Re}_p(t)} ds \tag{6.28}$$

Finally the drag factor, f_D, and the derivative of the dragfactor with respect to the Reynolds number, f'_D, are needed.
From Eq. 6.24 the structure presented in Eq. 6.23 can clearly be seen, $a(t,\tau) = \frac{4}{\pi} f_H(t,\tau)$, $b(t,\tau) = [g(t,\tau)]^{\frac{1}{4}}$ and $c(t,\tau) = \mathrm{Re}_p(t)$.

The complete history kernel shows that the drag factor and its dependency on the nucleus Reynolds number is important. A history force which is based on the drag factor can incorporate the effects which can be incorporated in the drag force. Thus if the shape of a nucleus depends on the Reynolds number and can therefore be captured in the drag relation, the history force can incorporate this dependency. The shape incorporation in the drag relation can not be done in this case as discussed previously.
The history time, $T_H(t,\tau)$, is based on the prior nucleus Reynolds numbers and can only increase as the Reynolds number is always positive.

The experiments on which the kernel is based are experiments of settling spheres in a liquid. The decay of the history force is therefore based on a uni-directional approach. When the nucleus would change direction the build up of the boundary layer differs from the case of uni-directional accelerating nucleus. And the decay of the history force might be different from what is expected.

As the implementation of the kernel presented in Eqs. 6.24-6.28 is labour intensive and

can not assure more accurate results, as the underlying assumptions of spherical gas nuclei and the drag relation of a solid sphere are by far not as accurate as the description of the history kernel, the kernel presented in Eqs. 6.24-6.28 will not be implemented.
To estimate the contribution of the history force the kernel presented by Mei et al. in [27] will be used. This kernel differentiates between long and short history times and can therefore be used to roughly estimate the impact of the actual history force. The kernel can be found in Eq. 6.29.

$$K(t,\tau) = \frac{K_{Bas}(t,\tau)}{\left\{1 + \left[\frac{1}{4^2\pi}\left(\frac{\mathrm{Re}_p(t)}{K_{Bas}(t,\tau)}\right)^3 \frac{1}{f_H}\right]^{\frac{1}{c_1}}\right\}^{c_1}} \quad \text{Where:} \quad f_H = \left(0.75 + c_2\mathrm{Re}_p(t)\right)^3 \tag{6.29}$$

The Basset kernel, $K_{Bas}(t,\tau)$, is given in Eq. 6.19. The factors c_1 and c_2 are found by Mei et al on a semi-analytical basis as: $c_1 = 2$ and $c_2 = 0.2$. When $c_1 = 2$ is taken the structure given in Eq. 6.23 can be recognized. To fit the experiments better the coefficients c_1 and c_2 have been found to be $c_1 = 2.5$ and $c_2 = 0.105$ by Loth and Dorgan. The latter will be used to estimate the history force. The implementation will be relatively simple and due to the decay the kernel will not over predict the history force systematically.

6.7 Total equation of motion

The equation of motion can be found by summing all forces, see Eq. 6.30.

$$\mathbf{F}_m = \sum \mathbf{F}_{\text{on nucleus}} = \mathbf{F}_I + \mathbf{F}_D + \mathbf{F}_p + \mathbf{F}_g + \mathbf{F}_H \tag{6.30}$$

The forces taken into account are described and lead to Eq. 6.31.

$$\begin{aligned}\rho_p \frac{4}{3}\pi R_0^3 \frac{d\mathbf{w}_p}{dt} =& - C_{am}\rho_f \frac{4}{3}\pi R^3 \frac{d\mathbf{w}_p}{dt} + C_{am}\rho_f 4\pi R^2 \frac{dR}{dt}(\mathbf{w} - \mathbf{w}_p) \\ &+ \frac{1}{2}\rho_f C_D \pi R^2 (\mathbf{w} - \mathbf{w}_p)|\mathbf{w} - \mathbf{w}_p| - (1 + C_{am})\frac{4}{3}\pi R^3 \nabla p \\ &+ \frac{4}{3}\pi R_0^3 \mathbf{g}(\rho_p - \rho_f) - 6\pi R \mu_f \int_{-\infty}^{t} K(t,\tau)\frac{d\bar{\mathbf{w}}}{d\tau} d\tau\end{aligned} \tag{6.31}$$

Rewriting Eq. 6.31 gives Eq. 6.32, in which an equation of motion can be recognized.

$$\begin{aligned}\frac{d\mathbf{w}_p}{dt} =& \frac{1}{\rho_p \frac{4}{3}\pi R_0^3 + C_{am}\rho_f \frac{4}{3}\pi R^3}\Big\{ C_{am}\rho_f 4\pi R^2 \frac{dR}{dt}(\mathbf{w} - \mathbf{w}_p) \\ &+ \frac{1}{2}\rho_f C_D \pi R^2 (\mathbf{w} - \mathbf{w}_p)|\mathbf{w} - \mathbf{w}_p| - (1 + C_{am})\frac{4}{3}\pi R^3 \nabla p \\ &+ \frac{4}{3}\pi R_0^3 \mathbf{g}(\rho_p - \rho_f) - 6\pi R \mu_f \int_{-\infty}^{t} K(t,\tau)\frac{d\bar{\mathbf{w}}}{d\tau} d\tau \Big\}\end{aligned} \tag{6.32}$$

The upper boundary of the history integral requires $\frac{d\mathbf{w}_p}{dt}$, in Chapter 8 it will be discussed how this is circumvented

7 Impact Model

7.1 Gas nucleus

An impact model for a gas nucleus will be included in the equation of motion. In the literature impact models regarding gas nuclei rising under gravity against a flat plate have been developed ([12],[30]). These models are based on the film drainage of the film between the plate and the nucleus. The film drainage force is a repulsive force since the pressure in the film increases. The result of this force is the bounce of the nucleus. The results found in [12] can be seen in Figure 7.1.

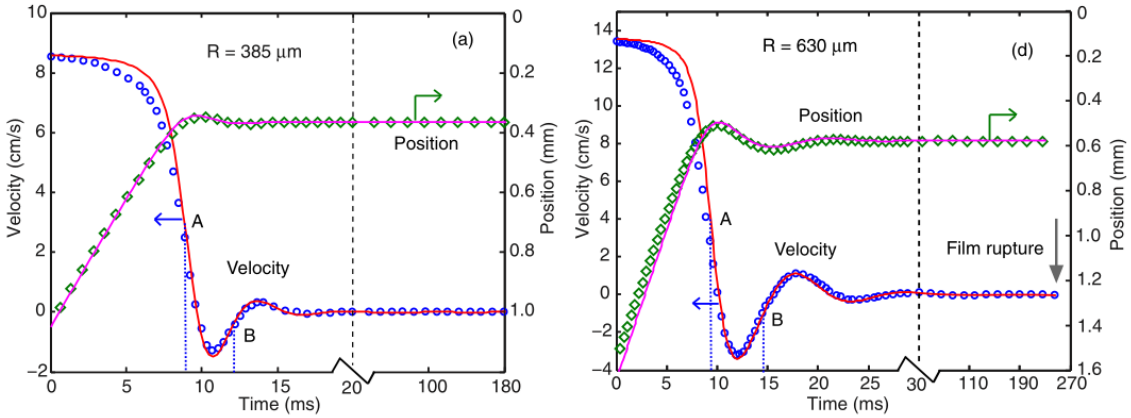

Figure 7.1: Result of the impact model by [12].

In Figure 7.1, the position of the nucleus as a function of time can be seen on the right axis. The nucleus hardly bounces, as the distance from the middle of the nucleus to the plate changes far less than the radius of the nucleus. Furthermore the small bounce damps out fast.

The film drainage on which the repulsive force of the impact model is based will not be included as the film between an object and a nucleus in a non-quiescent flow field will consist of the boundary layer of the object. The effects of viscous and turbulent flow features are left out of consideration. Near boundary layers the lift force would possibly be a more relevant repulsive force than the film drainage force.

Using a normal force in the impact model is an option, however as the nucleus hits the body the definition of the normal force is undefined. This could be circumvented using a force during the time step prior to the moment of impact. In practice, this would mean that once the impact is registered the equation of motion during the prior time step will be adjusted so that in that time step the nucleus will stop moving in the normal direction to the body. Implementing an impact model based on a normal force benefits from the fact that the normal equation of motion can hold along the body surface. The implementation of this impact model is however impractical and will need control over the time step prior to the impact. Furthermore, the impact model will usually be relevant past the point of cavitation inception, so past the most interesting point for this research. And finally, gas nuclei will

deform under the force during impact which can not be taken into account.
Implementing an impact model based on the normal force will be labor intensive and can not guarantee better results.

The impact model of choice is based on the observation that the nucleus hardly bounces (see Figure 7.1). It is assumed that once the nucleus hits the body the nucleus follows the streamline of its middle point. This is as long as the nucleus does not change size. When the nucleus has hit the body and grows the velocity of the nucleus will be that of the streamline of the center together with the normal velocity following from the growth of the nucleus. When the nucleus shrinks the nucleus will get back in the flow and therefore the normal equation of motion holds again.
Clearly, this impact model violates the equation of motion when the nucleus grows along the surface. The equation of motion will in practice however be ”checked” regularly since the nucleus will normally move towards the high-pressure region near the stagnation point of the trailing edge. The presented impact model is easy to implement as the velocity of the streamline is known and the growth of the nucleus is calculated anyway using a gas nucleus dynamics equation.

7.2 Solid

For a solid particle the same impact model as that for a gas nucleus is implemented. Since a solid particle will not change size the solid particle will follow the streamline once it has hit the body.

If the impact of a solid particle would have been implemented more precisely using the coefficient of restitution the result would not have been better for sure as the effects of the shape and the boundary layer are omitted anyway.

8 Solving procedure

Eq. 5.2 and Eq. 6.32 form the set of non linear coupled second order differential equations which needs to be solved. Within this set of equations the impact model will be implemented.

8.1 History force

To solve the equations of motion, dealing with the history force is important. The integral given in Eq. 6.22 is repeated in Eq. 8.1.

$$-\frac{\mathbf{F}_H}{6\pi R(t)\mu_f} = \int_{-\infty}^{t} K(t,\tau)\frac{d\bar{\mathbf{w}}}{d\tau}d\tau \tag{8.1}$$

The lower boundary of the integral shows the need for the total history of the nucleus. To circumvent needing the total history, the integral can be splitted as in Eq. 8.2.

$$\int_{-\infty}^{t} K(t,\tau)\frac{d\bar{\mathbf{w}}}{d\tau}d\tau = \int_{-\infty}^{t_0} K(t,\tau)\frac{d\bar{\mathbf{w}}}{d\tau}d\tau + \int_{t_0}^{t} K(t,\tau)\frac{d\bar{\mathbf{w}}}{d\tau}d\tau \tag{8.2}$$

Where t_0 is the initial time. Assuming that prior to t_0 no relative acceleration has taken place yields no contribution of the first term on the right hand side of Eq. 8.2. This imposes a restrain on the initial conditions. The initial velocity must be equal to the flow velocity at the initial location, $\mathbf{w}_p(t_0) = \mathbf{w}(\mathbf{x}_p(t_0), t_0)$.

The upper boundary of the integral leads to a history time of $T_H = 0$, as can be seen by the general form of the history kernel, Eq. 6.23. This leads to singularities. Furthermore, filling in the upper boundary of the integral requires the current relative acceleration. To circumvent both problems the remaining integral will be split once more, see Eq. 8.3.

$$\int_{t_0}^{t} K(t,\tau)\frac{d\bar{\mathbf{w}}}{d\tau}d\tau = \int_{t_0}^{t-\Delta t_n} K(t,\tau)\frac{d\bar{\mathbf{w}}}{d\tau}d\tau + \int_{t-\Delta t_n}^{t} K(t,\tau)\frac{d\bar{\mathbf{w}}}{d\tau}d\tau \tag{8.3}$$

Δt_n is the n^{th} time step. The second part on the right hand side of Eq. 8.3 will be approximated. First, the relative acceleration over the last time step will be assumed to be constant (so the time step may not be too large) and equal to the relative acceleration at the previous time step. Secondly, the Kernel, $K(t,\tau)$, will be approximated by the Basset kernel (Eq. 6.19), for the short history times evaluated (due to the small time step) this approximation is accurate. This results in Eq. 8.4.

$$\int_{t_0}^{t} K(t,\tau)\frac{d\bar{\mathbf{w}}}{d\tau}d\tau \approx \int_{t_0}^{t-\Delta t_n} K(t,\tau)\frac{d\bar{\mathbf{w}}}{d\tau}d\tau + \frac{d\bar{\mathbf{w}}}{dt}|_{t-\Delta t_n}\int_{t-\Delta t_n}^{t} K_{Bas}(t,\tau)d\tau \tag{8.4}$$

The Basset kernel can be integrated analytically leading to Eq. 8.5.

$$\int_{t_0}^{t} K(t,\tau)\frac{d\bar{\mathbf{w}}}{d\tau}d\tau \approx \int_{t_0}^{t-\Delta t_n} K(t,\tau)\frac{d\bar{\mathbf{w}}}{d\tau}d\tau + \frac{d\bar{\mathbf{w}}}{d\tau}|_{t-\Delta t_n}\sqrt{\frac{\tau_d \Delta t_n}{\pi}} \tag{8.5}$$

The history kernel described by Eqs. 6.24-6.28 approaches the Basset history kernel in the limit of short history times, making the derived approximation exact in the limit for a time step going to zero. For the used history kernel, (Eq. 6.29) this is however not the case.

The remaining integral will be approximated numerically using the trapezoidal rule, which is second order for multiple time steps. The integral needs to be calculated every time step since the kernel depends on time.

8.2 Order reduction

The total set of equations can be written in short as Eq. 8.6.

$$\frac{d}{dt}\begin{bmatrix} u_p \\ v_p \\ \frac{dR}{dt} \end{bmatrix} = \begin{bmatrix} f_1(\frac{dR}{dt}, R, \mathbf{w}_p, \mathbf{x}_p, t) \\ f_2(\frac{dR}{dt}, R, \mathbf{w}_p, \mathbf{x}_p, t) \\ f_3(\frac{dR}{dt}, R, \mathbf{x}_p, t) \end{bmatrix} \tag{8.6}$$

The functions f_1, f_2 and f_3 are determined by Eq. 6.32 (f_1 and f_2) in combination with the approximate history force of Eq. 8.5 and Eq. 5.2 (f_3). To solve the second order non-linear differential equations, order reduction will be used, see Eq. 8.7. For the full set of equations, see Appendix G.

$$\frac{d}{dt}\begin{bmatrix} x_p \\ u_p \\ y_p \\ v_p \\ R \\ \frac{dR}{dt} \end{bmatrix} = \begin{bmatrix} u_p(t) \\ f_1(\frac{dR}{dt}, R, \mathbf{w}_p, \mathbf{x}_p, t) \\ v_p(t) \\ f_2(\frac{dR}{dt}, R, \mathbf{w}_p, \mathbf{x}_p, t) \\ \frac{dR}{dt} \\ f_3(\frac{dR}{dt}, R, \mathbf{x}_p, t) \end{bmatrix} \tag{8.7}$$

In short, Eq. 8.7 can be written as Eq. 8.8, it can be seen that Eq. 8.8 is a first order non linear differential equation.

$$\frac{d\mathbf{Q}}{dt} = f(\mathbf{Q}, t) \quad \text{Where} \quad \mathbf{Q} = \begin{bmatrix} x_p & u_p & y_p & v_p & R & \frac{dR}{dt} \end{bmatrix}^T \tag{8.8}$$

8.3 Impact model

An impact model needs to detect contact. When the normal distance from the body to the middle of the nucleus is smaller than or equal to the radius of the nucleus, the nucleus and the body are in contact. The condition is given in Eq. 8.9. The normal distance, D_n, is used as the profile is smooth.

$$D_n \leq R(t) \tag{8.9}$$

The impact model as described in Chapter 7 couples the movement of the nucleus to the properties of the streamline at the middle of the nucleus and to the growth of the nucleus. The velocity of the nucleus is described by Eq. 8.10.

$$\mathbf{w}_p = \underbrace{\mathbf{w}(\mathbf{x}_p)}_{\text{Streamline}} + \underbrace{\hat{\mathbf{n}}(\mathbf{x}_p, R)\frac{dR}{dt}}_{\text{Growth}} \tag{8.10}$$

In Eq. 8.10 $\hat{\mathbf{n}}(\mathbf{x}_p, R)$ is the outward unit normal of the body at the location the nucleus hits the body. The location where the nucleus hits the body is determined by the location of the center of the nucleus and its radius. Assuming that the change in the normal of the body is small within one time step leads to a nucleus acceleration given in Eq. 8.11.

$$\frac{d\mathbf{w}_p}{dt} \approx \mathbf{w}_p \cdot \nabla\mathbf{w}(\mathbf{x}_p) + \hat{\mathbf{n}}(\mathbf{x}_p, R)\frac{d^2R}{dt^2} \tag{8.11}$$

Apart from the trailing edge, the normal will change smoothly. Nuclei will not remain in contact with the body over the trailing edge.
The set of equations being solved when the impact model is used is given in Appendix G, and can be summarized by Eq. 8.12. The approximate acceleration of the nucleus (Eq. 8.11) is not necessary to calculate the trajectory but will be used to estimate the history force while the nucleus was in contact with the body.

$$\frac{d}{dt}\begin{bmatrix} x_p \\ u_p \\ y_p \\ v_p \\ R \\ \frac{dR}{dt} \end{bmatrix} = \begin{bmatrix} f_1(\frac{dR}{dt}, R, \mathbf{x}_p, t) \\ f_2(\frac{d^2R}{dt^2}, R, \mathbf{w}_p, \mathbf{x}_p, t) \\ f_3(\frac{dR}{dt}, R, \mathbf{x}_p, t) \\ f_4(\frac{d^2R}{dt^2}, R, \mathbf{w}_p, \mathbf{x}_p, t) \\ \frac{dR}{dt} \\ f_5(\frac{dR}{dt}, R, \mathbf{x}_p, t) \end{bmatrix} \tag{8.12}$$

In Eq. 8.12 f_1 and f_3 are determined by Eq. 8.10, f_2 and f_4 are determined by Eq. 8.11, and finally f_5 is still determined by Eq. 5.2. The presented order is not the order used to solve the set of equations, as the nucleus growth needs to be calculated first.

8.4 Integration method

The first order non linear set of ordinary differential equations will be solved using the standard fourth order accurate Runge-Kutta method. This method is presented in Eq. 8.13, using the conventions of Eq. 8.8.

$$\begin{aligned} \mathbf{Q}_{n+1} =& \mathbf{Q}_n + \frac{\Delta t_n}{6}\left(\mathbf{k}_1 + 2\mathbf{k}_2 + 2\mathbf{k}_3 + \mathbf{k}_4\right) \quad \text{Where} \\ \mathbf{k}_1 =& f(t_n, \mathbf{Q}_n) \\ \mathbf{k}_2 =& f(t_n + \frac{\Delta t_n}{2}, \mathbf{Q}_n + \Delta t_n \frac{\mathbf{k}_1}{2}) \\ \mathbf{k}_3 =& f(t_n + \frac{\Delta t_n}{2}, \mathbf{Q}_n + \Delta t_n \frac{\mathbf{k}_2}{2}) \\ \mathbf{k}_4 =& f(t_n + \Delta t_n, \mathbf{Q}_n + \Delta t_n \mathbf{k}_3) \end{aligned} \tag{8.13}$$

The time step used for the integration scheme will be variable as to model the nucleus collapse very small time steps are required, which would cost a lot of computational time if the time step is kept constant especially considering the history integral.

The wanted time step can be found if a maximum absolute and/or relative change allowed in the variables is specified. The maximum absolute and relative changes are defined in Eq. 8.14 as Δ_{abs} and Δ_{rel} respectively.

$$\begin{aligned} \Delta_{abs} &= \max |\mathbf{Q}_{n+1} - \mathbf{Q}_n| \\ \Delta_{rel} &= \max \frac{|\mathbf{Q}_{n+1} - \mathbf{Q}_n|}{|\mathbf{Q}_n|} \end{aligned} \tag{8.14}$$

The time step following from this requirement can be approximated as in Eq. 8.15.

$$\left| \frac{d\mathbf{Q}_n}{dt} \right| \approx \frac{|\mathbf{Q}_{n+1} - \mathbf{Q}_n|}{\Delta t_{n+1}} \tag{8.15}$$

The order of approximation of the time step does not influence the order of the integration scheme. The time steps found can be seen in Eq. 8.16.

$$\begin{aligned} \Delta t_{abs} &= \frac{\Delta_{abs}}{\max \left| \frac{d\mathbf{Q}_n}{dt} \right|} \\ \Delta t_{rel} &= \frac{\Delta_{rel} |\mathbf{Q}_{n,max}|}{\max \left| \frac{d\mathbf{Q}_n}{dt} \right|} \end{aligned} \tag{8.16}$$

The time steps found do not guarantee a maximum error, however if it is assumed that the error over one time step is significantly smaller than the change in the solution than the found time step will result in acceptable errors. Under stable conditions, the assumption on the error will hold, especially taking into account the fourth order time integration scheme. Ideally, the time step would be determined using two solutions with different accuracy to estimate the error. The benefit of the proposed method is that the change of the solution can be influenced directly, such that the solution does not change too much with respect to the body size.
The time step used for the integration will be the minimum of the two time steps found in Eq. 8.16, as long as it is in a range defined by a maximum and a minimum time step, Δt_{max} and Δt_{min} respectively. The end result can be seen in Eq. 8.17.

$$\Delta t = \min \left\{ \max \left[\min \left(\Delta t_{abs}, \Delta t_{rel} \right), \Delta t_{min} \right], \Delta t_{max} \right\} \tag{8.17}$$

9 Results

9.1 Profile shape

The resulting trajectories depend on the shape of the profile. The profile shape will therefore first be established. The profile shape used will be that of a section of a propeller blade. The blade can be seen in Figure 9.1, and is the same blade as used in [31]. The half cylinder shows the plane where the cross section of the blade will be taken. The cross section is taken at 60% of the total radius of the propeller blade.

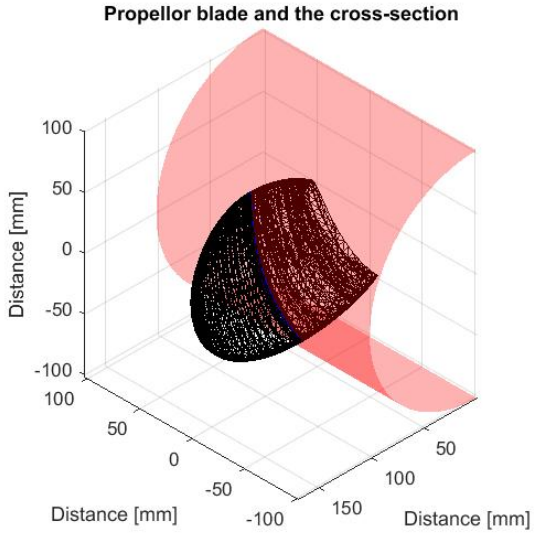

Figure 9.1: The propeller blade and the location of the cross section.

The cross sectional shape can be seen in Figure 9.3.

The flow surrounding a 3D propeller is a rotating flow. This means that from the point of view from the flow the shape of the propeller differs from the actual shape, more specific the camber of the profile and the angle of attack differ. To compensate for this fact, a 3D ProCall calculation of the propeller has been made, to retrieve a pressure distribution at the cross section. The cross section can then be fitted to the pressure distribution, by changing the camber of the profile and the angle of attack of the flow. The pressure distribution of the ProCall calculation and the fitted pressure distribution can be seen in Figure 9.2. The fitted pressure distribution has been checked using XFoil (programm made by MIT), which can also be seen in Figure 9.2. The overlap of the resulting pressure coefficient is most important at the front of the profile, as both the high and the low pressure regions are located there. Both the maximum and the minimum pressure coefficient differ slightly. This is a consequence of the amount of panels used in the ProCall calculations. The fit has thus been made on the resulting shape of the pressure coefficient line and not on the maximum or minimum pressure coefficient. Inviscid XFoil calculations and viscid XFoil calculations hardly differ as the Reynolds number used in the ProCall calculations was high ($\mathrm{Re}_f \approx 8 \cdot 10^7$) and taken as input for the viscid XFoil simulation.

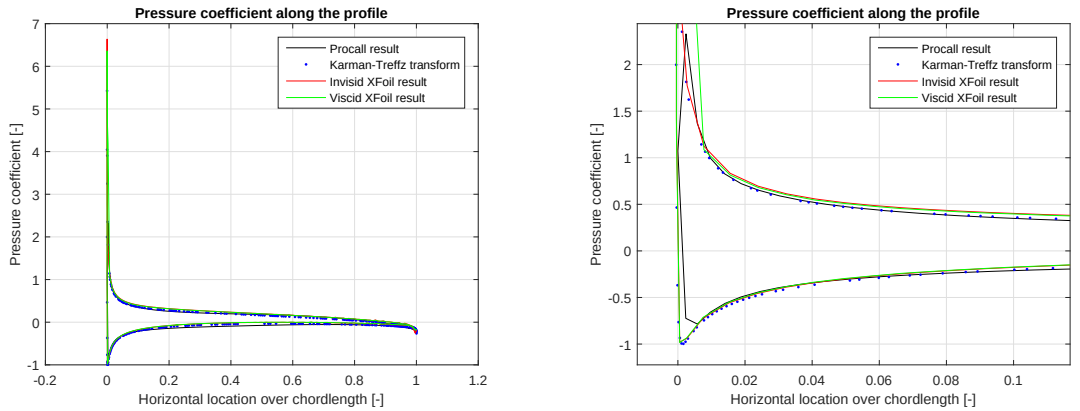

(a) Pressure coefficient.

(b) Zoomed in Pressure coefficient.

Figure 9.2: Fitted pressure coefficient.

The shape of the profile along with the shape experienced by the flow are shown in Figure 9.3.

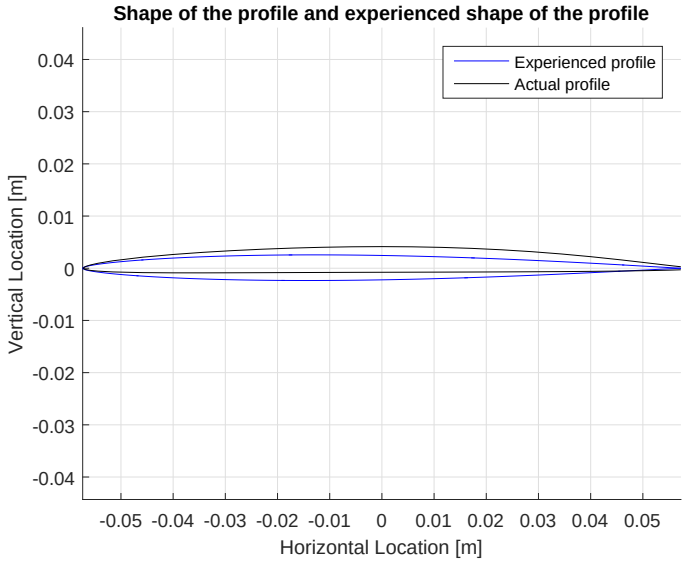

Figure 9.3: The cross section of the blade and the approximate experienced shape of the cross section.

The approximate profile as experienced by the flow will from now on be used for the calculations and is given by $R_{cyl} = 29.14\,mm$, $\frac{\xi_0}{R_{cyl}} = -0.017$, $\frac{\eta_0}{R_{cyl}} = 0.002$, $\alpha_{te} = 5.5°$ and $\alpha = 2.5°$.

9.2 Velocity

The flow velocity around the profile depends on the rotation rate of the propeller, n_{prop} and the local radius of the propeller, r_{prop}, and on the linear velocity of the propeller, V_{lin}.

The approximate undisturbed velocity, U_0, which can be used for the calculations is given in Eq. 9.1.

$$U_0 = \sqrt{V_{lin}^2 + \left(2\pi r_{prop} n_{prop}\right)^2} = 2n_{prop} R_{prop} \sqrt{J^2 + \left(\frac{r_{prop}}{R_{prop}\pi}\right)^2} \tag{9.1}$$

The advance ratio, J, is defined in Eq. 9.2 and R_{prop} is the total radius of the propeller.

$$J = \frac{V_{lin}}{2n_{prop} R_{prop}} \tag{9.2}$$

The found equivalent of the free stream velocity, U_0, will be used to describe the flow around the profile.
The advance ratio remains at $J = 0.4$, the propeller radius is $R_{prop} = 170\,mm$ and $\frac{r_{prop}}{R_{prop}} = 0.6$ the rotational rate will change.

In accordance with [31], the cavitation number and pressure coefficient will be based on the rotational rate of the propeller, and not on the free stream velocity. Both definitions are given in Eq. 9.3.

$$\sigma_{v,n} = \frac{p_0 - p_v}{2\rho_f n_{prop}^2 R_{prop}} \quad C_{p,n} = \frac{p - p_0}{2\rho_f n_{prop}^2 R_{prop}^2} \tag{9.3}$$

The trajectory and radius will be calculated as discussed in Chapter 8, with a flow field given in section 9.1. The result of Eq. 8.12 can be seen in Figure 9.4 as the trajectory with the Loth and Dorgan history kernel.

9.3 Influence of the history force

The influence of the history force on the trajectory can be seen in Figure 9.4. The history force yields trajectories closer to the body. When the history force is overestimated by means of the Basset force the trajectory is closest to the body. The resulting effect of the history force is expected as it counteracts relative accelerations, which occur near the leading edge of the profile. The history force, can for specific cases, be approximated by a fraction of the drag force, the history force will therefore counteract screening.

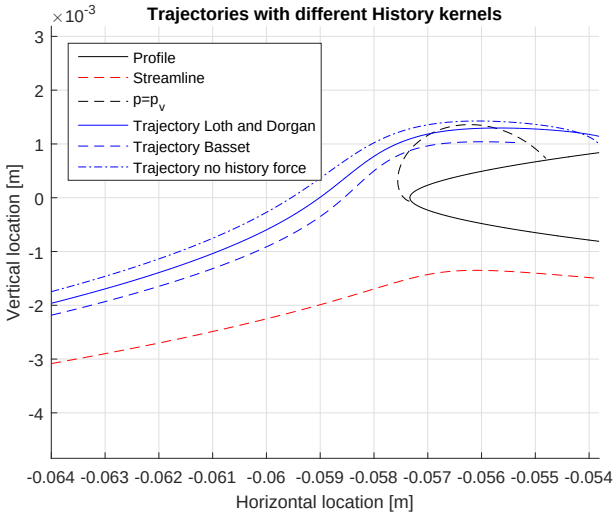

Figure 9.4: Trajectories with different history kernels and the streamline with the same initial condition. $R_0 = 100\,\mu m$, $\sigma_{v,n} = 2.5$ and $n_{prop} = 7\,s^{-1}$.

When the trajectory is altered the growth of the nucleus is influenced. The influence of the history force on the nucleus growth can be seen in Figure 9.5. The history force can make the difference between cavitation ($R > R_{crit}$) and no cavitation ($R < R_{crit}$).

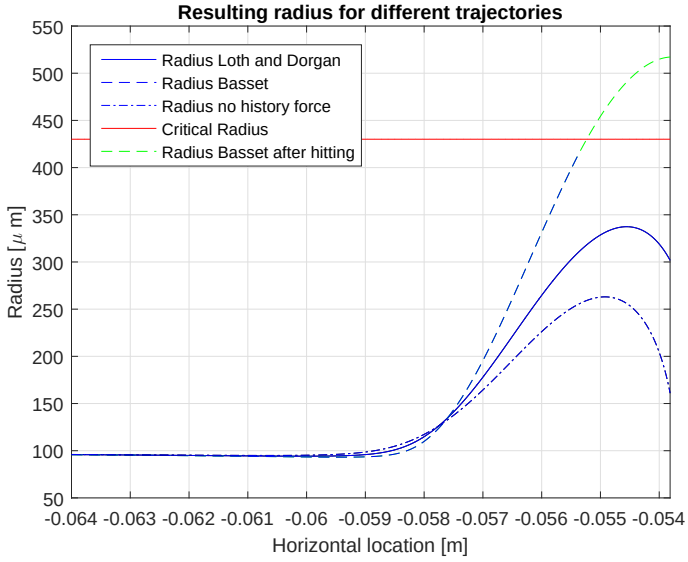

Figure 9.5: Nucleus radius for trajectories with different history kernels. $R_0 = 100\,\mu m$, $\sigma_{v,n} = 2.5$ and $n_{prop} = 7\,s^{-1}$.

The influence of the history force on the force balance can best be shown by a comparison between the drag force and the history force, see Figure 9.6. The drag force and history force are taken from the trajectory with the history force of Loth and Dorgan (Figure 9.4). The history force is of the same order as the drag force (and approximately in the same direction even though this can not be seen in the figure). The influence of the history force can be approximated by increasing the drag force, the approximation however is very rough as both the direction and the magnitude are not scalable by one constant along the trajectory. Furthermore, it might look like the drag force should very roughly be increased by a factor of two to find the same trajectory, this might however in the absence of any history force

not be true. Finding the scaling constant should be done in an iterative process where the results should still be compared to the result found by using the history force.

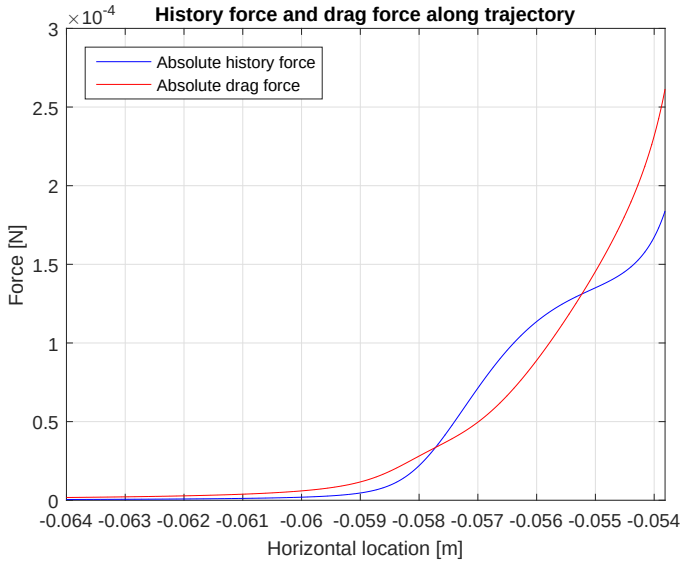

Figure 9.6: The absolute value of the history force by Loth and Dorgan and the drag force. $R_0 = 100\,\mu m$, $\sigma_{v,n} = 2.5$ and $n_{prop} = 7\,s^{-1}$.

9.4 Impact model

The impact model as described in 8.12 keeps the nucleus from getting into the profile, see Figure 9.7. Once the body is hit by the nucleus, the nucleus follows the streamline of the middle point of the nucleus.

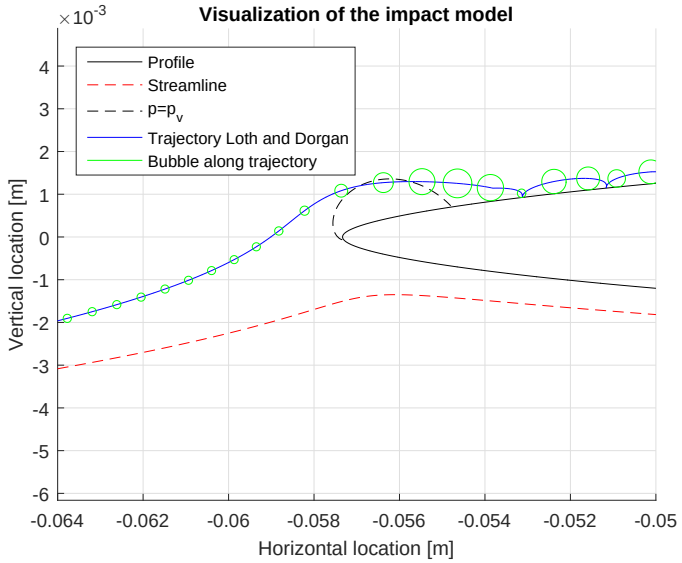

Figure 9.7: The impact model keeping the nucleus from getting into the body. $R_0 = 100\,\mu m$, $\sigma_{v,n} = 2.5$ and $n_{prop} = 7\,s^{-1}$.

9.5 Time step

The integration method depends on the variable time step. The variable time step is shown in Figure 9.8 for the trajectory with the history force of Loth and Dorgan shown in Figure 9.4. The integration method is started using small time steps, the time step will thus initially increase. As the nucleus gets closer to the body more change in the variables is expected, and therefore the time step will decrease. If the calculated time step gets below the minimum time step, the minimum time step will be used.

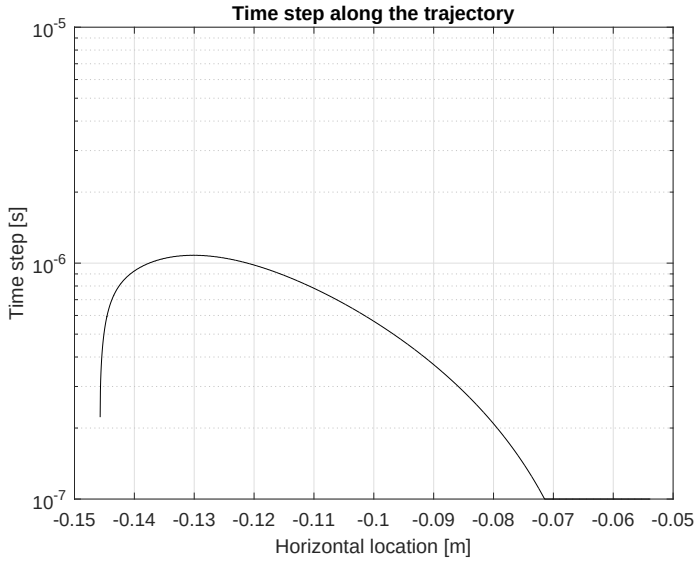

Figure 9.8: The time step along the trajectory, $R_0 = 100\,\mu m$, $\sigma_{v,n} = 2.5$ and $n_{prop} = 7\,s^{-1}$.

9.6 The modified Eötvös number and the nucleus Reynolds number

The modified Eötvös number is a quantitative measure for the deformation of a gas nucleus and proportional to the nucleus Reynolds number squared (Eq. 6.12). In Figure 9.9 the modified Eötvös number for the trajectory with the history force of Loth and Dorgan (Figure 9.4) can be seen. In the same Figure the proportionality to the nucleus Reynolds number has been checked using $\mathrm{Eo}' \approx 200\mathrm{Re}_p^2$.

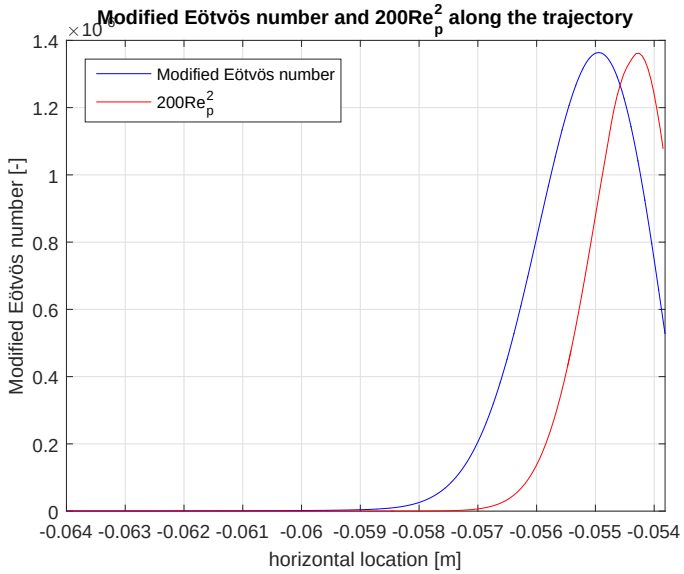

Figure 9.9: The modified Eötvös number and the line 200Re_p^2 along the trajectory. $R_0 = 100\,\mu m$, $\sigma_{v,n} = 2.5$ and $n_{prop} = 7\,s^{-1}$.

The modified Eötvös number reacts prior to the nucleus Reynolds number the reason being that the relative acceleration reacts primarily to pressure gradients and not the relative velocity. The nucleus Reynolds number might be used to qualitatively estimate the deformation of a gas nucleus. The delay should then be taken into account. Estimating if the modified Eötvös number is large should be based on experiments.

9.7 Non-symmetric screening

Screening has been introduced in the first part as the effect that prevents larger gas nuclei to cavitate. The concept of screening will be evaluated for non-symmetric profiles.

The screening effect on a non-symmetric profile seen from the point of view from the flow significantly differs from the screening of symmetric profiles.

For non-symmetric profiles, the screening of a gas nucleus can be either too little, too much or enough. In Figure 9.10 the concept is illustrated.
Too much screening on non-symmetric profiles occurs in a similar fashion to screening on symmetric profiles, too much screening lets the nucleus move over the region where the pressure is below the vapor pressure. Or more precise, over the region where the pressure is low enough for the nucleus to cavitate. Too much screening can occur even when the nucleus starts below the dividing streamline. The high pressure region pushes the nucleus upwards of the dividing streamline. Too much screening is illustrated by the upper nucleus path in Figure 9.10.
Too little screening on non-symmetric profiles occurs when the nucleus starts below the dividing streamline and will not get pushed upwards of the dividing streamline. The nucleus will then get below the profile and thus not encounter low enough pressures. See the lowest nucleus path in Figure 9.10.
Finally, enough screening is introduced as the amount of screening leading to cavitation. See the middle nucleus path in Figure 9.10.

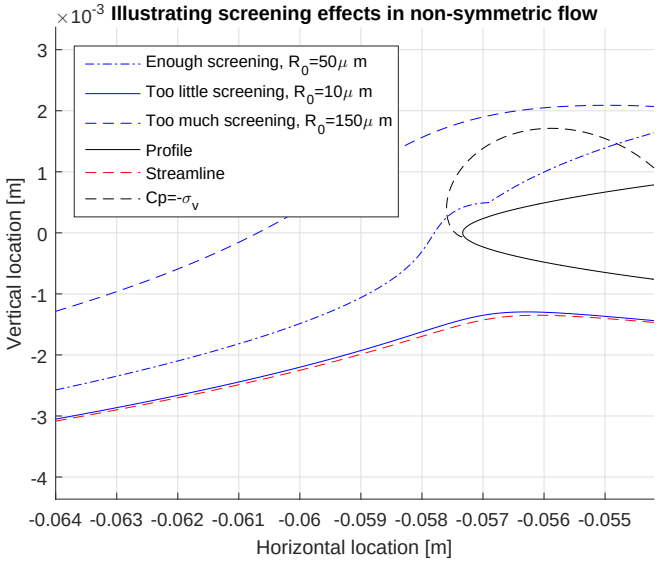

Figure 9.10: Illustration of the concept of too much too little and enough screening. $\sigma_{v,n} = 2.2$ and $n_{prop} = 10\,s^{-1}$.

Figure 9.11 shows the cavitation type for nuclei with different initial radii and different initial heights. The region in which cavitation occurs roughly has a drop like shape. Nuclei larger than cavitating nuclei with the same initial height are nuclei which have been screened too much.
Nuclei smaller than cavitating nuclei with the same initial height and starting below the dividing streamline are screened too little. Nuclei smaller than cavitating nuclei with the same initial height and starting above the dividing streamline remain stable.

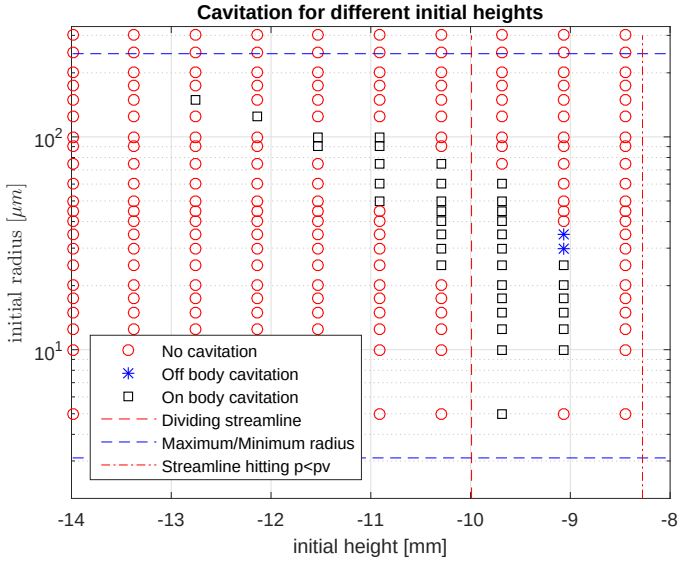

Figure 9.11: The cavitation behavior for a propeller blade section with $\sigma_{v,n} = 2.2$ and $n_{prop} = 10\,s^{-1}$.

Larger nuclei need to start further below the dividing streamline to induce cavitation, which is the most important difference between symmetric screening and non-symmetric screening. If, in the case of a symmetric profile under zero incidence, a nucleus starts above the dividing streamline and is screened too much the same behavior is mirrored below the dividing streamline.

To estimate the bandwidth of initial heights in which nuclei might start, the streamline just hitting the area where the pressure is below the vapor pressure is important. When the high pressure and the low pressure area are sufficiently close the screening effect will push away all nuclei till (just) above the low pressure region. This is the right vertical line in Figure 9.11.
The dividing streamline does not give an estimate of the bandwidth in itself. However, having the streamline hitting the low pressure region, the dividing streamline gives perspective. If there was no screening ($n_{prop} \rightarrow 0$) all cavitation occurrences would occur between both lines. This is the left vertical line in Figure 9.11.
To estimate a lower limit on the available nuclei sizes the stability criteria as given in Eq. 2.5 is used with $C_p^* = C_{p,min}$ the $C_{p,min}$ will not be taken from the calculations but from the experiments done in [31] as $C_{p,n,min} = -5$. The minimum pressure coefficient in the calculations is lower than the minimum pressure coefficient found in experiments. The lower limit can be seen in Figure 9.11 as the lowest horizontal line.
The approximate upper limit on the available nuclei sizes can be determined by neglecting the bubble dynamics. If the nucleus remains spherical and the growth of the nucleus only reacts to the pressure in the middle point of the nucleus, then the critical radius of the nucleus (Eq. 2.4) should be smaller than the maximum distance from the iso-line where the pressure is the vapor pressure and the profile. The approximate upper limit is determined by the assumptions of the current model. The influence of bubble dynamics on the approximate upper limit can either decrease or increase the limit. As the nucleus has a reaction time, the nucleus can either not react in time to the low pressure, or not react in time to high pressures. The approximate upper limit is given in Figure 9.11 as the highest horizontal line.

9.7.1 Lowering the rotational rate

A lower rotational rate leads to less screening, therefore the cavitation region will get more centered around the dividing streamline. The lower limit will increase slightly as nuclei become more stable. The upper limit will increase since, to keep the cavitation number constant, the surrounding pressure has to be increased. The result can be seen in Figure. 9.12.

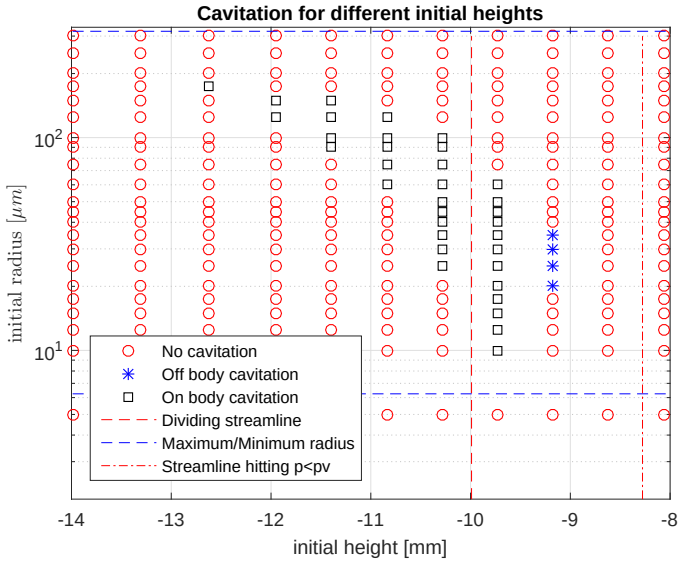

Figure 9.12: The cavitation behavior for a propellor blade section with $\sigma_{v,n} = 2.2$ and $n_{prop} = 7\,s^{-1}$.

In Figure 9.13, the largest and smallest radii available for cavitation are plotted for different rotational rates. The dashed lines are the observed limits, see Figures 9.11 and 9.12, the solid lines are the theoretical maximums and minimums in the absence of dynamical effects. The theoretical limits behave similar to the found limits, the found limits are well within the range of the theoretical limits. The fact that the theoretical upper limits and the found upper limits behave likewise is interesting as it is assumed that the upper limit would (partially) be determined by the screening effect. It seems that the screening effect is not directly affecting the available nuclei spectrum in non-symmetric conditions.

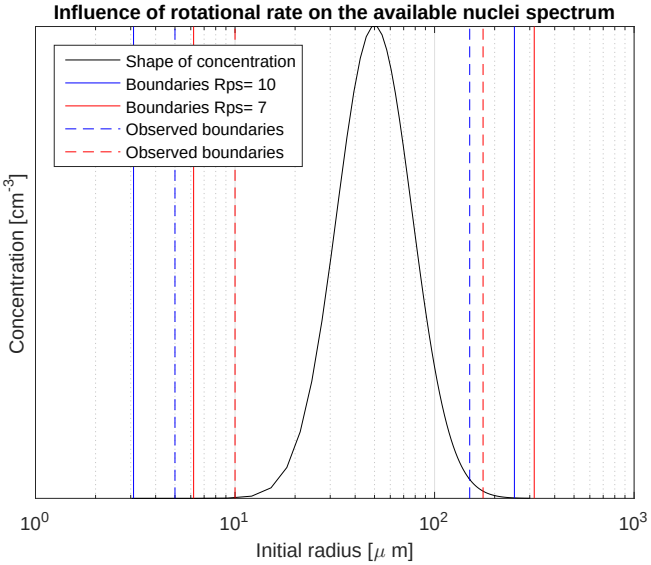

Figure 9.13: A typical nuclei distribution ([32]) and a comparison between the theoretical and the observed boundaries.

9.7.2 Increasing the cavitation number

An increased cavitation number leads to a smaller area where $p < p_v$. Therefore, the streamline hitting the area $p < p_v$ will start closer to the dividing streamline. The critical radius fitting in the low pressure area is smaller, leading to a lower approximate upper limit. Finally, larger nuclei remain stable in the minimum pressure point, leading to a higher minimum radius line. The result can be seen in Figure 9.14.

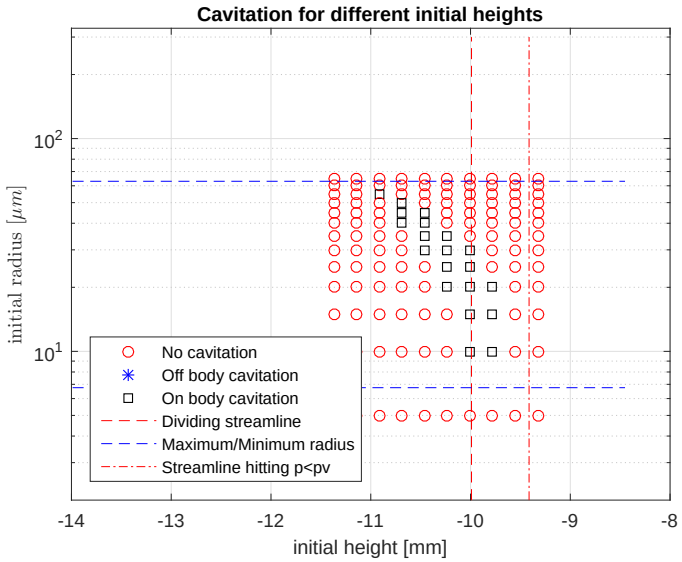

Figure 9.14: The cavitation behavior for a propellor blade section with $\sigma_{v,n} = 4$ and $n_{prop} = 10\,s^{-1}$.

9.8 Cavitation event rate

The cavitation event rate, $\dot{E}$, depends on the number of nuclei reaching the profile and the percentage of those who cavitate. The number of nuclei in the flow is determined by the concentration, C, see Figure 9.15. The total number of nuclei per cubic centimeter is $\sum C = 2\,cm^{-3}$. The concentration profile is approximated based on [32].

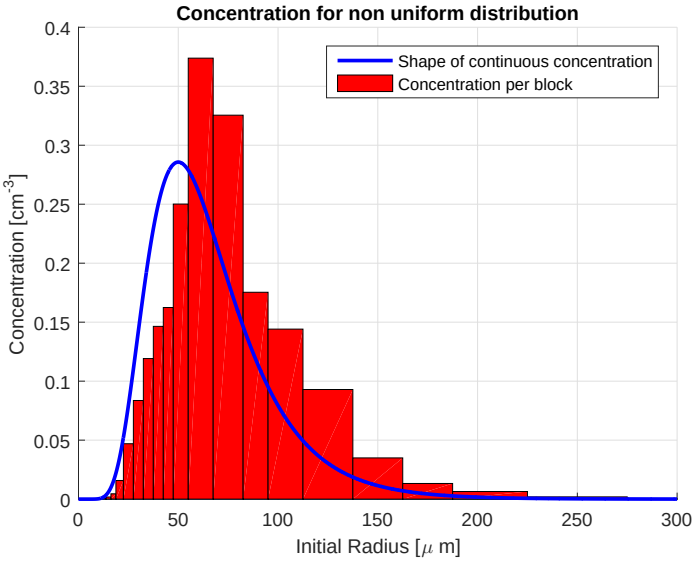

Figure 9.15: A continues concentration profile and a non continues concentration profile with non uniform step size. Approximated using [32].

The cavitation event rate in a 2D situation is 0, therefore the cavitation event rate will be evaluated per meter which will be denoted as: $\dot{E}'$, see Eq. 9.4.

$$\dot{E}'|_{R_0} = C|_{R_0} \Delta y_0|_{R_0} U_0 \tag{9.4}$$

The cavitation event rate per meter for a set of initial radii depends on the volume flow per meter through the bandwidth of initial heights for these initial radii and the concentration. The bandwidth of initial heights for an initial radius can be extracted from Figures 9.11-9.12. The bandwidth of initial heights has been given for Figure 9.11 in Figure 9.16.

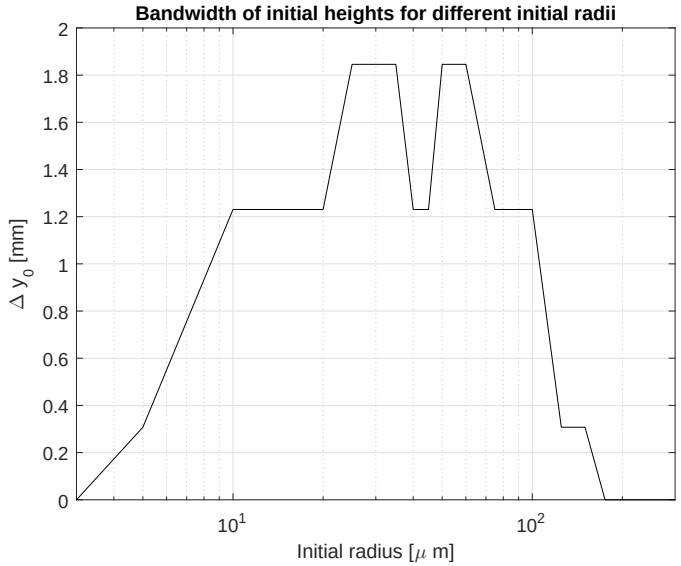

Figure 9.16: Bandwidth of initial heights per initial radius extracted from Figure 9.11.

Clearly, Figure 9.16 depends highly on the resolution of Figure 9.11. Finally, the cavitation event rate per meter can be found, see Figure 9.17

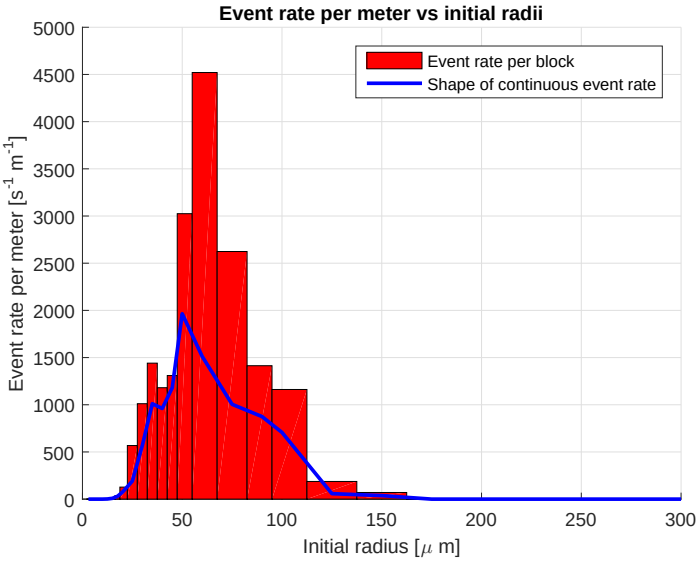

Figure 9.17: Cavitation event rate per meter for different initial radii derived from Figure 9.11.

The continuous cavitation event rate is determined using the continuous concentration. The sum of the cavitation event rates per meter per box of initial radii gives the total cavitation event rate per meter. Which is for this case $\sum \dot{E}' \approx 18700\, m^{-1}s^{-1}$.

The cavitation event rate per meter derived from Figure 9.14 can be found in Figure 9.18 with a total cavitation event rate per meter of $\sum \dot{E}' \approx 2100\, m^{-1}s^{-1}$. The cavitation event rate decreases with increasing cavitation number as expected. The variation of the nuclei size for different cavitation numbers is not taken into account.

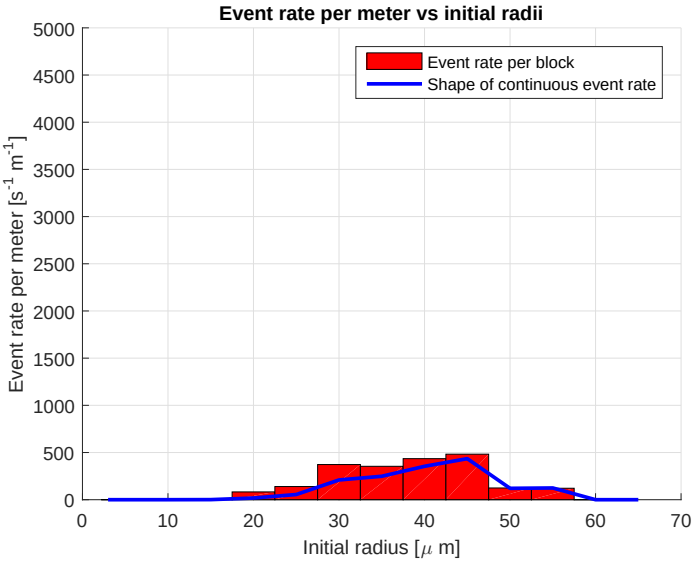

Figure 9.18: Cavitation event rate per meter for different initial radii derived from Figure 9.14.

The cavitation event rate per meter derived from Figure 9.12 yields a total cavitation event rate per meter of $\sum \dot{E}' \approx 12700\, m^{-1}s^{-1}$, the decrease in cavitation event rate is mostly due to the decrease in volume flow per meter.

Even though the cavitation event rate has been determined for a Schiebe headform in [4], the order of magnitude can be estimated on the found cavitation event rates. The Schiebe headform has a diameter of $5.08\,cm$, which yields cavitation event rates in the order of $\dot{E} \sim 100 - 1000\,s^{-1}$. This is in the same order of magnitude as found in [4].

The difference between the cavitation event rate and the available nuclei spectrum has been illustrated. Most striking is the difference between the cavitation event rates for the different rotational rates, as the cavitation event rate for the lower rotational rate is lower even though the available nuclei spectrum is wider.

VISCOUS FLOW

In the last part, an introduction to viscous effects on mainly the equation of motion is given. Furthermore, a method of dealing with an externally provided flow field is proposed.

10 Interpolating in a provided flow field

The objective of interpolating is to find a property at a location in which the actual value of this property is not known. Previously, the properties of the flow field were known analytically by means of a potential flow model. In this chapter, the usage of an externally provided flow field defined in certain grid points is examined.

The requirement on an externally provided flow field in 2D is that the locations of the grid points are known, (x_g, y_g), and that in these grid point locations the flow properties velocity, $\mathbf{w}(\mathbf{x}_g)$, and pressure, $p(\mathbf{x}_g)$, are known.

The grid will be subdivided in triangles using the *delaunayTriangulation* function of MATLAB. Using *pointLocation*, which is a function of MATLAB as well, the triangle in which the property is wanted is obtained. The three grid points defined by the triangle will be used to interpolate the flow property. Apart from the flow property, the gradient of the flow property is retrieved. If the flow property of interest is $q_0(\mathbf{x}_0)$ and the triangle points are numbered from 1 to 3, then the Taylor series for these points can be written, see Eq. 10.1, where $\Delta x_{g,i} = x_{g,i} - x_0$ and $\Delta y_{g,i} = y_{g,i} - y_0$.

$$\begin{aligned} q_1 &\approx q_0 + \left.\frac{\partial q}{\partial x}\right|_0 \Delta x_{g,1} + \left.\frac{\partial q}{\partial y}\right|_0 \Delta y_{g,1} \\ q_2 &\approx q_0 + \left.\frac{\partial q}{\partial x}\right|_0 \Delta x_{g,2} + \left.\frac{\partial q}{\partial y}\right|_0 \Delta y_{g,2} \\ q_3 &\approx q_0 + \left.\frac{\partial q}{\partial x}\right|_0 \Delta x_{g,3} + \left.\frac{\partial q}{\partial y}\right|_0 \Delta y_{g,3} \end{aligned} \tag{10.1}$$

At the location of interest, the set of equations can be solved in terms of q_1, q_2 and q_3. The result is the interpolated property and the approximated derivatives at the location of interest.
If second order derivatives are needed three more points need to be added. Higher order interpolation might be troublesome as no conditions on the continuity of the flow field are specified.
To extend the current interpolation to a 3D situation, the 3D grid needs to be subdivided into pyramids.

11 Viscous effects in the equation of motion

In this chapter, the equation of motion derived in Chapter 6 is reviewed for steady viscous flows. The Saffman lift force, the Magnus lift force and the Faxén correction force are a consequences of viscous flow. In [29] expressions for these forces can be found.

The Saffman lift force is a consequence of the vorticity of the flow. If the velocity of the flow is higher above the nucleus than below the nucleus and the nucleus moves with a relative velocity to the flow, then a pressure difference over the nucleus will exist. This pressure difference leads to a lift force. The Saffman lift force in 2D is given in Eq. 11.1.

$$\begin{aligned}
\mathbf{F}_{L,S} =& 9.66\frac{2}{3}R^2\rho_f C_{L,S}\sqrt{\frac{\nu_f}{|\omega_f|}}\left(\mathbf{w}-\mathbf{w}_p\right)\omega_f \quad \text{Where:} \\
C_{L,S} =& \begin{cases} 0.3314\sqrt{\frac{R|\omega_f|}{|\mathbf{w}-\mathbf{w}_p|}}\left(1-e^{-\frac{\mathrm{Re}_p}{10}}\right)+e^{-\frac{\mathrm{Re}_p}{10}} & \mathrm{Re}_p \leq 40 \\ 0.0524\sqrt{\mathrm{Re}_p\frac{R|\omega_f|}{|\mathbf{w}-\mathbf{w}_p|}} & \mathrm{Re}_p > 40 \end{cases}
\end{aligned} \tag{11.1}$$

ω_f is the vorticity of the 2D flow field and given by: $\omega_f = \frac{\partial v}{\partial x} - \frac{\partial u}{\partial y}$. The Saffman lift force will be implemented in the equation of motion. The implementation is straight forward, the Saffman lift force will be added to the force balance of Eq. 6.30.

The Magnus lift force is a consequence of the rotation of the nucleus. The Magnus lift force will not be taken into account as to track the rotation of a nucleus a new set of equations based on torque should be introduced. Moreover, the current model is based on a single nucleus, in reality the interaction between nuclei will greatly influence the rotation of the nucleus.

The Faxén correction force is a force which is a consequence of taking the equation of motion in the center of mass of the nucleus. If a flow field has varying vorticity the velocity of the flow at the center of mass of the nucleus might not be a good representation of the flow velocity experienced by the nucleus. The Faxén correction force is the force due to the second order effects in the flow, and is therefore related to the Laplacian of the flow field. Corrections on higher order effects in the flow could be included as well, see [29] Chapter 3. The flow field should for these corrections be resolved with at least the spatial accuracy of the order of the correction. The Faxén correction force will not be included as the second order derivatives will not be determined (Eq. 10.1).

The idea of the Faxén correction force is applicable to the pressure. The pressure is namely taken in the middle point of the nucleus. This pressure might not be fully representable for the experienced pressure.

12 Viscous flow results

12.1 The provided flow field

In [33] the influence of a roughness element on cavitation inception is studied. A roughness element decreases the minimum pressure on the profile significantly for sufficiently large flow Reynolds numbers ($\mathrm{Re}_f > 10^5$), see [33].
The influence of a roughness element on the cavitation behavior will be studied with the current model, yielding two flow fields. A flow field without the roughness element and a flow field with the roughness element. The NACA0015 profile can be seen in Figure 12.1. The flow Reynolds number is $\mathrm{Re}_f = 3.6 \cdot 10^5$, the chord length is $c = 60\,mm$, the angle of attack is $\alpha = 6^\circ$ and the inflow velocity is $U_0 = 6\,ms^{-1}$. In Figure 12.2, the roughness element can be seen, the roughness element has a height of $\varepsilon = 60\,\mu m$. The flow field is calculated in 3D using a RANS (Reynolds Avaraged Navier Stokes) solver, the flow is thus steady. The provided flow fields are 2D cuts of the 3D result.

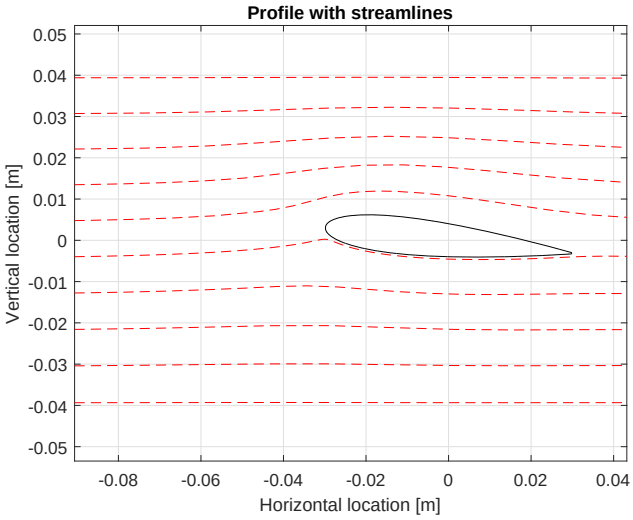

Figure 12.1: Profile and streamlines for the profided flow field. $\mathrm{Re}_f = 3.6 \cdot 10^5$.

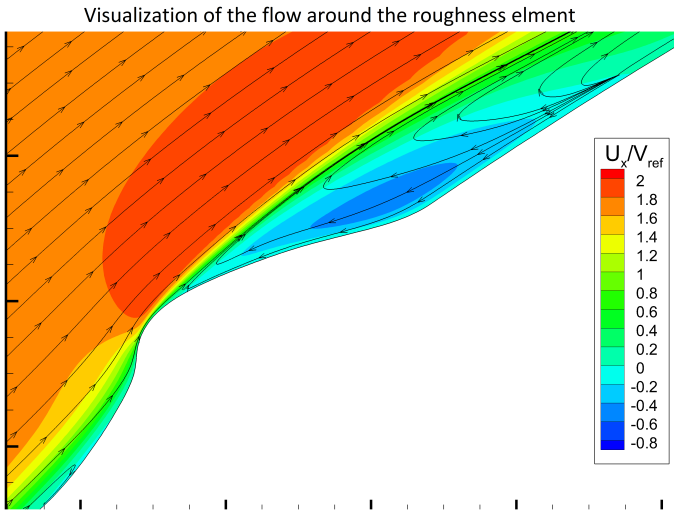

Figure 12.2: Visualization of the roughness element. $\mathrm{Re}_f = 3.6 \cdot 10^5$.

The roughness element is placed close to the minimum pressure point if no roughness element were present. This area is of interest as in this region the pressure can be below the vapor pressure. In this region the boundary layer can be seen to not extend more than the height of the roughness element (Figure 12.2). The flow fields are chosen such that the roughness element would be higher than the boundary layer at the location of the roughness element. Nuclei with diameters smaller than the height of the roughness element might be captured in the boundary layer.

12.2 Influence of the Saffman lift force

The influence of the Saffman lift force can not be seen in terms of different trajectories. The Saffman lift force will namely start to influence the force balance close to or in the boundary layer. If nuclei collapse, the Kelvin impulse related forces take over the force balance and the lift force is negligible. For illustration purposes, a nucleus which will be screened too much is used so that collapses are prevented. The resulting trajectory can be seen in Figure 12.3. The resulting forces in the vertical direction are given in Figure 12.4. The vertical direction is chosen as the normal of the profile is nearly vertical where the nucleus hits the profile. The Saffman lift force influences the force balance shortly before impact. The amount of time the force acts on the nucleus is too short to alter the trajectory significantly. To study the influence of the Saffman lift force correctly, a force balance based impact model should be implemented.

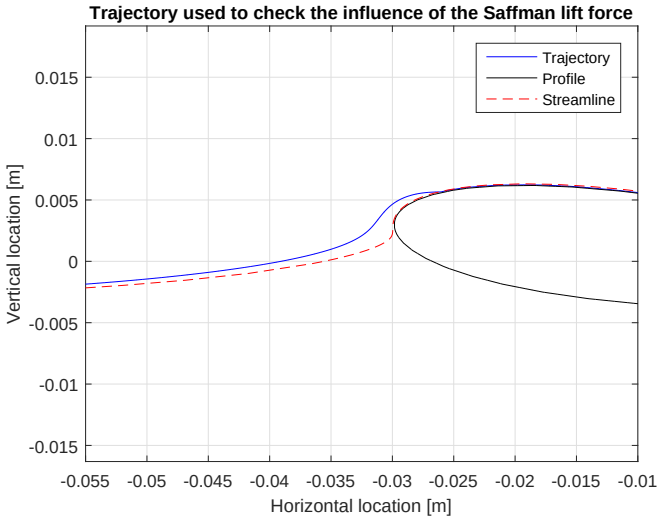

Figure 12.3: Trajectory of a nucleus with initial radius of $R_0 = 43\,\mu m$. $\mathrm{Re}_f = 3.6 \cdot 10^5$ and $\sigma_v = 2.15$.

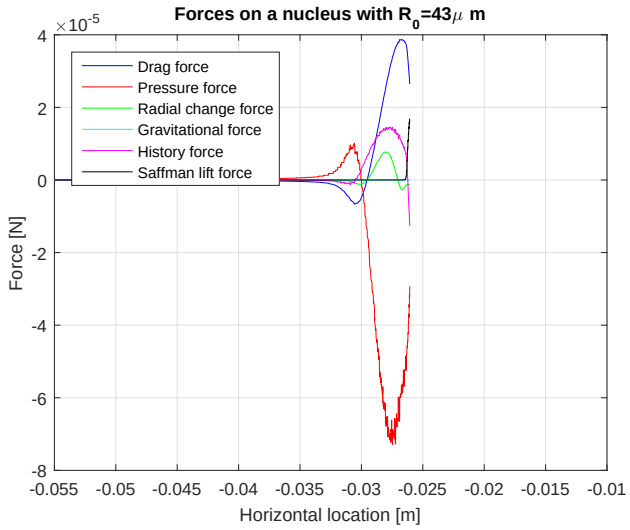

Figure 12.4: Forces on a nucleus with initial radius of $R_0 = 43\,\mu m$. $\mathrm{Re}_f = 3.6 \cdot 10^5$ and $\sigma_v = 2.15$.

12.3 Non-symmetric screening

Having a symmetric profile under an angle of attack will still yield non-symmetric screening, as from the point of view of the flow the profile is non-symmetric. In Figure 12.5, the cavitation behavior for the profile without the roughness element can be seen. The minimum stable radius has not been shown as it is $R_{0,min} = 1.6\,\mu m$ yielding too large computational times. The most outstanding result is the caviting nucleus larger than the approximated maximum radius. In this case, the dynamical effects of the nucleus yield an underestimation of the maximum radius. The reaction time of the nucleus makes the nucleus react delayed to the increased pressure. Additionally, nuclei reaching half their critical radius have been included as in [33] it has been made plausible that nuclei do not necessarily need to reach their critical radius to induce sheet cavitation inception.

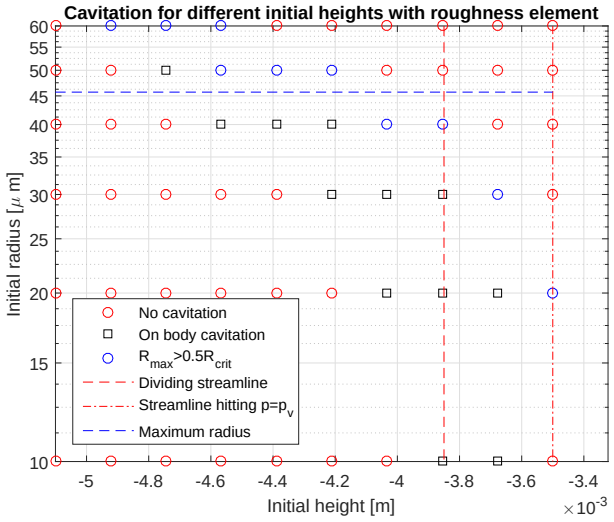

Figure 12.5: Cavitation on the profile without the roughness element. $\mathrm{Re}_f = 3.6 \cdot 10^5$ and $\sigma_v = 2$.

In Figure 12.6, the cavitation behavior for the flow field with the roughness element can be seen. The roughness element increases the area where the pressure is below the vapor pressure. The nucleus starting at $y_0 \approx -3.5 \cdot 10^{-3}\, m$ with an initial radius of $R_0 = 20\, \mu m$ does cavitate where this would not have happened without the roughness element. At the same initial height the nucleus with an initial radius of $R_0 = 10\, \mu m$ reaches half the critical radius where this would not have happened without the roughness element. The roughness element yields more growth but the extra growth does not represent the extra growth observed in experiments, see [33].

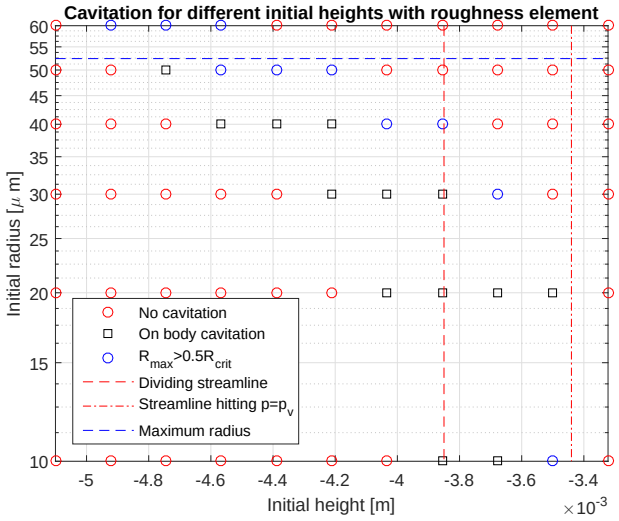

Figure 12.6: Cavitation on the profile with the roughness element. $\mathrm{Re}_f = 3.6 \cdot 10^5$ and $\sigma_v = 2$.

In [33], two gas nuclei with initial radii of $R_0 = 18.5\, \mu m$ and $R_0 = 43\, \mu m$ have been tracked. Both nuclei produce a streak of cavitation, the larger nucleus produces a longer streak. The experiments have been carried out with an incoming flow of approximately $U_0 = 8\, ms^{-1}$. The flow fields will be scaled such that the same free stream velocity is used. Scaling the flow clearly undermines the Reynolds dependent flow features such as boundary layer build up. In Figure 12.7, the different growth behavior can be found. In general, the roughness element induces more growth. Remarkable is that the roughness element seems to influence the flow

such that a nucleus with an initial radius of $R_0 = 43\,\mu m$ ends above the profile where without the roughness element this would not have happened. Furthermore, the larger nucleus will never reach the critical radius.

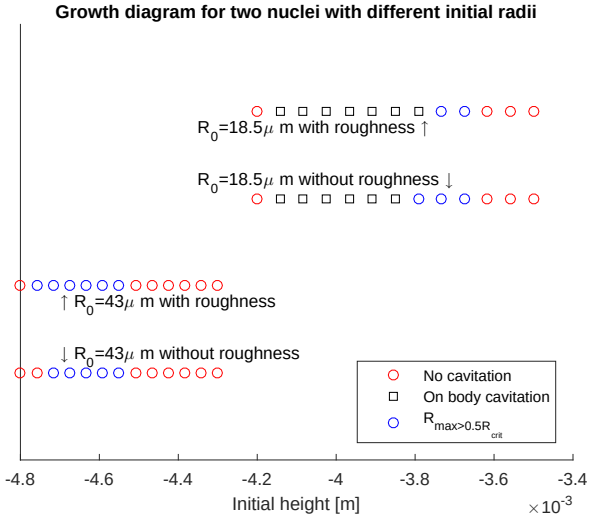

Figure 12.7: Visualization of the difference between having and not having a roughness element. $\mathrm{Re}_f \approx 5.1 \cdot 10^5$ and $\sigma_v = 2.15$.

12.4 Solid particle

The equation of motion has been set up such that it would be suitable for both gas and solid nuclei. Solid nuclei might influence cavitation inception, see [1]. The behavior of solid nuclei is opposite to that of gas nuclei as the density of solid nuclei is usually larger than that of the surrounding liquid. Gravity has a more significant influence on solid nuclei. In Figure 12.8, the trajectories of gas nuclei with a density of $\rho_p = 1\,kgm^{-3}$ and the trajectories of solid nuclei with a density of $\rho_p = 7850\,kgm^{-3}$ are compared. The larger the initial nuclei size, the more the corresponding trajectories deviate.

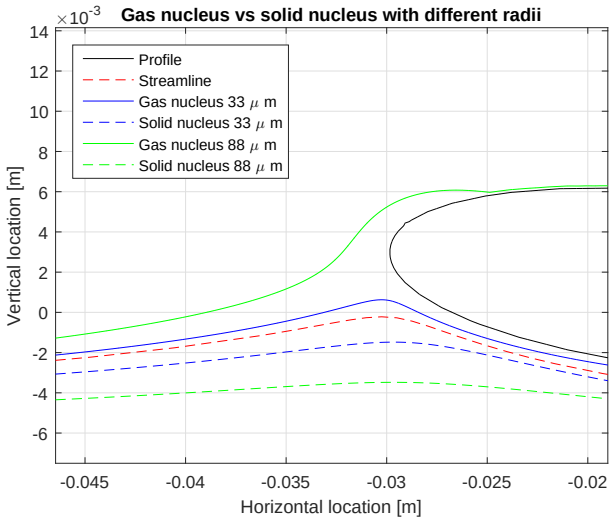

Figure 12.8: Comparison between gas and solid nuclei, with densities of $\rho_p = 1$ and $7850\,kgm^{-3}$. $\mathrm{Re}_f = 3.6 \cdot 10^5$ and $\sigma_v = 2.15$.

For solid nuclei, it can be checked if the nucleus would hit the profile in the area where the pressure is below the vapor pressure. In Figures 12.9-12.10, it is shown wheter the nuclei hit the profile in the low pressure area. There is no maximum nucleus radius for solid nuclei which are able to hit the profile as starting higher is always an option.

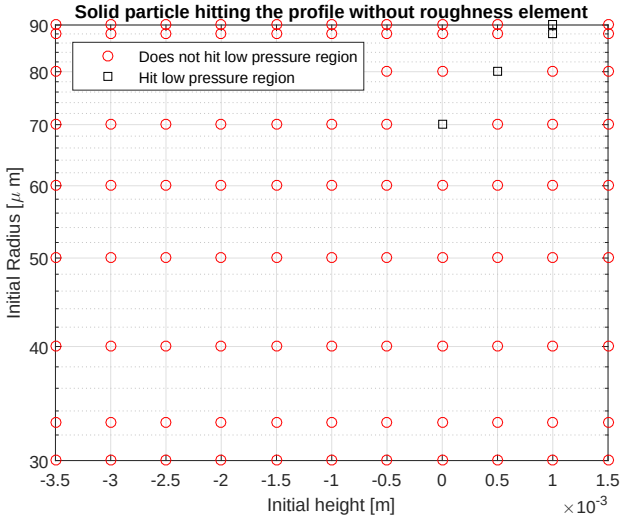

Figure 12.9: Solid nuclei with a density of $\rho_p = 7850\,kgm^{-3}$ hitting the profile without roughness element. $\mathrm{Re}_f = 3.6 \cdot 10^5$.

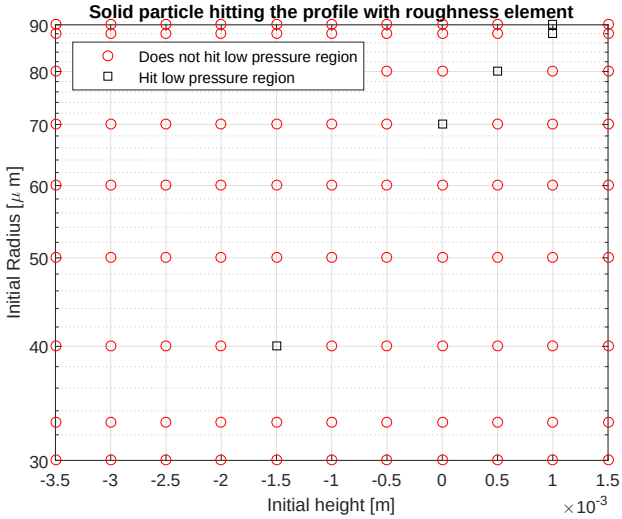

Figure 12.10: Solid nuclei with a density of $\rho_p = 7850\,kgm^{-3}$ hitting the profile with roughness element. $\mathrm{Re}_f = 3.6 \cdot 10^5$.

In the case of a roughness element, there is one more hit detected. This is most likely more a geometric consequence than a flow field related consequence.
In both Figures 12.9-12.10, the trend can be seen that larger nuclei need to start at a higher location to hit the profile. This behavior is opposite to that of gas nuclei, the same effect is shown in Figure 12.8.

13 Conclusions

The conclusions are given in the same order as the report is written.

The elementary model gave insight in scale effects. Large nuclei do not deviate from their streamlines according to the scaling laws derived for small nuclei in the Stokes limit. Small nuclei do deviate from their streamlines according to these scaling laws. The equivalent Stokes number makes large and small nuclei distinguishable, the classification of the size of nuclei depends on the free stream velocity and on the size of the object in the flow. If a nucleus deviates too much from the streamline, the nucleus will not encounter low enough pressures to cavitate. This effect is called screening, screening is most evident on symmetric profiles at zero incidence and provides an upper limit on the available nucleus size for cavitation.
The growth of nuclei influences the trajectory of the nucleus. In the limit for large Weber numbers changing the Weber number does not influence the trajectory significantly. The equivalent Stokes number should be used over the flow Reynolds number to estimate scale effects.

Benefiting from an actual bubble dynamics equation, a more complete equation of motion and a wider variety of available profile shapes, the model described in the second part provided more insight on, in particular, non-symmetric screening.
The more involved equation of motion showed that the history force is relevant in liquids contaminated with surfactants.
The mayor downfall of the presented model is that nuclei need to remain spherical. By means of the modified Eötvös number, the deformation of nuclei can quantitatively be estimated. The modified Eötvös number correlates strongly, only delayed, with the square of the particle Reynolds number.
The most striking result is that the screening effect does not seem to play a role in flows with non-symmetric profiles or with symmetric profiles at incidence. Under these non-symmetric conditions nuclei can start below the dividing streamline and end up above the profile. Stability of nuclei along with the dynamical effects, captured in the bubble dynamics equation, determines the maximum nucleus radius available for cavitation.
The cavitation event rate provides more useful information on the expected cavitation behavior than focusing on the available nuclei spectrum.

Viscous simulations showed that the Saffman lift force can only be implemented correctly if the impact model is force balance based.
Comparing the growth of nuclei in a flow field without a roughness element and a flow field with a roughness element showed that the roughness element induced more growth. The amount of extra growth is not significant enough to assume the growth of gas nuclei to be the sole cause of the cavitation behind a roughness element.
Finally the trajectories of solid nuclei and gas nuclei have been compared. Having a higher density than the liquid, the solid nuclei react opposite to the pressure gradient force.

14 Recommendations

The recommendations will be mentioned point wise.

- Under non-symmetric conditions it was shown that screening plays no role. Non-symmetric conditions are required to generate lift, yielding that for practical applications non-symmetric conditions are the standard. If experiments are conducted it is therefore advised to take non-symmetric conditions.
- In order to keep the cavitation number constant while changing the free stream velocity, the surrounding pressure needs to be changed. Therefore, the influence of the surrounding pressure on the nuclei spectrum needs to be included.
- Using conformal transformation the influence of the nose radius should be examined. More variations in for example the camber can be studied as well.
- A history kernel dependent on the drag factor should be implemented if the influence of the shape of the nucleus on the drag factor is known.
- If the trajectory of a nucleus is of interest past the low pressure zone, the influence of the Saffman lift force should be reevaluated using a force balance based impact model.
- Interpolation in the provided flow field using Taylor series leads to problems for higher order derivatives. To compensate for this fact Hermite interpolation could be used, for this interpolation type the continuity of the flow field can be specified.
- The cavitation event rate should be focused on more than on the available nuclei spectrum, since the cavitation event rate is more relatable to what is observed in experiments.
- An integration method based on the difference between two results calculated with different order schemes should be implemented to determine the variable time step on a more solid base.
- More experimental validation of the model is required.

Bibliography

[1] Martijn van Rijsbergen, 2016 *A review of sheet cavitation inception mechanisms* International symposium on transport phenomena and dynamics of rotating machinery 2016

[2] Virgil E. Johnson, Jr., and Tsuying Hsieh, 1966 *The influence of the trajectories of gas nuclei on cavitation inception*, 6th Symposium on Naval Hydrodynamics 1966

[3] Zheng Cui *Rutherford Appleton Laboratory, Oxford, UK*

[4] Zhenhuan Liu, Christopher E. Brennen, 1998 *Cavitation nuclei population and event rates*, Journal of fluids engineering, volume 120, december 1998

[5] Y.Chizelle, S. Ceccio, C. Brennen, Y. Shen,1992 *Cavitation Scaling Experiments With Headforms: Bubble Acoustics*, 1992

[6] Y. Chizelle, S. Ceccio, C. Brennen, 1995 *Observation ans scaling of travelling bubble cavitation*, Journal of Fluid Mechanics, volume 293, 1995

[7] Vijay H Arakeri, 1979 *Cavitation inception*, Proc. Indian Acad. Sci., Volume C2, may 1979

[8] Michael P. Brenner, Sacha Hilgenfeldt and Detlef Lohse, 2002 *Single-bubble sonoluminescence*, Reviews of modern physics, volume 74, april 2002

[9] Andrea Prosperetti, *Bubble dynamics: Some things we did not know 10 years ago*

[10] John R. Blake, 1988 *The Kelvin impulse: application to cavitation bubble dynamics*, J. Australian Mathamatical society, 1988

[11] John R. Blake, David M. Leppinen and Qianxi Wang, 2015 *Cavitation and bubble dynamics: the Kelvin impulse and its applications* Interface Focus 5: 20150017

[12] Evert Klaseboer, Rogerio Manica, Marice H. W. Hendrix, Claus-Dieter Ohl and Derek Y.C. Chan, 2014 *A force balance model for the motion, impact, and bounce of bubbles* Physics of fluids 26, 092101, 2014

[13] E. Giannadakis, M. Gavaises, H. Roth and C. Arcourmanis, 2004 *Cavitation Modelling in Single-Hole Diesel Injector based on Eulerian-Lagrangian approach* conference on thermo- and Fluid dynamic processe in diesel engines, Thiesel 2004

[14] E. Giannadakis, M. Gavaises and C. Arcourmanis, 2007 *Modelling of cavitation in diesel injector nozzles* J. Fluid Mech. (2008), vol. 616, pp. 153-193

[15] T. Miloh, 1977 *Hydrodynamics of deformable contiguous spherical shapes in an incompressible inviscid fluid* Journal of Engineering Mathematics, Vol. 11, no. 4, October 1977

[16] A. S. Sangani, D. Z. Zhang and A. Prosperetti, 1991 *The added mass, Basset, and viscous drag coefficients in nondilute bubbly liquids undergoing small-amplitude oscillatory motion* Physics of Fluids A: Fluid Dynamics 3, 2955(1991)

[17] C. D. Ohl, A. Tijink and A. Prosperetti, 2002 *The added mass of an expanding bubble* J. Fluid MEch. (2003)

[18] Shu Takagi and Yoichiro Matsumoto, 2011 *Surfactant effects on bubble motion and bubbly flows* Annu. Rev. Fluid Mech. 2011

[19] I. Roghair, Y.M. Lau, N.G. Deen, H.M.Slagter, M.W. Baltussen, M. Van Sint Annaland and J.A.M. Kuipers, 2011 *On the drag force of bubbles in bubble swarms at intermediate and high Reynolds numbers* Chemical Engineering Science 66 (2011)

[20] W. Dijkhuizen, I. Roghair, M. van Sint Annaland and J.A.M. Kuipers, 2010 *DNS of gas bubbles behaviour using an improved 3D front tracking model–Drag force on isolated bubbles and comparison with experiments* Chemical Engineering Science 65 (2010)

[21] M.X. van Rijsbergen and T.J.C. van Terwisga, 2011 *High-speed micro-scale observations of nuclei-induced sheet cavitation* WIMRC 3rd International Cavitation Forum 2011

[22] J. Magnaudet and I. Eames, 2000 *The motion of high-Reynolds-number bubbles in inhomogeneous flows* Annu. Rev. Fluid Mech. 2000

[23] Christopher E. Brennen, 1995 *Cavitation and bubble dynamics* Oxforc university press

[24] Martin R. Maxey and James J. Riley, 1983 *Equation of motion for a small rigid sphere in a nonuniform flow* Phys. Fluids 26(4), april 1983

[25] Vamsi Spandan, Rodolfo Ostilla-Mónico, Roberto Verzicco and Detlef Lohse, 2016 *Drag reduction in numerical two-phace Tayler-Couette turbulence using an Euler-Lagrange approach* J. Fluid Mech. (2016), vol 798

[26] Irene M. Mazzitelli, Deltlef Lohse and Federico Toschi, 2003 *The effect of microbubbles on developed turbulence* Physics of Fluids Volume 15, number 1 January 2003

[27] Dirk F. van Eijkeren and Harry W. M. Hoeijmakers 2010 *Influence of the history term in a Lagrangian method for oil-water separation* 7th international conference on multiphase flow, june 2010

[28] Dirk F. van Eijkeren and Harry W. M. Hoeijmakers 2013 *The influence of the history force in Lagrangian particle tracking applied to swirling flow produced water treatment* 8th international conference on multiphase flow, may 2013

[29] Dirk F. van Eijkeren 2016 *Dispersed dropled dynamics during produced water treatment in oil industry*

[30] Derek Y.C. Chan, Evert Klaseboer and Rogerio Manica, 2011 *Theory of non-equilibrium force measurements involving deformable drops and bubbles* Advances in Colloid and Interface Science 165(2011)

[31] Martijn X. van Rijsbergen, Tom J.C. van Terwisga, 2010 *Water quality effects on sheet caviataion inception on a ship propeller model* 7^{th} international conference on multiphase flow 2010

[32] M.Birvalski and M.X. van Rijsbergen, 2018 *Size and concentration measurements of cavitation nuclei in the wake of a ship model* 10^{th} international cavitation symposium 2018

[33] Martijn van Rijsbergen and Jesse Slot, 2015 *Bubble-induced sheet cavitation inception on an isolated roughness element* 9^{th} international symposium on cavitation 2015

Appendices

A Static stability of spherical gas bubbles

The assumptions made to support the derivation of a quasi-steady nucleus growth equation are as follows:

- The nucleus is assumed to be spherical regardless of the flow features.
- It is assumed that pressure changes slowly so that mechanical equilibrium is still satisfied.
- The gas inside the nucleus is isothermal.
- The gas inside the nucleus is isobaric.

Figure A.1 shows a schematic overview of the situation.

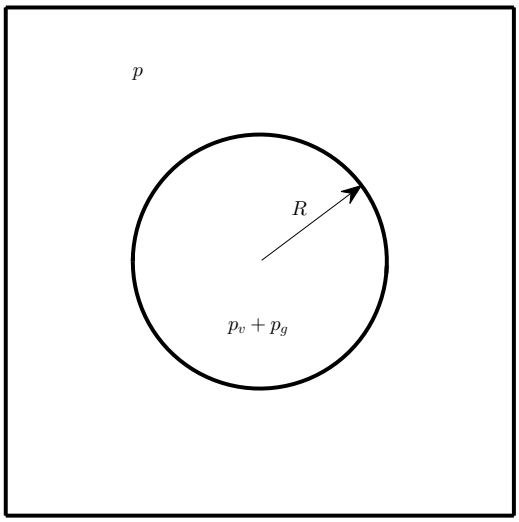

Figure A.1: Sketch of a gas nucleus with radius R in a liquid

To get static stability, the sum of the forces acting on any point in the nucleus needs to be zero. This will in general not yet be the case since the surface tension is not included. The surface tension will account for the difference in pressure over the boundary of the nucleus. Imagine to cut the nucleus in half, so the cut should go along the middle of the sphere. Then the force that is exerted by the pressure difference felt by the boundary of the cut is equal to the pressure difference times the projected area (a circle with radius R). This projected area is the effective area on which the pressure works in a force balance in any direction, since the cut of a sphere is directional independent. The surface tension works on the edge of the cut of the sphere, and thus has a work line described by the circumference of a circle. In equation form we get the force balance shown in Eq. A.1.

$$F_{\Delta p} = F_{\gamma} \tag{A.1}$$

In which $F_{\Delta p}$ stands for the force exerted by the pressure difference which is given by $F_{\Delta p} = \Delta p \pi R^2$. F_γ stands for the force exerted by the surface tension which is given by $F_\gamma = \gamma 2\pi R$. The result can be found in Eq. A.2.

$$\Delta p \pi R^2 = \gamma 2\pi R \quad \rightarrow \quad \Delta p = \frac{2\gamma}{R} \tag{A.2}$$

The pressure difference is positive if the pressure inside the nucleus is larger then the pressure outside the nucleus. Using this, Eq. A.3 is derived.

$$p_g + p_v - p = \frac{2\gamma}{R} \quad \rightarrow \quad p = p_g + p_v - \frac{2\gamma}{R} \tag{A.3}$$

Eq. A.3 is the equation for static stability of a nucleus, which is known as the Blake threshold, and holds at any point in a flow field. At an initial location, Eq. A.4 will be found.

$$p_0 = p_{g0} + p_v - \frac{2\gamma}{R_0} \tag{A.4}$$

p_0 is the reference pressure at a point where the nucleus has radius R_0. The vapor pressure is not dependent on the location in the flow field since the composition of the liquid does not change, so $p_{v0} = p_v$. Furthermore, the partial gas pressure at any point can be related to the initial gas pressure by using the ideal gas law, since the temperature does not change one finds: $p_{g0}V_0 = p_g V$. This in turn gives $p_g = p_{g0}\frac{R_0^3}{R^3}$. Substitution in Eq. A.3 gives Eq. A.5.

$$p = p_{g0}\left[\frac{R_0}{R}\right]^3 + p_v - \frac{2\gamma}{R} \tag{A.5}$$

By rewriting Eq. A.5 and dividing by $p_0 - p_v$ Eq. A.6 can be found.

$$\frac{p - p_v}{p_0 - p_v} = \frac{1}{p_0 - p_v}\left(p_{g0}\left[\frac{R_0}{R}\right]^3 - \frac{2\gamma}{R}\right) \tag{A.6}$$

To get rid of the partial gas pressure Eq. A.4 is used once more leading to Eq. A.7.

$$\frac{p - p_v}{p_0 - p_v} = \frac{1}{p_0 - p_v}\left(\left[p_0 - p_v + \frac{2\gamma}{R_0}\right]\left(\frac{R_0}{R}\right)^3 - \frac{2\gamma}{R}\right) \tag{A.7}$$

If Eq. A.7 is rewritten conveniently, one gets Eq. A.8.

$$\frac{p - p_v}{p_0 - p_v} = \left(\frac{R_0}{R}\right)^3\left[1 + \frac{2\gamma}{(p_0 - p_v)R_0}\left(1 - \frac{R^2}{R_0^2}\right)\right] \tag{A.8}$$

Using the definition of the cavitation number and the Weber number leads to Eq. A.9.

$$\frac{p - p_v}{p_0 - p_v} = \left(\frac{R_0}{R}\right)^3\left[1 + \frac{8}{\sigma_v \mathrm{We}}\left(1 - \frac{R^2}{R_0^2}\right)\right] \tag{A.9}$$

Eq. A.9 in dimensionless form can be found by introducing the radius ratio, r, as $r = \frac{R_0}{R}$. And using the pressure coefficient, C_p. This yields Eq. A.10.

$$\frac{C_p + \sigma_v}{\sigma_v} = r^3 \left[1 + \frac{8}{\sigma_v \mathrm{We}} \left(1 - r^{-2} \right) \right] \tag{A.10}$$

Rewriting Eq. A.10 gives Eq. A.11.

$$r^3 - \frac{\frac{8}{\mathrm{We}}}{\sigma_v + \frac{8}{\mathrm{We}}} r - \frac{C_p + \sigma_v}{\sigma_v + \frac{8}{\mathrm{We}}} = 0 \tag{A.11}$$

Eq. A.11 is the same equation as Eq. A.9 but written in a solvable form when r is sought. Eq. A.11 is written shortly as: $r^3 - Pr - Q = 0$. A third degree polynomial can be solved, the solution depends on the discriminant. The discriminant of a third degree function of the form $ax^3 + bx^2 + cx + d$ is given by $\Delta = 18abcd - 4b^3d + b^2c^2 - 4ac^3 - 27a^2d^2$. In the case of Eq. A.11 the discriminant becomes: $\Delta = 4P^3 - 27Q^2$. By using the discriminant three cases can be distinguished, namely:

1. if $\Delta > 0$, then the equation has 3 distinct real roots
2. if $\Delta = 0$, then the equation has a multiple root and all of its roots are real
3. if $\Delta < 0$, then the equation has one real root and two complex roots

First, the case in which the local pressure p is greater then the vapor pressure p_v is considered. This means that $C_p + \sigma_v > 0$. If this is the case then Q will be positive just as P which is always positive. If then the case in which $Q^2 > \frac{4}{27}P^3$ is considered the discriminant will be negative($\Delta < 0$, case 3). When a third degree polynominal in the form of Eq. A.11 has one real root, this root can be found by Cardano's method. This gives Eq. A.12. Only real solutions are interesting since this problem is physical.

$$r = \sqrt[3]{\frac{1}{2}Q + \frac{1}{2}\sqrt{Q^2 - \frac{4}{27}P^3}} + \sqrt[3]{\frac{1}{2}Q - \frac{1}{2}\sqrt{Q^2 - \frac{4}{27}P^3}} \tag{A.12}$$

Note that $\frac{1}{2}Q$ has been forgotten in [2].

If now the case $C_p + \sigma_v > 0$ and $Q^2 < \frac{4}{27}P^3$ is considered the determinant becomes positive($\Delta > 0$, case 1), meaning 3 real solutions. The solution which will be relevant however needs to be positive since the radius of the nucleus will always be positive. The solutions for this case can be found by Viète's method the only positive solution is found in the case where $k = 0$. This gives Eq. A.13.

$$r = 2\sqrt{\frac{P}{3}} \cos\theta \quad \text{Where} \quad \theta = \frac{1}{3}\cos^{-1}\left(\frac{Q}{\sqrt{\frac{4}{27}P^3}} \right) \tag{A.13}$$

Note that the division is missing in [2].

Lastly the case where $C_p + \sigma_v < 0$ and $Q^2 < \frac{4}{27}P^3$ is considered. This means that the surrounding pressure is lower than the vapor pressure. In that case the determinant is again positive and the solution to the problem has therefore three real roots. In this case two positive solution can be found when, namely when $k = 0$ or $k = 1$ is taken. Only in the case

where $k = 1$ r is smaller than 1, meaning that the nucleus has grown which it should do since the surrounding pressure is lower than the vapor pressure. Similar to the previous case one can find Eq. A.14.

$$r = 2\sqrt{\frac{P}{3}}\cos\frac{\pi - \theta'}{3} \quad \text{Where} \quad \theta' = \cos^{-1}\left(\frac{Q}{\sqrt{\frac{4}{27}P^3}}\right) \tag{A.14}$$

Note that the division is again missing in [2].

With Eqs A.12-A.13-A.14 the third equation in [2] is reproduced.

One special case has not been investigated yet, namely the case where $Q^2 = \frac{4P^3}{27}$. This case is only of interest when $C_p + \sigma_v < 0$ so that the surrounding pressure is lower then the vapor pressure because only then this critical point will lead to massive growth of the gas nucleus. This phenoma is catagorized as cavitation inception in [2]. The critical pressure coefficient can be found by: $Q^2 = \frac{4P^3}{27}$ but to get a better understanding of the meaning of this critical point a plot of the outcome of Eq. A.9 is given in Figure A.2.

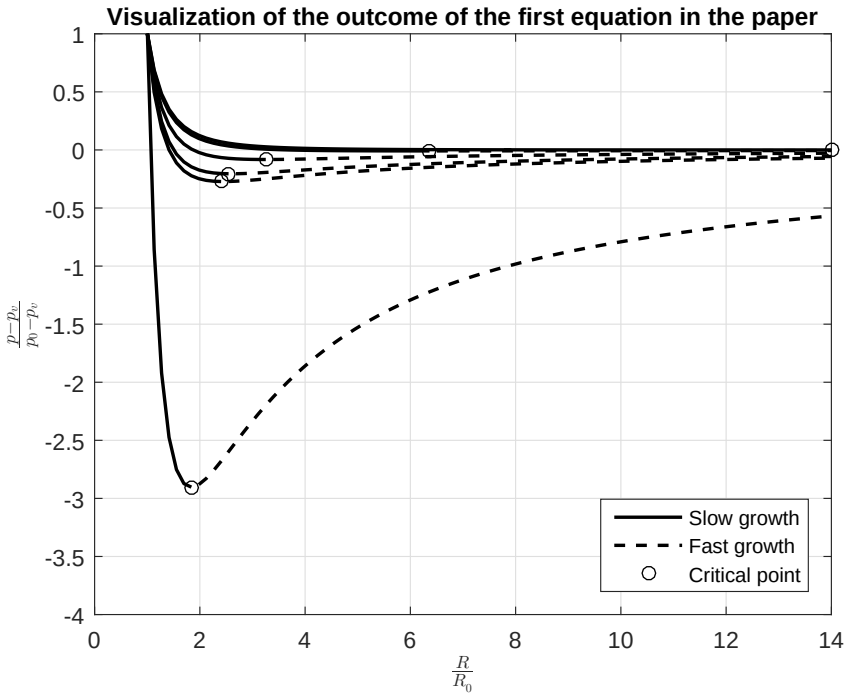

Figure A.2: The function given in Eq. A.9 plotted for different values of σ_vWe. The values used for σ_vWe are 1,8,10,20,100 and 1000, the higher this value the higher the critical point.

As can be seen in Figure A.2, there is a minimum pressure after which the particle begins to grow very fast. This point is called the critical point. It can be seen that all functions head towards the $\frac{p-p_v}{p_0-p_v} = 0$-line.
To find the minimums observed in Figure A.2 and to create decent understanding of the phenoma Eq. A.5 is used. Cavitation inception occurs at the minimal surrounding pressure reached, this point can be found by setting the derivative to zero, see Eq. A.15.

$$\frac{\partial p}{\partial R} = -3\frac{p_{g0}R_0^3}{R^4} + \frac{2\gamma}{R^2} \tag{A.15}$$

After setting the derivative to zero and some convenient rewriting Eq. A.16 is found.

$$R_{crit} = R_0 \sqrt{\frac{3p_{g0}}{\frac{2\gamma}{R_0}}} \tag{A.16}$$

In Eq. A.16 R_{crit} is the critical radius. Using this critical radius the critical pressure can be found by using Eq. A.5 again. This leads to Eq. A.17.

$$p_{crit} = p_{g0} \left(\frac{\frac{2\gamma}{R_0}}{3p_{g0}} \right)^{3/2} + p_v - \frac{2\gamma}{R_{crit}} \tag{A.17}$$

Rewriting Eq. A.17 gives Eq. A.18.

$$p_{crit} = \frac{2\gamma}{3R_0} \frac{R_0}{R_{crit}} + p_v - \frac{2\gamma}{R_{crit}} = p_v - \frac{4\gamma}{3R_{crit}} \tag{A.18}$$

So the critical pressure is known. Writing Eq. A.18 in dimensionless form requires the dimensionless critical radius. This can be found by using Eq. A.4 and using the cavitation and Weber number. This gives Eq. A.19.

$$R_{crit} = R_0 \sqrt{3 \left(\frac{\mathrm{We}\sigma_v}{8} + 1 \right)} \tag{A.19}$$

Filling in the critical radius found in Eq. A.19 into Eq. A.18 gives Eq. A.20.

$$p_{crit} - p_v = -\frac{4\gamma}{3\sqrt{3}R_0 \sqrt{\frac{\mathrm{We}\sigma_v}{8} + 1}} \tag{A.20}$$

Introducing the critical pressure coefficient as: $C_p^* = \frac{p_{crit} - p_0}{\frac{1}{2}\rho U^2}$ gives Eq. A.21.

$$C_p^* + \sigma_v = -\frac{\frac{16}{\mathrm{We}}}{3\sqrt{3}\sqrt{\frac{\mathrm{We}\sigma_v}{8} + 1}} \tag{A.21}$$

Rewriting Eq. A.21 gives Eq. A.22.

$$C_p^* + \sigma_v = -\frac{2\sigma_v \left(\frac{8}{\sigma_v \mathrm{We}} \right)^{3/2}}{3\sqrt{3} \left(1 + \frac{8}{\sigma_v \mathrm{We}} \right)^{1/2}} \tag{A.22}$$

Eq. A.22 could have also been found by stating $4Q^2 = 27p^3$, and is the same equation as the fourth equation in [2].

B Application to a two-dimensional half body in an infinite fluid

The flow potential is given in Eq. B.1.

$$\Phi = \frac{1}{2\pi}\ln(x^2+y^2) + x \tag{B.1}$$

This flow potential consist of a uniform flow field ($+x$-part) and a source in the point $(0,0)$. The source will account for the body in the flow. The integration constant is set to zero since in practice only the derivatives matter. The body shape found by this potential is given in Eq. B.2.

$$x = -y\cot\pi y \tag{B.2}$$

Eq. B.2 can be derived via the stream function. The analysis of the stream function just as the analysis of the potential have been left out of this derivation.
The flow potential can be differentiated to x and to y leading to the velocity components, see Eq. B.3.

$$\begin{aligned}\frac{\partial\Phi}{\partial x} &= u = 1 + \frac{1}{\pi}\frac{x}{x^2+y^2}\\ \frac{\partial\Phi}{\partial y} &= v = \frac{1}{\pi}\frac{y}{x^2+y^2}\end{aligned} \tag{B.3}$$

The dimensionless pressure gradients can be found by using the time independent Bernoulli's formula and neglecting gravity: $p_0 - p = \frac{1}{2}\rho_f(u^2+v^2)$. This formula in dimensionless form gives: $C_p = 1-(\hat{u}^2+\hat{v}^2)$, leading to Eq. B.4.

$$\begin{aligned}-\frac{\partial C_p}{\partial x} &= -\frac{2}{\pi}\frac{x^2-y^2+\frac{x}{\pi}}{(x^2+y^2)^2}\\ -\frac{\partial C_p}{\partial y} &= -\frac{2}{\pi}\frac{y\left(2x+\frac{1}{\pi}\right)}{(x^2+y^2)^2}\end{aligned} \tag{B.4}$$

Filling in Eq. B.3 and Eq. B.4 into the dimensionless equation of motion gives Eqs. B.5-B.6. The nucleus velocity is related to the nucleus position as $\hat{\mathbf{w}}_p \equiv \frac{d\mathbf{x}_p}{d\hat{t}} \equiv \dot{\mathbf{x}}_p$, $\mathbf{x}_p = \begin{bmatrix} x_p & y_p \end{bmatrix}^T$

$$\frac{d\dot{x}_p}{d\hat{t}} = \frac{18}{\hat{R}^2\mathrm{Re}_f}\frac{\mathrm{Re}_p C_D}{24}\left[\left(1+\frac{1}{\pi}\frac{x_p}{x_p^2+y_p^2}\right)-\dot{x}_p\right] - \frac{3}{\pi}\left[\frac{x_p^2-y_p^2+\frac{x_p}{\pi}}{(x_p^2+y_p^2)^2}\right] \tag{B.5}$$

$$\frac{d\dot{y}_p}{d\hat{t}} = \frac{18}{\hat{R}^2\mathrm{Re}_f}\frac{\mathrm{Re}_p C_D}{24}\left[\left(\frac{1}{\pi}\frac{y_p}{x_p^2+y_p^2}\right)-\dot{y}_p\right] - \frac{3}{\pi}\left[\frac{y_p\left(2x_p+\frac{1}{\pi}\right)}{(x_p^2+y_p^2)^2}\right] \tag{B.6}$$

Finally, the nucleus Reynolds number can be found by using the flow velocity found in Eq. B.3. This gives Eq. B.7.

$$\mathrm{Re}_p = \hat{R}\mathrm{Re}_f \left\{ \left[\left(1 + \frac{1}{\pi} \frac{x_p}{x_p^2 + y_p^2} \right) - \dot{x}_p \right]^2 + \left[\left(\frac{1}{\pi} \frac{y_p}{x_p^2 + y_p^2} \right) - \dot{y}_p \right]^2 \right\}^{1/2} \tag{B.7}$$

C Order reduction

For efficient computation, first-order differential equations are preferred, and therefore the second-order nonlinear ODE's given by Eqs. B.5-B.6-B.7 will be written as a system of first-order ODE's. This is done by introducing the vector $\mathbf{z}$. The definition of the vector is given in Eq. C.1.

$$\mathbf{z} = \begin{bmatrix} \dot{x}_p \\ x_p \\ \dot{y}_p \\ y_p \end{bmatrix} \tag{C.1}$$

This means that $\dot{\mathbf{z}}$ is given by Eq. C.2.

$$\dot{\mathbf{z}} = \begin{bmatrix} \frac{18}{\hat{R}^2 \mathrm{Re}_f} \frac{\mathrm{Re}_p C_D}{24} \left[\left(1 + \frac{1}{\pi} \frac{x_p}{x_p^2 + y_p^2} \right) - \dot{x}_p \right] - \frac{3}{\pi} \left[\frac{x_p^2 - y_p^2 + \frac{x_p}{\pi}}{(x_p^2 + y_p^2)^2} \right] \\ \dot{x}_p \\ \frac{18}{\hat{R}^2 \mathrm{Re}_f} \frac{\mathrm{Re}_p C_D}{24} \left[\left(\frac{1}{\pi} \frac{y_p}{x_p^2 + y_p^2} \right) - \dot{y}_p \right] - \frac{3}{\pi} \left[\frac{y_p \left(2x_p + \frac{1}{\pi} \right)}{(x_p^2 + y_p^2)^2} \right] \\ \dot{y}_p \end{bmatrix} \tag{C.2}$$

Now it can be seen that the following holds: $\dot{\mathbf{z}} = f(\mathbf{z})$. So, the first derivative of a vector $\mathbf{z}$ is a function of that same vector, leading to an, in general, non-linear system of first-order ODE's.

D Equivalent Stokes number

The equivalent Stokes number can be found by considering the equation of motion (Eq. 2.7) in the Stokesian regime in one dimension, and in a quiescent flow (not necessary but used so that the velocity is the relative velocity). This leads to Eq. D.1.

$$\frac{1}{2}\frac{4}{3}\pi R^3 \rho_f \frac{dv_p}{dt} = 6\pi\mu_f R v_p \tag{D.1}$$

Rewriting Eq. D.1 leads to Eq. D.2.

$$\frac{dv_p}{dt} = \frac{18\mu_f}{2\rho_f R^2} v_p \tag{D.2}$$

Neglecting the time dependency of the nucleus radius leads to a solution given in Eq. D.3.

$$v_p = A e^{\frac{18\mu_f}{2\rho_f R_0^2} t} \tag{D.3}$$

Where A is an undefined constant. The relaxation time, t_0, can be recognized in Eq. D.3 as $t_0 = \frac{2\rho_f R_0^2}{18\mu_f}$. This relaxation time is the characteristic time of a nucleus to adapt to the flow. The characteristic time of the flow is given as $\frac{h}{U_0}$. If the time scale of the flow is significantly larger than the time scale of the nucleus, the nucleus follows the flow. The initial equivalent Stokes number can be found in Eq. D.4.

$$\mathrm{Stk}_{eq0} = \frac{2R_0^2 U_0}{18\nu_f h} = \frac{\hat{R}_0^2 \mathrm{Re}_f}{18} \tag{D.4}$$

Example

A classic condition on the Stokes number is that the Stokes number should be smaller than 0.1. With $U_0 = 15.24\, ms^{-1}$ and $h = 15.24\, mm$ leading to $\mathrm{Re}_f = 7.14 \cdot 10^5$ gives that the limiting initial dimensionless nucleus radius is $\hat{R}_0 < 0.002$. The limiting initial dimensionfull nucleus radius is $R_0 < 30\, \mu m$.

E Deriving normal distance from streamline

Starting from the equation of motion given in Eq. E.1 using Stokes flow Eq. E.2 is found.

$$\underbrace{\frac{1}{2}\frac{4}{3}\pi R^3\rho_f\frac{d\mathbf{w}_p}{dt}}_{\text{Added mass force}} = \underbrace{\frac{1}{2}\rho_f(\mathbf{w}-\mathbf{w}_p)|\mathbf{w}-\mathbf{w}_p|C_D\pi R^2}_{\text{Drag force}} - \underbrace{\frac{3}{2}\frac{4}{3}\pi R^3\nabla p}_{\text{Pressure force}} \tag{E.1}$$

$$\frac{1}{2}\frac{4}{3}\pi R^3\rho_f\frac{d\mathbf{w}_p}{dt} = \frac{1}{2}\rho_f\nu_f(\mathbf{w}-\mathbf{w}_p)\pi R - \frac{3}{2}\frac{4}{3}\pi R^3\nabla p \tag{E.2}$$

To determine the normal distance from a streamline to a trajectory requires the local normal velocity. The local normal velocity of the flow with respect to the initial streamline is (close to) zero and remains (close to) zero. Therefore, the acceleration in the normal direction should also be (close to) zero. This gives Eq. E.3.

$$0 = -\frac{1}{2}\rho_f\nu_f(U_{n,p})\pi R - \frac{3}{2}\frac{4}{3}\pi R^3\frac{\partial p}{\partial n} \tag{E.3}$$

Where $U_{n,p}$ is the normal velocity of the nucleus. Rewriting gives Eq. E.4.

$$U_{n,p} = \alpha\frac{2}{9}\frac{R^2}{\mu_f}\frac{\partial p}{\partial n} \quad \text{With} \quad \alpha = -\frac{3}{2} \tag{E.4}$$

The normal distance from the streamline can now be found by integrating the normal velocity in time, see Eq. E.5.

$$\epsilon = \int_A^B \alpha\frac{2}{9}\frac{R^2}{\mu_f}\frac{\partial p}{\partial n}dt \tag{E.5}$$

Where A is a point in time well before the largest pressure gradients in the normal direction and B well after that point. Non-dimensionalizing Eq. E.5 leads to Eq. E.6.

$$\epsilon = \frac{2\alpha}{9}\frac{R^2U_0}{\nu_f}\int_a^b \frac{1}{\rho_f U_0^2}\frac{\partial p}{\partial\frac{n}{r_h}}\frac{U_0}{|q|}d\left(\frac{s}{r_h}\right) \tag{E.6}$$

In Eq. E.6 the integral is now along the trajectory with coordinate s by $t = \frac{s}{|q|}$. q is the flow velocity along s. The integral is dimensionless with boundaries a and b which now represents the location along the streamline well before and after the largest pressure gradients. r_h represents the initial condition, $y_{p,0}$. Already, it can be seen that ϵ is proportional to R^2 and U_0. In [4] the same result is found apart from the factor α. For this Appendix, the proportionality was important, that is found in accordance with [4]. The factor $\alpha = -\frac{3}{2}$ is negative, this could simply be neglected since ϵ is a normal distance which depends on the choice of the normal direction. The factor $\frac{3}{2}$ is implemented for accelerating flow fields. Assuming Stokes flow it can be argued if the nucleus is actually in an accelerating flow field.

Finally, Eq. E.7 can be found by non-dimensionalizing Eq. E.6 further and collapsing the integral to the initial condition depended term $\sum(r/r_h)$.

$$\frac{\epsilon}{r_h} = \frac{2\alpha \mathrm{Re}_f \hat{R}^2}{18\frac{r_h}{h}} \sum(r/r_h) \quad \rightarrow \quad \frac{\epsilon}{r_h} = \frac{2\alpha \mathrm{Stk}_{eq}}{\frac{r_h}{h}} \sum(r/r_h) \tag{E.7}$$

In Eq. E.7, the proportionally of the distance from the streamline to the equivalent Stokes number can be seen.

F Derivation of bubble dynamics equations

F.1 Derivation of the Rayleigh-Plesset equation

In this derivation [8] has been used to provide the directions.
The Rayleigh-Plesset equation can be derived from the Navier-Stokes equations (Eq. F.1) together with the mass conservation equation (Eq. F.2).

$$\rho_f \left(\frac{\partial \mathbf{w}}{\partial t} + \mathbf{w} \cdot \nabla \mathbf{w} \right) = -\nabla p + \mu_f \nabla^2 \mathbf{w} + \zeta_f \nabla \nabla \cdot \mathbf{w} \tag{F.1}$$

$$\frac{\partial \rho_f}{\partial t} + \nabla \cdot \left(\rho_f \mathbf{w} \right) = 0 \tag{F.2}$$

ζ_f is the bulk viscosity of the fluid. This viscosity comes into play when the fluid is being contracted or expanded.
It is assumed that the fluid is isothermal, and for that reason the energy equation is not used.

Using the identity $\mathbf{w}\nabla\mathbf{w} = \frac{1}{2}\nabla\mathbf{w^2}$ and writing the velocity via the potential, $\mathbf{w} = \nabla\phi$, gives Eqs. F.3-F.4.

$$\rho_f \left(\frac{\partial \nabla \phi}{\partial t} + \frac{1}{2} \nabla (\nabla \phi \nabla \phi) \right) = -\nabla p + \mu_f \nabla^2 \nabla \phi + \zeta_f \nabla \nabla \cdot \nabla \phi \tag{F.3}$$

$$\frac{\partial \rho_f}{\partial t} + \nabla \cdot \left(\rho_f \nabla \phi \right) = 0 \tag{F.4}$$

Assuming a spherical gas nucleus all the time will mean that the velocity field near the nuclues will be fully spherical (if the nucleus is followed along its track). This means that the local streamlines will never interfere and therefore the viscosity does not play a role, this leads to Eq. F.5.

$$\rho_f \left(\frac{\partial \nabla \phi}{\partial t} + \frac{1}{2} \nabla (\nabla \phi \nabla \phi) \right) = -\nabla p \tag{F.5}$$

Since the spatial differential operator just as the temporal operator is a linear operator, the order of operations may be switched. This leads to Eq. F.6.

$$\rho_f \nabla \left(\frac{\partial \phi}{\partial t} + \frac{1}{2} \nabla \phi \cdot \nabla \phi \right) = -\nabla p \tag{F.6}$$

Eq. F.6 as a weak formulation one finds Eq. F.7.

$$\rho_f \left(\frac{\partial \phi}{\partial t} + \frac{1}{2} \left(\nabla \phi \right)^2 \right) = -p \tag{F.7}$$

If the assumption of only radial velocity components is re-used finally one finds Eq. F.8.

$$\rho_f \left(\frac{\partial \phi}{\partial t} + \frac{1}{2} \left(\frac{\partial \phi}{\partial r} \right)^2 \right) = -p \tag{F.8}$$

For the mass conservation equation (Eq. F.4) more or less the same steps can be taken leading to Eq. F.9.

$$\frac{\partial \rho_f}{\partial t} + \nabla \rho_f \cdot \nabla \phi + \rho_f \nabla^2 \phi = 0 \tag{F.9}$$

If again the sphericity of the nucleus is used one finds Eq. F.10.

$$\frac{\partial \rho_f}{\partial t} + \frac{\partial \rho_f}{\partial r} \frac{\partial \phi}{\partial r} + \rho_f \nabla^2 \phi = 0 \tag{F.10}$$

The objective now is to find one equation for the potential, ϕ, this can be accomplished by taking the temporal derivative of the pressure. First it should be noted that the $dp = \frac{dp}{d\rho_f} d\rho_f = c^2 d\rho_f$. Using both Eqs F.8-F.10 Eq. F.11 can be found.

$$\begin{aligned} -\frac{\partial p}{\partial t} &= -c^2 \frac{\partial \rho_f}{\partial t} = c^2 \left[\frac{\partial \rho_f}{\partial r} \frac{\partial \phi}{\partial r} + \rho_f \nabla^2 \phi \right] \quad \text{and:} \\ -\frac{\partial p}{\partial t} &= \frac{\partial}{\partial t} \left(\rho_f \left[\frac{\partial \phi}{\partial t} + \frac{1}{2} \left(\frac{\partial \phi}{\partial r} \right)^2 \right] \right) \end{aligned} \tag{F.11}$$

Clearly, both terms of Eq. F.11 can be equated. Equating both parts, using the product rule of differentiation and rearranging gives Eq. F.12.

$$\nabla^2 \phi = \frac{1}{c^2 \rho_f} \frac{\partial \rho_f}{\partial t} \left[\frac{\partial \phi}{\partial t} + \frac{1}{2} \left(\frac{\partial \phi}{\partial r} \right)^2 \right] + \frac{1}{c^2} \left[\frac{\partial^2 \phi}{\partial t^2} + \frac{1}{2} \frac{\partial \left(\frac{\partial \phi}{\partial r} \right)^2}{\partial t} \right] - \frac{1}{\rho_f} \frac{\partial \phi}{\partial r} \frac{\partial \rho_f}{\partial r} \tag{F.12}$$

If $dH = \frac{dp}{\rho_f}$, $\frac{\partial \rho_f}{\partial t} = \frac{\rho_f}{c^2} \frac{\partial H}{\partial t}$, $\frac{\partial}{\partial t} = \frac{1}{u} \frac{\partial}{\partial r}$, $\frac{\partial r}{\partial t} = u = \frac{\partial \phi}{\partial r}$ and lastly $\frac{1}{2} \frac{\partial y^2}{\partial x} = \frac{\partial \frac{1}{2} y^2}{\partial y} \frac{\partial y}{\partial x} = y \frac{\partial y}{\partial x}$ are used one finds Eq. F.13.

$$\nabla^2 \phi = \frac{1}{u c^4} \frac{\partial H}{\partial r} \left[\frac{\partial \phi}{\partial t} + \frac{1}{2} \left(\frac{\partial \phi}{\partial r} \right)^2 \right] + \frac{1}{c^2} \left[\frac{\partial^2 \phi}{\partial t^2} + u \frac{\partial u}{\partial t} \right] - \frac{u}{c^2} \frac{\partial H}{\partial r} \tag{F.13}$$

Now reuse the momentum equation, to find Eq. F.14.

$$\nabla^2 \phi = -\frac{1}{u c^4} \frac{\partial H}{\partial r} \frac{p}{\rho_f} + \frac{1}{c^2} \left[\frac{\partial^2 \phi}{\partial t^2} + u \frac{\partial u}{\partial t} \right] - \frac{u}{c^2} \frac{\partial H}{\partial r} \tag{F.14}$$

Rearranging gives Eq. F.15.

$$\nabla^2 \phi = \frac{u}{c^2} \left(\frac{\partial u}{\partial t} - \frac{\partial H}{\partial r} \left[1 + \frac{p}{\rho_f c^2 u^2} \right] \right) + \frac{1}{c^2} \frac{\partial^2 \phi}{\partial t^2} \tag{F.15}$$

Knowing that the pressure is of the same order as the density times the free stream velocity squared. Assuming that the free stream velocity is much smaller than the speed of sound, yields the term in between square brackets to be reduced to 1, this finally gives Eq. F.16.

$$\nabla^2\phi = \frac{u}{c^2}\left(\frac{\partial u}{\partial t} - \frac{\partial H}{\partial r}\right) + \frac{1}{c^2}\frac{\partial^2\phi}{\partial t^2} \tag{F.16}$$

Eq. F.16 needs to be solved as a function off the wall velocity of the nucleus ($\frac{dR}{dt}$). From Eq. F.16 it can be seen that with a velocity field with significant lower velocities the first term cancels ($\frac{u}{c^2} \approx 0$). The linear term involving $\frac{\partial^2\phi}{\partial t^2}$ can be neglected near the nucleus, under the assumption that $c^2 \gg \frac{\partial^2\phi}{\partial t^2}$. This leads to the conclusion that near the nucleus the Laplace equation holds for the potential ($\nabla^2\phi$=0). At the nucleus wall the radial velocity is known, namely the velocity of the nucleus wall itself. This leads to a solution shown in Eq. F.17.

$$\phi = -\frac{\dot{R}R^2}{r} + A(t) \tag{F.17}$$

Where $\dot{R} = \frac{dR}{dt}$ and $A(t)$ is a free constant possibly depending on time. The constant $A(t)$ will represent the sound field initiated by the nuclei growth and collapse. Since the nucleus is much smaller than the sound wave length (note that this is a crucial assumption, but realistic since the wavelenght of sound of $1\,kHz$ in water is about $1.5\,m$), the sound field will be independent of r at large distances from the nucleus. This means that the first term will be omitted far from the nucleus so that Eq. F.18 remains.

$$\phi = A(t) \tag{F.18}$$

It is also known that far away from the nucleus the potential is equal to the potential at infinity giving $A(t) = \phi_\infty(t)$. So the full potential is given by Eq. F.19.

$$\phi = -\frac{\dot{R}R^2}{r} + \phi_\infty(t) \tag{F.19}$$

It can be seen that the velocity $u = \frac{\partial\phi}{\partial r} = \frac{\dot{R}R^2}{r^2}$, and that at $r = R$ the boundary condition indeed holds. Having the velocity, the force balance on the surface of the nucleus can be made. This is done in terms of the pressure, see Eq. F.20. The shear viscosity has however now been included via the shear term $\frac{\partial u}{\partial r}(r = R)$.

$$p_g(t) + p_v - p[R(t)] + 2\mu_f\frac{\partial u}{\partial r}(r = R) = 2\frac{\gamma}{R} \tag{F.20}$$

Differentiating the velocity field to r leads to Eq. F.21.

$$p_g(t) + p_v - p[R(t)] - 4\mu_f\frac{\dot{R}}{R} = 2\frac{\gamma}{R} \tag{F.21}$$

The pressure in the nucleus of the gas, p_g, is assumed to be spatially uniform, meaning that body forces are not allowed. If Eq. F.8 is used again, and the pressure term of Eq. F.21 is used one finds Eq. F.22.

$$\rho_f \left(\frac{\partial \phi}{\partial t} + \frac{1}{2} \left(\frac{\partial \phi}{\partial r} \right)^2 \right) = -p_g(t) - p_v + 4\mu_f \frac{\dot{R}}{R} + 2\frac{\gamma}{R} \tag{F.22}$$

Knowing that $\frac{\partial \phi}{\partial r} = u$ and filling it in at $r = R$ gives $\frac{\partial \phi}{\partial r} = \dot{R}$. $\frac{\partial \phi}{\partial t}$ is derived in Eq. F.23.

$$\frac{\partial \phi}{\partial t} = \frac{\partial}{\partial t} \left(-\frac{\dot{R} R^2}{r} \right) + \frac{\partial}{\partial t} \left(\phi_\infty(t) \right) = -\ddot{R} R - 2\dot{R}^2 + \frac{\partial}{\partial t} \left(\phi_\infty(t) \right) \tag{F.23}$$

Using Eq. F.23 in Eq. F.22 gives Eq. F.24.

$$\rho_f \left[R \frac{d^2 R}{dt^2} + \frac{3}{2} \left(\frac{dR}{dt} \right)^2 \right] = p_g(t) + p_v - 4\mu_f \frac{\dot{R}}{R} - 2\frac{\gamma}{R} + \rho_f \frac{\partial \phi_\infty}{\partial t} \tag{F.24}$$

The term $\rho_f \frac{\partial \phi_\infty}{\partial t}$ is the source term in the equation. This can be included in the following way: $\rho_f \frac{\partial \phi_\infty}{\partial t} = -P_0 - P(t)$.

$$\rho_f \left[R \frac{d^2 R}{dt^2} + \frac{3}{2} \left(\frac{dR}{dt} \right)^2 \right] = p_g(t) + p_v - P_0 - P(t) - 4\mu_f \frac{\dot{R}}{R} - 2\frac{\gamma}{R} \tag{F.25}$$

The source term depends in this case on the nucleus path, therefore the pressure which the nucleus feels, taken as p can be taken as this source. Including this term gives Eq. F.26 is found.

$$\rho_f \left[R \frac{d^2 R}{dt^2} + \frac{3}{2} \left(\frac{dR}{dt} \right)^2 \right] = p_v - p + p_g(t) - 2\frac{\gamma}{R} - \frac{4\mu_f}{R} \frac{dR}{dt} \tag{F.26}$$

To improve the found equation the gas pressure derivative can be included. Furthermore the influence of the radiated sound wave can be included to implement the effect of damping. Lastly it is important to have a realistic equation of state. This will all be examined later.

F.2 Derivation of the general Keller-Herring equation

In this derivation both [9] and [8] have been used extensively.
The derivation of this equation is comparable to the derivation of the Rayleigh-Plesset equation, with the only difference being that the radiated sound wave is taken in consideration. Waves in general can be solved by a function which is constant in time when the observer of the solution is moving with the wave speed. This holds in both directions, and therefore a general wave solution can be seen in Eq. F.27.

$$Q_{\text{Wave}} = F(t - \frac{r}{c}) + G(t + \frac{r}{c}) \tag{F.27}$$

Since the wave is created by a changing volume in time the units of the solution are $[m^3 s^{-1}]$. It is obvious that if one travels at the speed of sound, c, the argument of the function F is

constant, and therefore the value of F. Since the wave is defined in polar coordinates, the opposing wave the is undefined, so $G = 0$. This leads to $Q_{\text{Wave}} = F(t - \frac{r}{c})$. If the wave is implemented in the potential of Eq. F.17 one finds Eq. F.28.

$$\phi = -\frac{\dot{R}R^2}{r} + A(t) = \phi_\infty(t) - \frac{1}{r}F(t - \frac{r}{c}) \tag{F.28}$$

So it can be seen that the potential far away from the nuclues is still $\phi_\infty(t)$, but now with the wave potential of the wave added.
The wave function $F(t - \frac{r}{c})$ can be approximated as $F(t - \frac{r}{c}) = F(t) - \frac{r}{c}\frac{dF(t)}{dt}$ via a first-order Taylor expansion around the point t. Using this relation one finds Eq. F.29.

$$\phi = \phi_\infty(t) - \frac{1}{r}F(t - \frac{r}{c}) \approx \phi_\infty(t) - \frac{1}{r}F(t) + \frac{1}{c}\frac{dF(t)}{dt} \tag{F.29}$$

By comparing Eq. F.28 and Eq. F.29 one finds that $F(t) = \dot{R}R^2$ and $A(t) = \phi_\infty(t) + \frac{1}{c}\frac{dF(t)}{dt}$.
Following the derivation of the Rayleigh-Plesset equation, the found potential should now be included in the reduced momentum equation (Eq. F.8). This involves calculating $\frac{\partial\phi}{\partial t}$ and $\frac{\partial\phi}{\partial r}$ at $r = R$. These calculations will be done term wise starting with $\frac{\partial\phi}{\partial r}$, see Eq. F.30.

$$\frac{\partial\phi}{\partial r}(r = R) = \frac{\dot{R}R^2}{r^2}|_{r=R} = \dot{R} \tag{F.30}$$

Calculating $\frac{\partial\phi}{\partial t}$ will be more involved, but will be started in Eq. F.31.

$$\begin{aligned}\frac{\partial\phi}{\partial t}|_{r=R} &= \frac{d\phi_\infty(t)}{dt} - \frac{1}{r}\frac{d(\dot{R}R^2)}{dt} + \frac{1}{c}\frac{d^2(\dot{R}R^2)}{dt^2} \\ &= \frac{d\phi_\infty(t)}{dt} - \frac{1}{R}\left(\ddot{R}R^2 + 2R\dot{R}^2\right) + \frac{1}{c}\frac{d^2(\dot{R}R^2)}{dt^2} \\ &= \frac{d\phi_\infty(t)}{dt} - \left(\ddot{R}R^2 + 2\dot{R}^2\right) + \frac{1}{c}\frac{d^2(\dot{R}R^2)}{dt^2}\end{aligned} \tag{F.31}$$

The latter part of Eq. F.31 ($\frac{d^2(\dot{R}R^2)}{dt^2}$) will be treated separately, which can be seen in Eq. F.32.

$$\frac{d^2(\dot{R}R^2)}{dt^2} = \frac{d}{dt}\left(\ddot{R}R^2 + 2\dot{R}^2R\right) \tag{F.32}$$

The first part ($\frac{d}{dt}\left(\ddot{R}R^2\right)$) of Eq. F.32 will lead to a third derivative of the radius of the nucleus with respect to time. This is an unwanted derivative, since it requires an extra initial condition on the acceleration of the boundary of the nucleus. By that it turns out that this will not work numerically according to [9]. To prevent this problem the third derivative can be expressed in terms of the normal Rayleigh-Plesset equation (Eq. F.26). It can be seen that the term $\ddot{R}R$ can be extracted from the Rayleigh-Plesset equation. This is a simplification of course, since the objective is to look for a more advanced equation for the gas nucleus

dynamics, but it is the best option available. So after some tedious derivation Eq. F.33 is found.

$$\begin{aligned}\frac{d}{dt}\left(\ddot{R}R^2\right) &= \frac{d}{dt}\left\{R\left[\frac{1}{\rho_f}\left(p_v - p + p_g(t) - 2\frac{\gamma}{R} - \frac{4\mu_f}{R}\dot{R}\right) - \frac{3}{2}\dot{R}^2\right]\right\} \\ &= -\frac{3}{2}\dot{R}^3 - 3R\dot{R}\ddot{R} + \frac{\dot{R}}{\rho_f}\left(p_v - p + p_g(t)\right) + \frac{1}{\rho_f}\dot{p_g}R\end{aligned} \tag{F.33}$$

Adding the result of Eq. F.33 with $\frac{d}{dt}\left(2\dot{R}^2R\right) = 2\dot{R}^3 + 4R\dot{R}\ddot{R}$ gives Eq. F.34.

$$\frac{d^2(\dot{R}R^2)}{dt^2} = \frac{1}{2}\dot{R}^3 + R\dot{R}\ddot{R} + \frac{\dot{R}}{\rho_f}\left(p_v - p + p_g(t)\right) + \frac{1}{\rho_f}\dot{p_g}R \tag{F.34}$$

Filling in Eq. F.34 into Eq. F.31 and knowing that the source term is the negative pressure of the flow over the density of the liquid so, $\frac{\partial\phi_\infty}{\partial t} = -\frac{p}{\rho_f}$ gives Eq. F.35.

$$\begin{aligned}&\frac{\partial\phi}{\partial t}|_{r=R} = \\ &-\frac{p}{\rho_f} - \left(\ddot{R}R + 2\dot{R}^2\right) + \frac{\dot{R}}{c}\left[\frac{1}{2}\dot{R}^2 + \ddot{R}R + \frac{1}{\rho_f}\left(p_v - p + p_g(t)\right) + \frac{1}{\rho_f}\dot{p_g}R\right]\end{aligned} \tag{F.35}$$

Using Eq. F.22 and Eq. F.30 and Eq. F.35 one finds Eq. F.36.

$$\begin{aligned}&-p - \rho_f\left(\ddot{R}R + \frac{3}{2}\dot{R}^2\right) + \rho_f\frac{\dot{R}}{c}\left[\frac{1}{2}\dot{R}^2 + \ddot{R}R + \frac{1}{\rho_f}\left(p_v - p + p_g(t)\right) + \frac{1}{\rho_f}\dot{p_g}R\right] = \\ &-p_g(t) - p_v + 4\mu_f\frac{\dot{R}'}{R} + 2\frac{\gamma}{R}\end{aligned} \tag{F.36}$$

Rewriting Eq. F.36 gives Eq. F.37.

$$\begin{aligned}&\left(1 - \frac{\dot{R}}{c}\right)\rho_f R\ddot{R} + \frac{3}{2}\dot{R}^2\rho_f\left(1 - \frac{\dot{R}}{3c}\right) = \\ &\left(1 + \frac{\dot{R}}{c}\right)\left[p_v - p + p_g(t)\right] + \frac{R}{c}\dot{p_g}(t) - 4\mu_f\frac{\dot{R}}{R} - 2\frac{\gamma}{R}\end{aligned} \tag{F.37}$$

As can be seen in Eq. F.37 the found equation will reduce to the Rayliegh-Plesset equation if $c \gg \dot{R}$ plus an extra term with the temporal derivative of the gas pressure. Eq. F.37 is called the Keller equation in [9] and [8].
Eq. F.37 can be derived in a more general way, namely by adding the Rayleigh-Plesset equation the equation resulting in a third order temporal derivative. This leads to the general Keller-Herring equation, which is given in Eq. F.38.

$$\begin{aligned}&\left(1 - (\lambda+1)\frac{\frac{dR}{dt}}{c}\right)\rho_f R\frac{d^2R}{dt^2} + \frac{3}{2}\frac{dR}{dt}^2\rho_f\left(1 - (\lambda + \frac{1}{3})\frac{\frac{dR}{dt}}{c}\right) = \\ &\left(1 + (1-\lambda)\frac{\frac{dR}{dt}}{c}\right)\left[p_v - p + p_g(t)\right] + \frac{R}{c}\frac{dp_g(t)}{dt} - 4\mu\frac{\frac{dR}{dt}}{R} - \frac{2\gamma}{R}\end{aligned} \tag{F.38}$$

If the factor λ in Eq. F.38 is set to 0 the Keller Miksis equation is found, and if λ is set to 1 the equation used by Herring and Trilling is found.

G Total set of equations

System of equations to be solved when the nucleus does not hit the body:

$$\frac{d}{dt}\begin{bmatrix} x_p \\ u_p \\ y_p \\ v_p \\ R \\ \frac{dR}{dt} \end{bmatrix} = \begin{bmatrix} u_p \\ \frac{1}{\rho_p \frac{4}{3}\pi R_0^3 + C_{am}\rho_f \frac{4}{3}\pi R^3}\left\{ C_{am}\rho_f 4\pi R^2 \frac{dR}{dt}(u-u_p) + \frac{1}{2}\rho_f C_D \pi R^2 (u-u_p)|\mathbf{w}-\mathbf{w_p}| - (1+C_{am})\,\frac{4}{3}\pi R^3 \frac{\partial p}{\partial x} - 6\pi R\mu_f \left(\int_{t_0}^{t-\Delta t_n} K(t,\tau)\frac{d\hat{u}}{d\tau}d\tau + \frac{d\hat{u}}{d\tau}|_{t-\Delta t_n}\sqrt{\frac{\tau_d \Delta t_n}{\pi}} \right) \right\} \\ v_p \\ \frac{1}{\rho_p \frac{4}{3}\pi R_0^3 + C_{am}\rho_f \frac{4}{3}\pi R^3}\left\{ C_{am}\rho_f 4\pi R^2 \frac{dR}{dt}(v-v_p) + \frac{1}{2}\rho_f C_D \pi R^2 (v-v_p)|\mathbf{w}-\mathbf{w_p}| - (1+C_{am})\,\frac{4}{3}\pi R^3 \frac{\partial p}{\partial y} + \frac{4}{3}\pi R_0^3 g(\rho_p - \rho_f) - 6\pi R\mu_f \left(\int_{t_0}^{t-\Delta t_n} K(t,\tau)\frac{d\hat{v}}{d\tau}d\tau + \frac{d\hat{v}}{d\tau}|_{t-\Delta t_n}\sqrt{\frac{\tau_d \Delta t_n}{\pi}} \right) \right\} \\ \frac{dR}{dt} \\ \frac{1}{\left(1-(\lambda+1)\frac{\frac{dR}{dt}}{c}\right)\rho_f R}\left\{ -\frac{3}{2}\frac{dR}{dt}^2 \rho_f \left(1-(\lambda+\frac{1}{3})\frac{\frac{dR}{dt}}{c}\right) + \left(1+(1-\lambda)\frac{\frac{dR}{dt}}{c}\right)\left[p_v - p + p_g(t)\right] + \frac{R}{c}\frac{dp_g(t)}{dt} - 4\mu_f \frac{\frac{dR}{dt}}{R} - \frac{2\gamma}{R} \right\} \end{bmatrix} \tag{G.1}$$

System of equations to be solved when the nucleus hits the body:

$$\frac{d}{dt}\begin{bmatrix} x_p \\ u_p \\ y_p \\ v_p \\ R \\ \\ \frac{dR}{dt} \end{bmatrix} = \begin{bmatrix} u + \hat{n}_x \frac{dR}{dt} \\ \frac{\partial u}{\partial x}u_p + \frac{\partial u}{\partial y}v_p + \hat{n}_x \frac{d^2R}{dt^2} \\ v + \hat{n}_y \frac{dR}{dt} \\ \frac{\partial v}{\partial x}u_p + \frac{\partial v}{\partial y}v_p + \hat{n}_y \frac{d^2R}{dt^2} \\ \frac{dR}{dt} \\ \frac{1}{\left(1-(\lambda+1)\frac{\frac{dR}{dt}}{c}\right)\rho_f R}\left\{ -\frac{3}{2}\frac{dR}{dt}^2 \rho_f \left(1-(\lambda+\frac{1}{3})\frac{\frac{dR}{dt}}{c}\right) + \left(1+(1-\lambda)\frac{\frac{dR}{dt}}{c}\right)\left[p_v - p + p_g(t)\right] + \frac{R}{c}\frac{dp_g(t)}{dt} - 4\mu_f \frac{\frac{dR}{dt}}{R} - \frac{2\gamma}{R} \right\} \end{bmatrix} \tag{G.2}$$